TUDelft

Delft University of Technology

An integrated aero-structural model for ram-air kite simulations with application to airborne wind energy

Thedens, P.

DOI

Publication date
2022

Document Version
Final published version

Citation (APA)

Important note
To cite this publication, please use the final published version (if applicable).
Please check the document version above.

An Integrated Aero-Structural Model for Ram-Air Kite Simulations

with Application to Airborne Wind Energy

AN INTEGRATED AERO-STRUCTURAL MODEL FOR RAM-AIR KITE SIMULATIONS

WITH APPLICATION TO AIRBORNE WIND ENERGY

Proefschrift

ter verkrijging van de graad van doctor
aan de Technische Universiteit Delft,
op gezag van de Rector Magnificus prof. dr.ir. T.H.J.J. van der Hagen,
voorzitter van het College voor Promoties,
in het openbaar te verdedigen op maandag 25 april 2022 om 10:00 uur

door

Paul THEDENS

Master of Science in Aerospace Engineering,
Delft University of Technology, Delft, The Netherlands,
Technical University of Denmark, Lyngby, Denmark,
geboren te Henstedt-Ulzburg, Duitsland.

Dit proefschrift is goedgekeurd door de

Promotor: Prof. dr. G.J.W. van Bussel
Copromotor: Dr.-Ing. R. Schmehl

Samenstelling promotiecommissie:

Rector Magnificus,	voorzitter
Prof. dr. G.J.W. van Bussel,	Technische Universiteit Delft
Dr.-Ing. R. Schmehl,	Technische Universiteit Delft

Onafhankelijke leden:

Prof. dr. D.A. von Terzi	Technische Universiteit Delft
Prof. dr. G. Sanchez-Arriaga	Universidad Carlos III de Madrid
Prof. dr. C. Kassapoglou,	Technische Universiteit Delft
Dr. P. Tiso,	ETH Zurich
Dr. M. Gaunaa,	DTU Technical University of Denmark

CONTENTS

SUMMARY

The airborne wind energy (AWE) technology aims to utilise tethered wings to harvest wind energy at altitudes conventional wind turbines cannot reach. There are two distinct methods to harvest airborne wind energy: onboard and ground-based generation. The onboard generation is achieved through flying fast manoeuvres driving propellers attached to the tethered wing, while the generated electricity is conducted through the tether. On the other hand, the ground-based generation utilises the tether tension of the kite to unwind it from a drum, driving a generator. When the tether is fully extended, it is reeled in by the generator, which consumes energy. Since the traction phase is a lot longer and produces a lot more electricity than electricity needed in the reel-in phase the net energy of such a cycle is positive. SkySails Power is one of the leading companies developing a ground-based AWE generator driven by a large ram-air kite. This thesis describes the development of a methodology for simulating their wing.

A ram-air wing is made of a thin fabric, and it obtains its three-dimensional shape from the internal pressure fed by intakes located in the frontal section of the wing. Simulating such a wing is challenging because it is nonrigid and experiences large deformations during the flight that changes its aerodynamic properties. Therefore, a coupled simulation strategy is developed based on the fluid-structure interaction method, where the parafoil's shape and aerodynamic performance are found iteratively. The parafoil's shape is determined with a finite element solver using dynamic relaxation; a computational method specifically developed for form-finding of membrane structures. A panel method is used to find the aerodynamic pressure field acting on the wing. Both solvers are coupled with *preCICE* which is an open-source tool developed explicitly to couple solvers to model physical processes such as fluid-structure interaction. A variety of coupling algorithms are tested to obtain fast convergence. The toolchain is tested on two parafoil designs: a $160m^2$ wing studied by fellow researchers and used for verification purposes and a 120m^2 wing flown by SkySails Power. The numerical model is validated with sensor data obtained during several flight hours. The simulation shows a good agreement with the force measurements and can predict critical parameters of the parafoil with satisfying accuracy. The toolchain has proven to be sufficiently numerically stable and can be used in the initial design phase for parafoils and reinforcement layout. Finally, a multi-disciplinary design optimisation on a 2D nonrigid wing profile with local reinforcements is developed. The optimiser found a variety of profile shapes and reinforcement designs, which minimises the strain energy of the rib structure and maximises the power harvesting factor. The method presented in the thesis exhibits possible design choices that compromise the maximum performance and the least deformed rib.

SAMENVATTING

Met Airborne Wind Energy (AWE) technologie wordt geprobeerd om, door middel van een vliegende vleugel die vastzit aan een kabel, windenergie te oogsten op grotere hoogten dan die met conventionele windturbines te bereiken zijn. Er zijn twee verschillende methodes om deze windenergie van grote hoogtes te produceren: aan boord van de vleugel of via de kabel op de grond. Het opwekken van windenergie aan boord gebeurt door propellers die bevestigd zijn aan de vleugel en die worden aangedreven door het snel vliegen van manoeuvres. Vervolgens wordt de geproduceerde elektriciteit via een kabel naar de grond gebracht. De tweede methode gebruikt de trekkracht in de kabel voor het opwekken van windstroom door de kabel van een trommel, die op de grond staat, af te wikkelen en daarmee een generator aan te drijven. Wanneer de kabel volledig is afgerold, wordt deze weer opgerold met energie die door de generator wordt geleverd. Omdat de hoeveelheid elektriciteit die geproduceerd wordt tijdens de lange uitrol-fase veel groter is dan de elektriciteit die nodig om de kabel in korte tijd weer op te rollen, is het netto resultaat positief. SkySails Power is één van de toonaangevende AWE bedrijven dat een systeem ontwikkelt met een grote ram-air vleugel die via een kabel de generator in het grondstation aandrijft. Dit proefschrift beschrijft de ontwikkeling van een methodologie voor het simuleren van een dergelijke vlieger.

Een ram-air-vleugel is gemaakt van dunne stof en krijgt zijn driedimensionale vorm door de interne druk die ontstaat door de luchttoevoer via gaten in het voorste gedeelte van de vleugel. Het simuleren van zo'n vleugel is een uitdaging omdat die niet stijf is en tijdens de vlucht grote vervormingen ondergaat die de aerodynamische eigenschappen veranderen. Daarom is een gekoppelde simulatie-strategie ontwikkeld op basis van de stroming-structuur interactie, waarbij de vorm van de vleugel en de aerodynamische prestaties iteratief worden gevonden. De vorm van de flexibele vleugel (de parafoil) wordt berekend met de eindige-elementenmethode met behulp van een dynamische relaxatie. Dit is een rekenmethode speciaal ontwikkeld voor het vinden van de vorm van flexibele membraanstructuren. Een panelenmethode wordt gebruikt om het aerodynamische drukveld te bepalen dat op de vleugel werkt. Beide berekeningsmethoden zijn gekoppeld aan *preCICE*, een open-sourcetool die specifiek ontwikkeld is voor het modelleren van fysieke processen zoals stroming-structuur interactie. Een verscheidenheid aan koppelingsalgoritmen is geïmplementeerd om te onderzoeken hoe een snelle convergentie te verkrijgen. De "toolchain" van methoden is getest op twee parafoil-ontwerpen: een vleugel van 160m^2 bestudeerd door collega-onderzoekers en gebruikt voor verificatiedoeleinden en een vleugel van 120m^2 van SkySails Power. Het numerieke model wordt gevalideerd aan de hand van met sensorgegevens die verkregen zijn tijdens meerdere vlieguren. De simulaties tonen een goede overeenkomst met de krachtmetingen en kunnen de kritische parameters van de parafoil met een bevredigende nauwkeurigheid voorspellen. De toolchain is numeriek voldoende stabiel gebleken en kan in de eerste ontwerpfase gebruikt worden voor de bepaling van de geometrie van de parafoil

en de lay-out van de verstevigingen. Ten slotte is een multidisciplinaire ontwerpopti-malisatie methodiek ontwikkeld voor een 2D niet-rigide vleugelprofielen met lokale ver-sterkingen. Het optimalisatieproces leverde een verscheidenheid aan profielvormen en verstevigingen, die de spanning in de ribstructuur minimaliseren en de "power harves-ting faktor" maximaliseren. De methode beschreven in het proefschrift levert diverse ontwerpcompromissen tussen maximale prestaties enerzijds en minimale vervorming van de ribben anderzijds.

1

INTRODUCTION

The International Energy Agency (IEA) regularly publishes global energy consumption and generation reports by countries and sources. Their latest information about global electricity consumption [1] states that the electricity consumption increased from 10.8 to 24.7 PWh between 1990 and 2018 with a steadily increasing growth rate. This increase is caused by the continuous expansion of the global economy and the need for more energy this entails. The higher living standards for many people in the western world and countries like China and India and the electrification of the transport sector is projected to increase the electric energy consumption even further. Next to electricity consumption, the report also states the contribution of electricity generation by sources. Fossil-fuel-based electricity generation totalled 67% in 2017, with coal contributing 40% of the total electricity generation while renewable electricity generation from hydro, photovoltaics and wind was approximately 25%. The IEA Energy Outlook 2020 [2] summarises the current situation as follows: "A lower future $C0_2$ emission with a current economy which is twice as large as in 2006 is a massive challenge, and technology is by far not the only factor to achieve net zero in 2050. Transport and housing sector electrification and behaviour changes are central to achieving this."

Due to the potential threat of climate change, the Intergovernmental Panel on Climate Change (IPCC) recommends a shift to renewable energy sources and a limitation and prevention of greenhouse gas emissions. This shift has already begun, as seen in the massive growth of renewable energy sources over the past 20 years. While wind energy electricity generation was at 4000 GWh in 1990, the generation in 2018 reached 1250 TWh [1], and the IEA predicts the total installed wind and photovoltaics capacity to surpass coal by 2024 [3]. Since the energy production of renewable energy sources depends on daytime and wind conditions, extra installed capacity and energy storage have to compensate for intermittency.

Jung et al. [4] assessed national and global wind resources under various wind turbine installation scenarios. They found that many countries have sufficient wind resources to satisfy their electricity consumption. However, their study results suggest that the current expansion rate of onshore wind energy is insufficient to cover global electric-

1
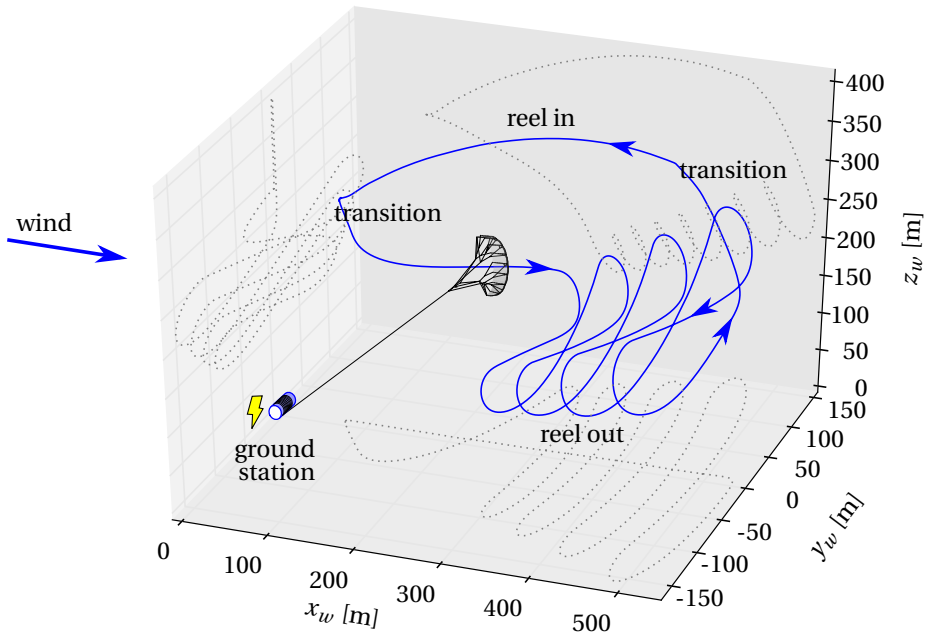
Figure 1.1: Illustrative pumping cycle flight path consisting of reel-out, reel-in and transition phases [6].

ity consumption in a reasonable time frame. The IPCC also advises further progress the technological aspects of renewables to further decrease the cost [5]. The growing need for more electricity and shift towards carbon-free electricity production methods has opened a market for renewables while most countries are forced to adapt their production accordingly. The demand for renewable energy also opens the field for alternative technologies in wind energy, such as airborne wind energy.

1.1. AIRBORNE WIND ENERGY

The purpose of this section is to introduce the reader to the topic of airborne wind energy (AWE) and highlight possible advantages compared to other renewable energy technologies and the shortcomings it entails. The basic idea behind AWE is to harvest energy from the wind using kites (tethered wings). The available wind power increases with the cube of the wind speed, and an airborne system may reach higher altitudes than modern wind turbines and provide access to more predictable winds that blow steadier and stronger at higher altitudes [7]. The research community and industry are currently investigating several system configurations. While the on-board generation configuration utilises wind turbines installed on the wing of a tethered flying device, the ground-based configuration utilises a tethered wing to drive a generator at the ground, either through a rotary movement of the tether or by using the kite's traction to drive a generator through unwinding the tethered from a drum. In Vermillion et al. [8] a full list of currently developed AWE system classifications can be found.

This work focuses on the ground-based power generation through kite traction. Fig-

ure 1.1 depicts the pumping cycle of an operating kite in crosswind during tether reel-out, transition, and reel-in phases. During reel-out, the kite is flown in a figure of eight trajectories while the tether is reeled out, producing electricity. When the kite reaches its maximum tether length, the kite is steered out of the wind window and the tether is reeled-in. After reaching its minimum tether length, the kite transitions towards the initial position before restarting the cycle. The net energy output of a complete power cycle can be improved by maximising the energy yield during the reel-out phase and minimising the reel-in time and power consumption, e.g. through depowering the kite.

Watson et al. [9] investigated the technology readiness level [10] of various alternative wind energy technologies including AWE. They concluded that the significant challenges for AWE are *high complexity, lack of proven reliability and operational hours*, and *limited knowledge* on the economic potential, i.e., whether the technology after total development yield the energy production it promised in theory. Also, a lack of experimental data to validate various models is mentioned, and based on the current challenges they evaluated a TRL 3-5, where 10 is the highest achievable mark. In comparison, floating wind turbines were put at 4-9, where the deviation originated from model and economic uncertainties.

Despite the challenges mentioned above, the technology provides several advantages compared to conventional wind turbines. Due to its low system weight the material reduction and increased mobility potentially saves cost. Also, a better adaptability to the wind resource by steering the kite to an altitude where the wind blows improves power output [11]. Particularly appealing locations are islands and places where seasonal weather events such as hurricanes inhibit the erection of conventional wind turbines. Also, deepwater offshore locations are appealing due to the force entry point on platform level.

1.1.1. TETHERED WINGS

So far, various technology demonstrators have been implemented, using of fixed-wing, hybrid or soft wings as depicted in Figure 1.2. Rigid wings are often made of carbon or glass fibre composites and are manoeuvred with aerodynamic control surfaces. The tethered flying device can be launched using a winch similar to a glider plane take-off or onboard propellers in vertical take-off mode. Fixed-wing kites can reach higher aerodynamic lift-to-drag ratios than soft kites due to high aspect ratio wings and very efficient wing profiles. Their aerodynamic efficiency allows for a small wing area, and fast manoeuvre flight envelopes. Fixed-wings are more expensive to manufacture, and autonomous landing a fixed-wing is one of the challenging aspects of this technology.

Soft wings are made of thin woven fabrics, and due to their flexible nature they are particularly difficult to simulate. Small changes in angle of attack may induce large structural deformations, which in return change the aerodynamic properties of the wing. Therefore, an aero-elastic model approach, based on fluid-structure interaction, is required to correctly determine the kite's shape during flight. The steering of a soft kite can be done autonomously by actuating bridle lines, which introduces an asymmetric pressure distribution and hence a rolling/yawing motion. Soft kites of the leading-edge inflatable (LEI) type combine a single skin canopy with an inflated tubular beam to define a lift-generating shape. The inflated beam stabilises the planform during the flight,

1

Figure 1.2: Soft, hybrid, and fixed-wing kite designs from various companies [12]. From left to right: SkySails Power, Kite Power, EnerKite, Ampyx Power, and TwingTec.

which makes them less prone to collapse compared to ram-air kites [13]. Bridle lines connected to the wing's trailing edge can be used to control the kite's pitch angle, which is helpful for depowering during the retraction phase. On the other hand, soft kites of the ram-air type consist of a double skin canopy inflated with air at stagnation pressure and their internal ribs provide an aerofoil shaped wing profile. In order to keep the wing stable during flight, both the top and bottom side of the canopy should be taut, which is accomplished by anhedral (span-wise arching), planform geometry and trim [14]. Compared to LEI kites, they can achieve higher glide ratios with their aerodynamic profile. By shortening various bridle lines in stages along each profile the angle of attack can be changed for depowering.

Each wing type has distinct advantages and disadvantages for AWE generation. Most soft kites have lower glide ratios than rigid wings due to their deformable wing profile, anhedral, and lower aspect ratio. Also, the bridle system introduces a considerable amount of aerodynamic drag, reducing the glide ratio. Nevertheless, soft kites compensate their lower glide ratio with a sizeable area-to-weight ratio, enabling large surface areas at low costs and low mass penalties which is important for upscaling the technologies. For AWE applications, the tether also plays a vital role in system scaling, and aerodynamic drag [15]. A longer tether enables the system to reach higher altitudes but conversely increases drag, reducing energy output. Fixed-wings have less drag than soft kites, and therefore suffer significantly more under the tether drag penalty. As a result, soft kites with a large wing surface may have a similar overall system performance compared to high glide ratio fixed-wings.

Fixed-wing kites are similar to conventional aeroplanes, and much of the know-how from the aerospace sector can be transferred into their design. Similarly, the fatigue loads acting on the wing during operation are comparable to the cyclic loads acting on wind turbine blades where glass fibre composites are used for manufacturing, and their design life is known to be many years of non-stop operation. Soft wings for paragliding or kite surfing, on the other hand, are not designed for either the load intensity or the number of load cycles that a kite during AWE operation is experiencing. Thus their manufacturing and design methods have to be developed and improved to withstand the wind loads and extend their design life. Also, UV degradation of the woven material is a crucial factor for design life.

1.1.2. COMPARISON TO CONVENTIONAL WIND ENERGY

Conventional horizontal axis wind turbines harvest wind currents and convert the kinetic energy into electricity. They consist of a large tower with a nacelle mounted on top where the generator is located. Usually, three blades rotate around the shaft covering a large swept area where the wind is harvested. With governmental subsidies and technological improvements, modern wind turbines became cost-effective and even the energy payback time of a modern 2 MW onshore wind turbine with a design life of 20 years in a farm configuration is approximately ten months [16]. Also, the overall sustainability compared to other energy sources such as coal and photovoltaics over its whole life cycle is ranked highest [17], whereas one of the technical challenges is the up-scaling of wind turbines which comes with heavier support structures such as longer blades and higher towers. The IEA predicts that the cost of onshore wind turbines may reduce by 15% from 2020 to 2025, but a faster expansion is mainly slowed by permitting difficulties and social acceptance [3]. For that reason, offshore parks are more attractive, but with the current technology, only sites with water depths not more than 40m can be accessed, which limits the park locations [18].

Airborne wind energy systems have distinct advantages compared to horizontal axis wind turbines. Most of the produced torque of a horizontal axis wind turbine comes from the blade tips where the tangential velocity is highest, and in order to provide the turbine with long blades, it requires a large and heavy support structure. On the other hand, an AWE system replaces the heavy support structure with a lightweight tether, which saves both material and cost. Additionally, due to the ground-based generator, no tower is required, and the root bending moment is minor compared to a horizontal axis wind turbine which could enable a more straightforward solution for floating offshore foundations. Without an extensive support structure, its transportation is cheaper and remote sites are accessible. In severe weather events, the kite can be landed and stowed away, which opens up hurricane sites where horizontal axis wind turbines cannot be erected.

The significant disadvantages of the AWE technology compared to conventional wind energy are the airborne system and the risk it entails, and the autonomous operation. The airborne system consists of the wing, bridle line system, tether and control pod. In case of a system anomaly during operation, e.g. due to a sensor/software or structural failure, the kite could lose control and crash. Also, the scenario when the grid connection is lost and the wind slows down can be fatal for soft wings because no apparent wind speed at the kite can be introduced by the winch/generator. For an autonomous operation, the system has to correctly react to each environmental change, such as wind gusts, thunderstorms, and wind direction/velocity changes. In case of a wrong decision or sensor error, the airborne system may immediately be jeopardised. For various strategies to improve system reliability and flight anomaly detection for AEW, refer to Salma et al. [19, 20]. On the other hand, a modern horizontal axis wind turbine has already been optimised such that it is less prone to critical failures. Their few degrees of freedom and constrained motion is less prone to environmental disturbances than a flying system with a practically unlimited number of degrees of freedom. These need to be controlled and measured with sensors to achieve reliable operation, and is technically more challenging, but it also bears a higher potential for reducing material use. Finally,

1

it should be mentioned that soft kites made of woven fabrics may suffer more under fatigue loads than glass fibre composites, thus finding a textile solution that resists the expected fatigue loads and UV radiation is a crucial part of life expectancy and system cost. Whether the aforementioned technological challenges will be overcome and AWE becomes cost-effective is still unknown at the time this thesis was written.

1.1.3. SKYSAILS POWER
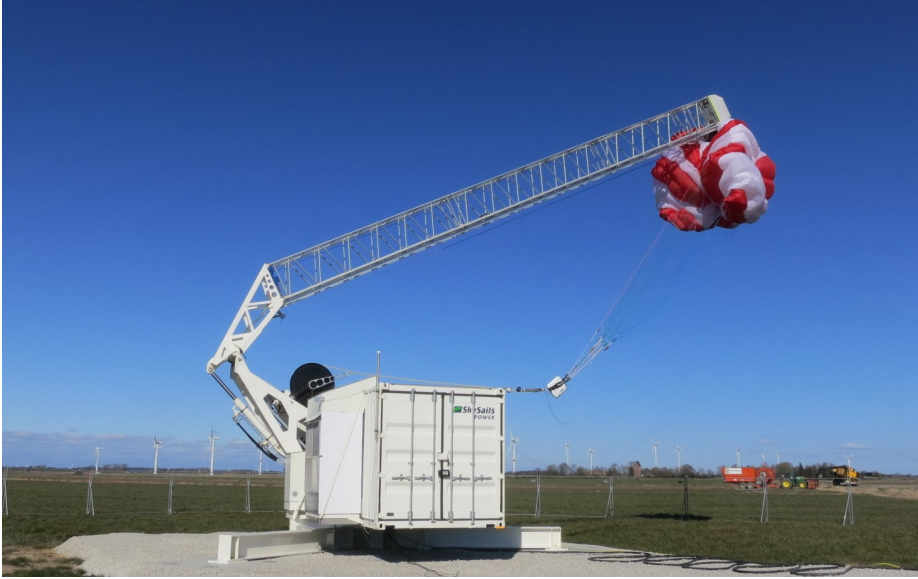
Figure 1.3: SkySails Power PN-14 system with reefed kite and retracted mast.

SkySails Group GmbH is based in Hamburg, Germany, and initially developed a kite traction system for bulk freighters and other marine vessels to reduce fuel consumption. The system uses a soft kite that is flying crosswind manoeuvres, producing several tonnes of traction to pull the ship. Since 2011, power systems for ground-based electricity generation are being developed utilising ram-air kites, steered with a remote-controlled control pod suspended below the wing. The most recent system is an onshore power generator with a tether thickness of 14mm. The 200kW generator is placed inside a 30ft shipping container attached to a foundation via a gear ring allowing the container to rotate 360 degrees to adjust to the changing wind direction. A mast is attached to the container's backside, on which the kite is docked during ground handling and launching and landing.

During launch preparation, the mast is rotated towards the ground, and the reefed kite can be attached to the tip of the mast as shown in Figure 1.3. When the mast is erected and the kite un-reefed, the wind fills the kite with air until it reaches an inflated state, see Figure 1.4. It can be seen that the kite has two attachments to the container, the main tether at the control pod underneath the wing and the leading edge connecting the tip of the mast via a reefing line. During the launch, both tether and reefing lines

Figure 1.4: SkySails Power PN-14 system with inflated kite connected to mast.

are reeled out, and the kite is allowed to climb to higher altitudes, see Figure 1.5a. Once the kite reached a safe altitude, the reefing line is connected to the main tether with an adapter. During the kite's operation, as depicted in Figure 1.5b, it is flown in figure of eight trajectories pulling the tether from the generator's drum and produce electricity. The generator acts as a winch during reel-in and pulls the kite towards the ground station, where the pumping cycle repeats. During landing, the reefing line adapter is removed from the main tether and moves to the tip of the mast. Then, both tether and reefing lines pull the kite towards the ground station until the kite docks with the mast and can be reefed for ground handling.

1.2. MOTIVATION FOR THIS THESIS WORK

The challenge in the structural layout of flexible kites for AWE applications during reel-out phase is to ensure a good aerodynamic performance to maximise tether tension, sufficient manoeuvrability, steering initiated with little force, and sufficient structural integrity such that the kite does not fail during operation. On the other hand, during the reel-in phase, the kite should produces as little traction as possible, while maintaining manoeuvrability and stability to avoid negative angles of attack. Like in most engineering applications, a trade-off between these features has to be made. During the development cycle of SkySails' kites, it became apparent that the structural and performance characteristics of the kite prior to field testing was challenging to estimate using simple analytical modelling approaches. Additionally, the flexible nature of ram-air kites causes the wing to deform during flight and behave substantially different compared to fixed-wings. Therefore, advanced simulation techniques which capture the aero-elastic effects that govern the flight dynamics of the kite are required to obtain reliable results, that can be used to motivate design choices. The motivation for this work is to create

1

(a) Kite during take-off.   (b) Kite during flight.

Figure 1.5: SkySails Power PN-14 system.

such a simulation environment to assess the kite during operation for both structure
and aerodynamics and potentially accelerate design changes during initial design.

1.3. THESIS OUTLINE

The thesis is structured as follows. First, a general description of ram-air kites and sim-
ulation approaches found in the literature is presented in Chapter 2. The derivation of
the finite element model for thin-walled membrane structure used to simulate the kite is
described in Chapter 3. In Chapter 4 the developed aero-elastic model is presented, and
its capabilities are verified with analytical and numerical models from literature, and a
model validation on the basis of measurements taken during flight is shown. Finally, a
multidisciplinary design optimisation on a ram-air kite rib is presented in Chapter 5.

2

LITERATURE REVIEW

In this chapter, the tethered parafoil used for AWE applications is introduced in more detail, and modelling approaches found in the literature are presented and discussed critically, and based on the findings, the research questions are formulated. The term parafoil and ram-air wing can be used interchangeably as both describe a tensile membrane structured wing consisting of multiple cells which are inflated by the relative airflow. Domina Jalbert invented the parafoil in 1964 and patented his invention in 1966 as a "Multi-cell wing type aerial device" [21]. The parafoil design was introduced as a parachute with better steerability and glide performance compared to the round canopy parachute. Its applications vary from sports like paragliding, motor paragliding, and kite surfing, to military precision aerial delivery and space craft decelerators. With their glide performance and lightweight structure they are also attractive for AWE applications.

2.1. PARAFOILS

Figure 2.1 depicts the frontal view of a parafoil wing, also known as a canopy, which consists of several individual cells enclosed by the top and bottom panels and internal ribs. While ribs provide the aerodynamic profile shape in chord direction and space for bridle line attachment points (LAPs), the top and bottom panels connect two neighbouring ribs and form the wing's skin. Intakes positioned at the leading edge of the wing allow the relative airflow to enter the nonrigid structure, inflate it, and form the wing geometry, and with holes in each rib called cross-ports, the internal pressure is distributed inside the wing. Most parafoils have a varying arc-anhedral between each neighbouring rib, which results in a C-shaped arc along the wing's span such that the wing tips point towards the ground.

The bridle line system of parafoils consists of cascades of interconnected lines starting with upper lines attached to ribs, see Figure 2.2. The bridle line closest to the leading edge is called A-line while the following lines towards the trailing edge follow the same convention (B, C, D). The upper bridle lines are then connected to (fewer) lower bridle lines that connect to riser lines that eventually connect the pilot's harness or the control pod. Control lines at the trailing edge allow the pilot to steer or brake during flight.

2
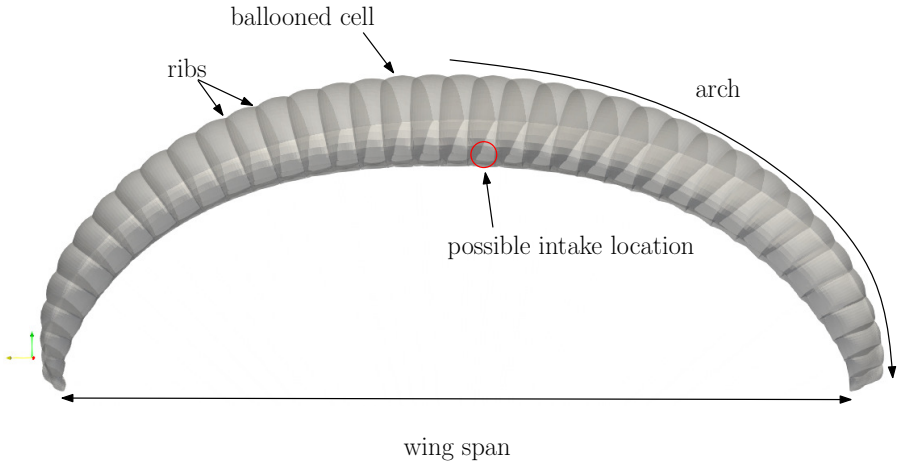
Figure 2.1: CAD model of the inflated ram-air wing.
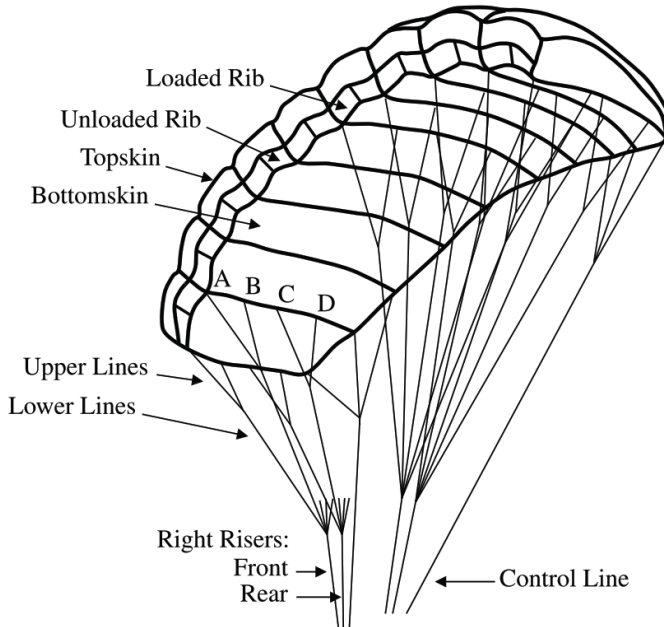
Figure 2.2: Components of a parafoil by Dunker [14].

All aerodynamic forces are transmitted through the bridle line system, and in the case of a tethered system, the forces act on the ground station through the tether. Besides transmitting loads, the bridle lines also maintain the planform shape and allow steering control inputs.

A parafoil's trim is defined as the pilot's (or control pod's) chord-wise position with
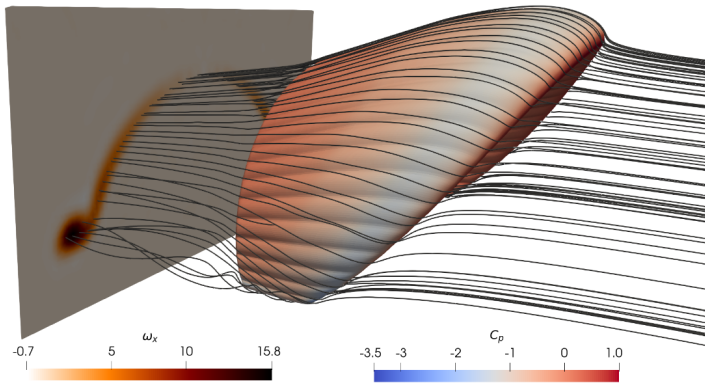
Figure 2.3: Simulated ram-air wing showing streamlines on the suction side and tip vortices indicated by the vorticity component ω_x, found in Folkersma et al. [22].

respect to the centre rib. The trim has a significant influence on the flight performance - a forward trim position reduces the angle of attack and, therefore, both lift and drag. On the other hand, a backwards trim position increases lift and drag. Both forward and backward positions are constraint by stability. The kite becomes inherently unstable and stalls and collapses if the trim is positioned outside those bounds. While a canopy collapse due to a forward trim is called front stall, the back stall occurs when the trim is moved too far aft. The optimal trim is usually found experimentally, and modern paragliders can change the trim position during flight to improve performance during certain manoeuvres. To reduce line drag and keep the bridle system aerodynamically efficient the number of bridle lines is kept at a minimum.

The aerodynamic pressure distribution on a ram-air wing during cross-wind flight is comparable to conventional fixed-wings. Figure 2.3 depicts the streamlines on a simulated ram-air wing using computational fluid dynamics [22]. The streamlines are not aligned with the rib profiles close to the wing tips due to the wing's arc anhedral. At the wingtips the flow produces a tip vortex, also indicated by the vorticity. Due to the flexible nature of a ram-air wing its ribs also deform during flight. At approximately quarter chord, where the pressure reaches its minimum, the profile is stretched towards the low-pressure peak, causing a reduction in section-wise glide ratio [23].

An essential attribute for ram-air kites is wing loading. For a free-flying paraglider it is defined as the total weight of the kite including payload divided by the projected surface area, and is a measure of how much weight per unit area the wing has to carry. A modern paraglider with a projected surface area of 20 m^2 and a pilot weight including harness and kite of approximately 120 kg has a wing loading of 59 N/m^2. In case of a reentry parafoil for spacecraft while landing, the wing loading is around 200 N/m^2 [24], and ram-air wings for precision aerial delivery may reach up to 720 N/m^2 [25]. During steering manoeuvres, this load usually increases by a factor of 2-6 depending on the turning radius and the resulting inertial forces. A tethered wing used for AWE applications has to withstand all force acting on the structure during operation. While gravitation and inertia act on the wing, the aerodynamic forces dominate during the traction phase. A

2

(a) SkySails kite system schematic showing canopy, bridle line system and control pod [26].

(b) Schematics of steered kite with indicated passive (red) and fixed (blue) bridle lines and skewed lift vector [27].
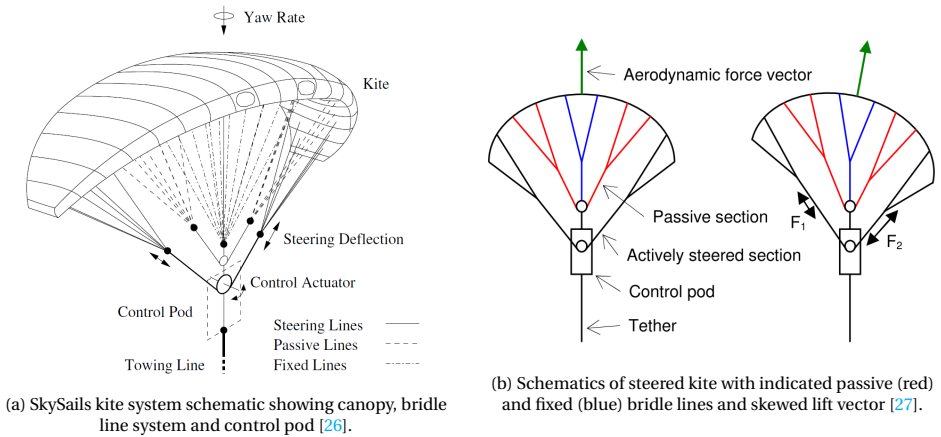
Figure 2.4: SkySails kite steering approach.

current SkySails Power parafoil with a projected surface area of 100m^2 and a pulling force of 60 kN experiences a wing loading of 490 N/m^2 during the traction phase. While ram-air wings for aerial delivery purposes are designed to withstand a single drop, AWE kites have to withstand thousands of power cycles which poses a significant challenge for the structural design and manufacturing of such wings. The wing's highly loaded parts are the panels at the suction side of the first quarter chord and the ribs, which transmit all aerodynamic pressure loads through the line attachment points (LAPs) into the bridle system. The point force introduction at each LAP necessitates a reinforcement on the rib to avoid tearing and extensive deformation of these highly loaded parts. For a more detailed description of the ram-air kite design philosophy, refer to Dunker [14].

The steering of parafoils can be achieved by deforming parts of the wing or moving the pilot's position in span-wise position. A paraglider is steered by pulling braking lines to move a trailing edge section of the wing downward that increases lift and drag locally. The resulting coupled yaw and roll rates then produce a turn and banking of the paraglider. SkySails, on the other hand, adapted the steering method of moving the control pod in span-wise direction. Its steering mechanism is depicted in Figure 2.4a. Here, the kite with bridle line system and control pod is shown. The bridle line system is split into three span-wise sections: fixed lines located in the centre, passive lines between the wing's centre and the tip section, and steering lines connected to the wing tips. The actuator located in the control pod is connected to both tip sections of the wing, and by actuator movements the control pod moves towards a wing tip. At the same time, the passive lines can freely move around the pulley located above the control actuator (indicated as a smaller white disk). The resulting steering motion is indicated in Figure 2.4b. It can be seen that the control actuator has to overcome a force difference given by the two tip sections, and when actuated, the aerodynamic force vector introduces a roll and yaw motion. There are two distinct advantages with this steering approach: the canopy is barely deforming during the steering motion which increases the life time expectancy, and the control actuator only has to overcome the force difference acting in both wing

tips that usually stays below 2.5% of the tether force [27].

2.2. TETHERED CROSSWIND FLIGHT

The dynamics of a tethered parafoil are inherently different from a free-flying wing because the tether constraints the flight trajectory. Also, the kite's flight velocity is mainly determined by its glide (lift-to-drag) ratio and the wind speed, whereas its weight plays a minor role during the traction phase because gravitational and inertial forces of a lightweight membrane kite are small compared to the pressure forces by the canopy. The theoretical energy output of crosswind flight was first derived by Loyd [28]. A similar approach with a simplified set of equations of motion used in this work, derived in Erhard et al. [26, 29], requires the following model assumptions:

1. The aerodynamic forces are large in comparison to the system mass such that external changes by the wind field and steering produce very high accelerations, which immediately adjust the kite to a quasi-steady equilibrium state.

2. The kite is oriented with the relative airflow such that no side-slip occurs.

3. The wind field is uniform and constant.

4. The tether is assumed as straight and inelastic.

Figure 2.5a shows a tethered kite in cross-wind flight with wind coordinate system $(\mathbf{e_x}, \mathbf{e_y}, \mathbf{e_z})$, where $\mathbf{e_x}$ is aligned with the wind direction. Unlike in a usual spherical coordinate system, neither elevation nor azimuth angle are used. Instead, two angles ϑ and φ, and the tether length L_t are used to describe the kite's location. The angle ϑ spans between the tether and $\mathbf{e_x}$, whereas φ is the angle between $\mathbf{e_z}$ and the projected tether on the $(\mathbf{e_y}, \mathbf{e_z})$ plane. A local body reference frame located at the centre of mass, which is assumed to be located at the control pod, spans three unit vectors $(\mathbf{e_{roll}}, \mathbf{e_{pitch}}, \mathbf{e_{yaw}})$. Additionally, a heading angle ψ (not shown in the figure) spanned between $\mathbf{e_x}$ and the $\mathbf{e_{roll}}$ uniquely defines the kite's orientation with respect to the wind oriented coordinate system, i.e. $\psi=0$ when the kite is orientated toward the wind direction. The velocity vectors shown in the figure are the wind velocity vector $\mathbf{V_w}$, the tether reeling velocity vector $\mathbf{V_t}$, and the kite's velocity vector $\mathbf{V_k}$, respectively. With the assumptions mentioned above, a set of equations of motion is derived in Erhard et al. [29], and the most relevant equation used in this work is

$$V_a = E(V_w \cos\vartheta - V_t). \tag{2.1}$$

Here, V_a is the apparent wind speed the kite experiences, and it is dependent on the airborne system's glide ratio E, wind speed, tether orientation angle ϑ, and the tether reeling speed V_t. This equation is used in Chapter 4 to determine the kite's glide ratio during flight with the help of two vane anemometers to measure the apparent wind speed at the control pod, a LIDAR systems to measure the wind speed at flight altitude, and a rotary encoder located at the ground station to measure ϑ.

Next, the tether force expression is derived from a force balance depicted in Figure 2.5b. The resultant aerodynamic force vector $\mathbf{R_k}$ acts in the direction of the tether orientation. The vector can be split into its lift $\mathbf{L_k}$ and drag $\mathbf{D_k}$ components and the apparent

(a) Kite in cross-wind flight described by spherical wind-oriented coordinate system.

(b) Aerodynamic forces (red) acting on the kite. The angle of attack is defined as the angle between the centre rib's chord line and the apparent wind speed vector.
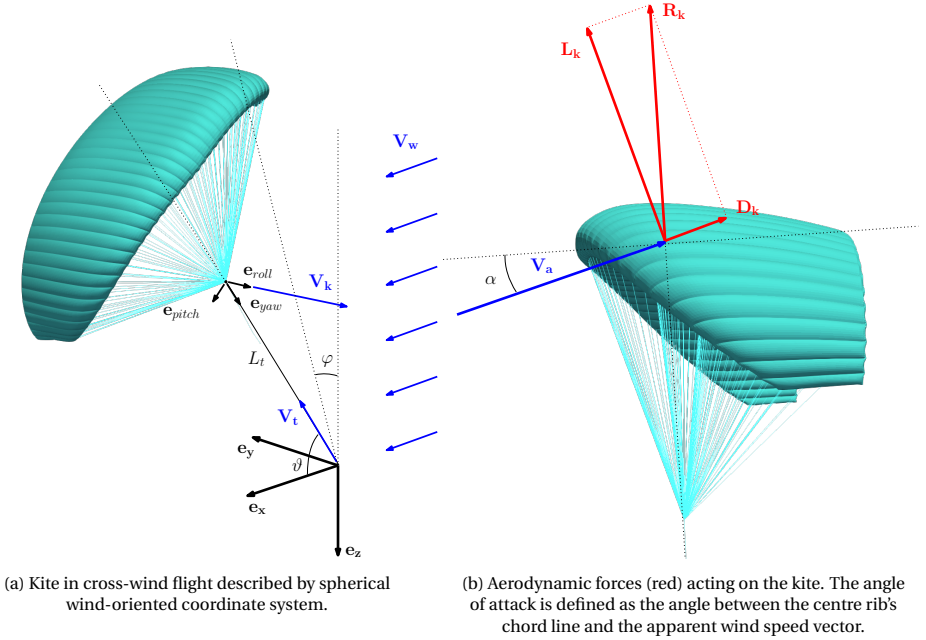
Figure 2.5: Kinematic and force diagram of kite in cross-wind flight.

wind velocity vector is oriented with an angle of attack α with respect to the centre rib's chord line. Using the standard formulation of aerodynamic lift force, the magnitude of the aerodynamic force produced by the parafoil is equivalent to

$$R_\mathrm{R} = C_\mathrm{R} \frac{1}{2} \rho V_\mathrm{a}^2 S_\mathrm{proj}, \tag{2.2}$$

where ρ is the air density, S_proj the parafoil's surface area projected on the $(\mathbf{e}_\mathrm{pitch}, \mathbf{e}_\mathrm{roll})$ plane, and C_R is the resultant force coefficient determined by

$$C_\mathrm{R} = \sqrt{C_\mathrm{L}^2 + C_\mathrm{D}^2}. \tag{2.3}$$

Both glide ratio and resultant force coefficient play a crucial role in describing the aerodynamic performance of a parafoil and will be used extensively in this thesis. For maximising the power output in the cross-wind flight Loyd introduced the power harvesting factor ζ, which is defined as

$$\zeta = \frac{P}{P_\mathrm{area}}, \tag{2.4}$$

where P is the extracted power from the wind and P_area is the available wind power that flows through a cross-sectional area equivalent to the kite's surface area. Loyd con-

cluded, that the tether reeling speed should be 1/3 of the wind speed to maximise ζ. In that case

$$\zeta_{\max} = \frac{4}{27} C_R (1 + E^2).$$ (2.5)

2.3. ANALYTICAL APPROACHES

In this section, a collection of analytical approaches to various parts of the parafoil are derived and later used for the computational model.

2.3.1. BALLOONING

A parafoil is an inflatable membrane wing with inlet openings close to the leading edge. The wing is fully inflated when the internal pressure is higher than the pressure surrounding the wing. The billowing of the panels is called ballooning, and the further apart the ribs are located, the more drastic the ballooning effect becomes, and thus the profile shape deviation from the actual rib profile. Within a good parafoil design, a non-rectangular panel geometry is used to shorten the rib-to-rib distance at specific locations along the chord, and as a result, introduces a three-dimensional profile shape between the ribs, which nearly resembles the rib profile. A proper three-dimensional shaping becomes more challenging to achieve for highly loaded wings where the suction side of the wing is experiencing large deformations. These large deformations can be controlled with local reinforcements, such as additional seams positioned on the panel or simply thicker fabrics.

If insufficient air is fed though the intakes, for example, when the intakes are not located in the stagnation zone due to a high or low angle of attack, the parafoil might deflate and collapse. Therefore a good positioning and dimensioning of the intakes is a crucial step in parafoil design. Also, kites with a high permeability constantly lose internal pressure though leakage flow through the fabric and sewing lines which drastically reduces the flight performance. A simple approach to estimate the internal pressure is to assume that the flow comes to a rest once it entered the wing and is equivalent to the stagnation pressure. This assumption does not hold for parafoils with many intakes positioned along their span because a vortex forms around each intake that heavily influences the local pressure [30, 31]. The SkySails parafoil under consideration only has only two intakes, and therefore its influence on the overall flow field is less pronounced and assumed to be negligible. With the assumption, that the internal pressure is equivalent to stagnation pressure it can be formulated as

$$p_{\text{int}} = \frac{1}{2} \rho V_a^2.$$ (2.6)

The external pressure is influenced by the aerodynamic profile shape and varies over the wing's surface. To formulate a resultant pressure expression for the structural finite element solver, where both internal and external pressure are combined, the pressure coefficient is used. The pressure balance at each location on the wing's surface than becomes

$$C_\text{p} = C_\text{p, aero} - C_\text{p, int} = C_\text{p, aero} - 1, \tag{2.7}$$

where C_p is the resultant pressure coefficient acting on the kite's membrane, and $C_\text{p, aero}$ is the pressure coefficient determined by the external flow. The pressure coefficient at stagnation pressure is by definition one, and consequently, the resultant pressure coefficient at the stagnation point becomes zero.

2.3.2. PANEL STRESS

A simple method to approximate the mechanical stress acting on the canopy is assuming each panel as part of a cylindrical pressure vessel. An expression for the axial and tangential stress in a pressure vessel was derived during the industrial revolution by Peter Barlow. He found a geometrical expression for the stresses applicable to thin-walled cylinders under plane stress with small strains. Figure 2.6a illustrates the profile of a pressurised cylinder with its axial σ_a and tangential σ_t stress components. Considering the definition of pressure as normal force per unit surface

$$p = \frac{F}{A_0} = \frac{F}{L2R}, \tag{2.8}$$

where F is the acting force on the cylinder profile area A_0, the product of length and diameter. The radius R is the average between the inner and outer radii, a fair assumption for thin-walled structures. Similarly, the tangential stress is expressed as

$$\sigma_\text{t} = \frac{F}{2Lt}, \tag{2.9}$$

where t is the cylinder wall thickness. Combining both Equations 2.8 and 2.9 results in the expression for the tangential stress, known as Barlow's formula

$$\sigma_\text{t} = \frac{pR}{t}. \tag{2.10}$$

The ballooned shape of a parafoil cell is depicted in Figure 2.6b, and it can be seen that only the upper and lower part of the cell is curved and due to the pressure differential across the membrane. On the other hand, the ribs are pressure-free because the air may flow freely between each cell through cross-ports. In order to obtain a simple estimation of panel stress, the local curvature R and pressure p are required. The local curvature for each chord-wise location can be approximated by placing the centre of curvature into the middle of the section as shown in Figure 2.6b, while the pressure can be determined in conjunction with Equation 2.7. With this approach, the local curvature is solely a function of local rib height h and panel width w_0, which corresponds to the circumference of the pressurised panel. In Chapter 4 this analytical expression is compared to the numerical results obtained by the developed parafoil model.

2.3.3. LINE DRAG

The line drag of the parafoil bridles constitutes a considerable amount of drag which has to be included in the model to determine the aerodynamic characteristics of the entire airborne component correctly. Determining the drag coefficient of the bridle lines

(a) Pressure vessel profile indicating tangential and axial stress components.

(b) Span-wise cut through kite cell. Vertical lines correspond to ribs and arcs depict ballooned panels connecting two neighbouring ribs.
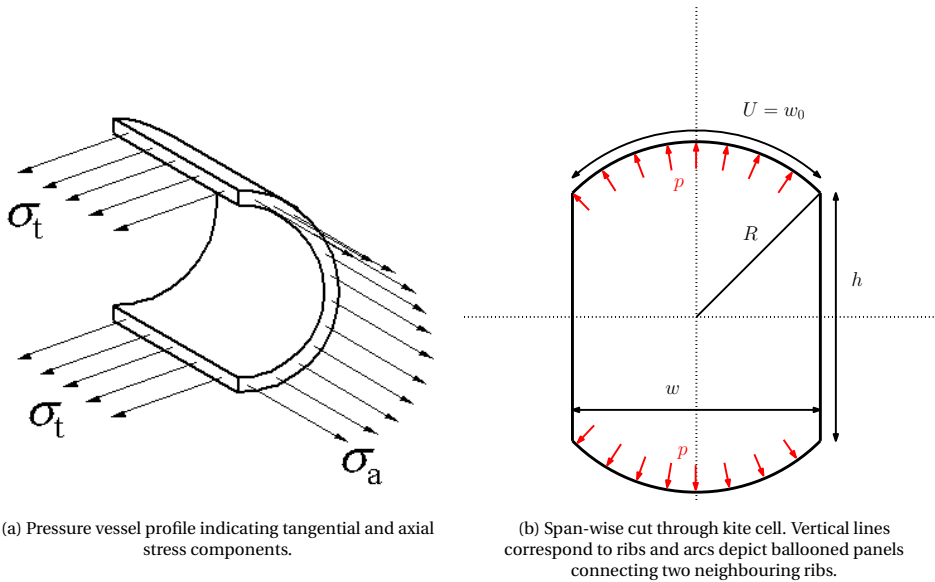
Figure 2.6: Analytical stress depiction due to ballooning.

during flight is not trivial due to dynamic flow effects such as vortex-induced vibration, which cause the airflow to locally separate around the bridle. The vortex-induced frequency can be described with the non-dimensional Strouhal number. A lock-in phenomenon between bridle line and flow occurs when the Strouhal number is close to the bridle's natural frequency such that the bridle starts to oscillate in resonance. This effect of aero-elastic nature can often be heard during the flight in the form of a whistling sound.

The drag coefficient of a static cylinder was experimentally determined in a wind tunnel by Delayn et al. [32]. In Reynolds number ranges between $1 \cdot 10^3$ and $1 \cdot 10^5$, the drag coefficient of a cylindrical object varies between 1 and 1.2. A sudden drop in drag coefficient to approximately 0.25 is observed at a Reynolds number of $3 \cdot 10^6$, which is caused by an effect called drag crisis, which occurs when the boundary layer around the cylinder changes from the laminar to the turbulent flow regime. The turbulent boundary layer also causes vortex shedding. This effect only occurs around a small range of supercritical Reynolds numbers (between $3 \cdot 10^6 - 6 \cdot 10^6$), whereas the drag coefficient increases again for higher Reynolds numbers. In the case of bridle lines and tether, the Reynolds number lies in the range of $1 \cdot 10^3$. Thus, the drag crisis effect is of no importance.

Kite bridle line drag has been characterised experimentally by several researchers using different line profiles, tension, and angles of attack. Bergeron et al. [33] determined a bridle line drag coefficient of approximately 1 for a cylindrical bridle line profile and 0.68 for elliptical profiles in a set of wind tunnel experiments using a range of tensions within the operating range of a round parachute. Jung [34] tested bridle line latex coating and compared their drag coefficient with non-coated bridle lines and concluded that non-coated bridle lines have a 50% higher drag coefficient. Dunker et al. [35, 36] tested

various profile geometries in a wind tunnel setup and concluded that the Strouhal number has a significant impact on the pressure drag of the bridle lines, increasing their drag by up to 300% for specific Reynolds numbers. Also, the profile geometry can reduce the induced vibration impact, e.g. by introducing a helical strake coating that circumvents lock-in. Siefers et al. [37] tested an inclined flat Dacron line in a wind tunnel setup and found that the drag coefficient was lower for the inclined lines than for lines perpendicular to the flow measured in previous work. However, they reported an inherent variability in test results which could be reduced by applying a higher tension. They concluded that neither Reynolds number nor small angles of attack tend to affect the drag coefficient significantly. The studies mentioned above show the intricacies of wind tunnel tests and how many factors like material, tension, angle of attack, and Reynolds number can affect the drag coefficient. The effective drag increase by vibrating bridle lines is out of scope of this thesis, and are therefore treated as a subscale process. Instead, an analytical approach is adopted to determine the drag coefficient of bridle lines which is based on Hoerner [38] who derived a simple formulation for lift and drag coefficients of an inclined cylinder as

$$C_L^{\text{cylinder}} = C_\tau \sin^2(\Theta) \cos(\Theta),$$ (2.11)

and

$$C_D^{\text{cylinder}} = C_\tau \sin^3(\Theta) + C_f,$$ (2.12)

where C_τ is the drag coefficient in normal direction with respect to the cylinder surface, C_f is the shear drag coefficient and Θ the angle between tether and flow direction. For this work, a normal drag coefficient of 1.1 and a shear drag coefficient of 0.02 is assumed, corresponding to values found in the literature mentioned above.

The tether drag plays a crucial part in the total drag of a tethered wing. The longer the tether and the faster the kite flies, the higher the contribution of the tether drag, which reduces the effective glide ratio. Argatov et al. [39] derived a simple analytical lumped drag expression for the tether drag in an AWE system by integrating the aerodynamic force over the tether length L, thus an approximation of the tether drag

$$\mathbf{F}_{\text{tether}} = \frac{1}{8} \rho d L C_D^{\text{tether}} V_a^2,$$ (2.13)

where d is the tether diameter. The resulting effective glide ratio of the airborne system then becomes

$$E = \frac{C_L^{\text{wing}}}{C_D^{\text{wing}} + \frac{C_D^{\text{tether}} d L}{4 S_{\text{proj}}}}.$$ (2.14)

2.4. MODELLING APPROACHES FOR MEMBRANE STRUCTURES

The thin membrane fabric used for parafoils exhibits distinct mechanical responses to tension, compression, shear, and bending loads. It practically poses no resistance to
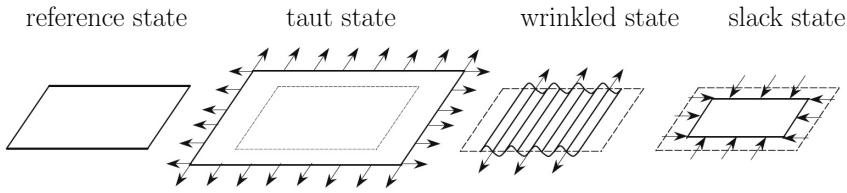
Figure 2.7: Different membrane states - reference, taut, wrinkled, and slack [41]

neither compression nor bending loads, and if a thin fabric is uni-axially loaded in tension, the membrane tends to wrinkle along the direction in which the load is acting. In the past 50 years form finding methods have been extensively developed which find the mechanical response of thin membrane structures under a given load, and the most significant solution methods are stated in this section. The mechanical response of membrane structures is nonlinear in various ways and often solved using the finite element method. Due to large translations and rotations during form finding the Green-Lagrange strain formulation is used and it is nonlinear in the sense that the solution has to be found in several solution steps. Another source of non-linearity is the pressure load acting normal on the membrane's surface. When the structure deforms, the membrane's surface orientation changes, and the pressure load direction has to be reevaluated for the deformed state. Also, membrane materials often consist of woven material which is a complex structure by itself and it exhibits nonlinear stress-strain behaviour and a stiffness depending on load direction [40]. And finally, due to the negligibly small bending and compressive resistance a wrinkling model is often introduced in the analysis to avoid refined finite element meshes.

2.4.1. NON-COMPRESSION MODEL

Wrinkling is a local buckling phenomenon dependent on the membrane's stress and strain state. Figure 2.7 depicts all three possible states a membrane can adopt: taut, wrinkled, and slack. A taut membrane is in tension along both principal axes and behaves like a shell. As soon as the stress along one principal axis becomes negative while stress positiveness is kept along the other axis, wrinkles form along the positively stressed axis while the membrane contracts perpendicular to the same axis. The slack state occurs when both principal axes are in compression, leading to an in-plane collapse of the membrane. Shell elements with bending stiffness can be used to simulate membrane structures, but the size of the smallest shell element has to be equivalent to the size of the smallest wrinkle to find the deformation field correctly. A fine mesh often leads to a long computation time and shows details that might be of no interest.

For that reason, non-compression models have been developed which do not compute the shape of individual wrinkles or their out-of-plane deformations but rather determine the in-plane contraction due to wrinkling based solely on the stress state. Wagner was the first to develop such an approach in 1929 called Tension Field Theory, where the structure is assumed to be in a purely tensile state [42]. Based on this approach, the wrinkle direction and in-plane contraction for simple geometries and load cases can be determined. The original approach by Wagner has been considerably improved and

2

reformulated into a more sophisticated mathematical form.

A considerable contribution to the analysis of membrane structures originates from the form-finding of cable nets, grid shells, and pre-stressed fabric membranes. Schek [43] developed the force-density method to find the equilibrium state of a net structure, e.g. representing membrane structures. Barnes developed a form-finding method based on Dynamic Relaxation with variable mass terms to critically damp the structure until an equilibrium is found [44, 45]. A simple element-wise stress update strategy is employed to correct for compressive stress. The method is numerically stable even if slack regions and highly nonlinear structural responses form during the solution procedure and the numerical implementation is simple. A round-robin analysis in 2013 compared various solvers from companies and institutes to understand the current state of analysis used for tensile structures [46]. Several form-finding and load analysis problems were solved, and critical values of stress, deflection and reaction were compared. It was found that the results show high variability due to different solving procedures and material models being employed.

Roddeman developed a wrinkling formulation based on a modified deformation tensor which corrects the stress state when wrinkling, or slackening occurs [47, 48]. In geometrically nonlinear analysis, the method can be used for both isotropic and anisotropic materials. A good agreement between analytical and numerical results from a simple shear test have been reported. Despite the validity of his method, the stiffness matrix becomes singular in regions of slackening, and a step method for the iterative solution procedure is recommended.

Several researchers have further developed Roddeman's modified deformation tensor. Rossi et al. [49] applied the stress state correction to a dynamic formulation to solve several problems such as an inflated airbag and a sheared membrane. They proposed an element-wise stress update strategy such that the compressive stress component is eliminated by rotating the stress tensor into its principal wrinkle direction and then updating the corresponding internal forces for the given element. The method caused numerical instabilities due to abrupt changes in the stress field, and a penalty factor was therefore introduced to reduce state switching of individual elements. Jarasjarungkiat et al. [41, 50] further developed the penalty factor formulation as a function of the current stress state and expanded the model to become applicable to orthotropic material. Another wrinkling model developed by Raible et al. [51] applies to both isotropic and anisotropic material. Its formulation is similar to the previously mentioned methods, which are based on an element-wise stress update strategy and with a principal strain-based formulation, the convergence behaviour has been improved for orthotropic materials.

Pipkin [52] focused on a strain energy formulation where the absence of compression is directly incorporated into the variational formulation. The strain energy function is re-written into a relaxed strain energy formulation, and it is shown to be a convex functional of the deformation gradient. Steigmann et al. [53] applied the relaxed strain energy formulation to an inflated tube, and the most recent advance in applying a variational formulation to membranes was conducted by de Rooij et al. [54]. They developed a finite element formulation for membranes with incorporated relaxed strain energy function and solved the nonlinear system with the interior-point method. Many

mechanical problems were solved, and the method proved to be numerically stable and efficient.

This section showed that several approaches to find the deformation and stress field of a loaded membrane structure had been developed in the past. The most suitable methods for this work apply to both isotropic and orthotropic materials because many fabrics used in the parafoil industry are orthotropic. Therefore, methods developed by Jarasjarungkiat [41, 50] and Raible [51], which both works on orthotropic materials, are tested in this work.

2.5. FLUID-STRUCTURE INTERACTION APPROACHES

As identified in the previous sections, a ram-air kite is an inflated tensile structure consisting of thin fabric and bridle lines with negligible bending stiffness. The kite shape during flight results from the difference in air pressure of internal and external pressure fields, and with a variation in the angle of attack or flight speed, the shape might change considerably. From a modelling point of view, the geometry cannot be found unless the aerodynamic pressure distribution is known, and the pressure distribution cannot be determined unless the shape is known. This coupling can be solved using the fluid-structure interaction approach, which simulates both fluid and structure as subsystems and exchanges information on the interface and is the modelling approach of this work.

2.5.1. PANEL METHOD

A simple aerodynamic approach is the *panel method* based on the potential flow assumptions. The lifting surface is discretised into panels, and the source-sink terms for given boundary conditions are computed. This method applies to flows that are irrotational, steady, and inviscid (Reynolds number approaches infinity). Several studies [55–57] used a nonlinear finite element software to model the structural response of a ram-air kite to the pressure field obtained by a panel method. The advantage of this method is its fast computation compared to a complete CFD analysis. Also, no finite volume mesh has to be built, which often is tedious to obtain, and its quality has a significant impact on the solution accuracy. On the other hand, results obtained by the panel method may diverge from reality when modelling flows with high angles of attack where flow separation occurs, and the assumption of irrotational flow becomes invalid. This constraint is important to note because soft kites for AWE applications are often flown at higher angles of attack to maximise their pulling force during cross-wind manoeuvres [13].

A complete dynamic approach with a staggered FSI scheme was taken by Ortega et al. [58] which consisted of a cost-effective low-fidelity panel potential flow solver with deforming wake and an explicit dynamic solver with wrinkling model and viscous damping for numerical stability to determine the ram-air kite's shape. They tested the solver on a free-flying parachute payload configuration with and without deflecting steering lines and compared the system's velocity and glide ratio with measurements that showed satisfactory results. The shortcomings of their method were the absence of viscous drag acting on the payload and canopy and internal canopy flow, which affects the total drag due to the intakes. Despite the shortcomings, they presented a simple FSI model for analysis of parachutes, and in a more recent publication [59], they improved their panel

solver with a flow separation model and applied it to analyse the aero-elastic response of a blunt inflatable building.

The most recent publication on aerodynamic modelling using the panel method was done by Castro-Fernández et al. [60]. They tested their in-house unsteady panel solver on a delta wing kite during a figure of eight manoeuvre and compared their obtained aerodynamic coefficients with a measurement approach introduced in Borobia-Moreno et al. [61]. They concluded, that a quasi-steady aerodynamic approach, compared to a steady and unsteady approach, is sufficiently accurate to model the lift coefficient during the figure of eight manoeuvre. Additionally, their obtained drag coefficient was lower than the measurement due to the absence of viscous drag, and the moment coefficient had the same order of magnitude compared to the measured data but no clear trend between them could be seen. Their quasi-steady model can be run with a time stepping of 10 ms and a full figure of eight trajectory was obtained in less than 30 minutes.

2.5.2. Computational Fluid Dynamics

A pure aerodynamic analysis on two-dimensional single-cell rigid aerofoils with and without intake was investigated by several researchers [30, 62–64]. All utilised the Reynolds-Average Navier-Stokes (RANS) equations and various turbulence models. A comparative study between the aerodynamics of the two aerofoils was carried out, and it was found that the intake primarily influences drag. The intake causes the flow to separate much earlier due to the flow separation around the intake, reducing lift and increasing drag. In Figure 2.8b a streamline plot of an open parafoil profile from Fogell [30] is depicted, and it can be seen that the streamlines are following the geometry both on the top and bottom side of the aerofoil. Figure 2.8a on the other hand, shows the simulation results for an open profile. The flow separates at the bottom side of the parafoil due to the vortex forming at the intake. While the lift coefficient reduces by only 10%, the drag coefficient doubles for an open profile compared to a closed one.

For power generation in the AWE sector, a discrete FSI model with a flight control system for a figure of eight manoeuvres was introduced by Bosch [65]. The structural model was based on membrane and beam elements discretising a leading edge inflatable (LEI) kite. The steady RANS equations with the k-ω turbulence model were utilised to determine the section-wise aerodynamic loads. In order to avoid long computation time in each time step, the RANS equations were pre-computed for a given set of angles of attack, camber, and thickness to obtain the aerodynamic coefficients and section-wise load for their structural model. The model was able to reproduce the kite's bending and torsional deformation modes during their flight manoeuvres. The limiting factor in their model was the aerodynamic approximation, which only covered 2-dimensional flow and depended on pre-computed results. Their kite design was taken from Breukels [66] who published a design methodology for AWE LEI kites.

A three-dimensional FSI analysis, including the intake flow, was conducted by Fogell et al. [30, 67]. They investigated the fluid-structure interaction during steady glide with a loosely coupled approach. The fluid dynamics were solved with the commercial fluid solver STAR-CCM+ applying the RANS equations and $k-\epsilon$ turbulence model. Similar to the two-dimensional analysis mentioned previously, the domain inside the wing was meshed to study the flow and the structural response. Fogell analysed a single cell
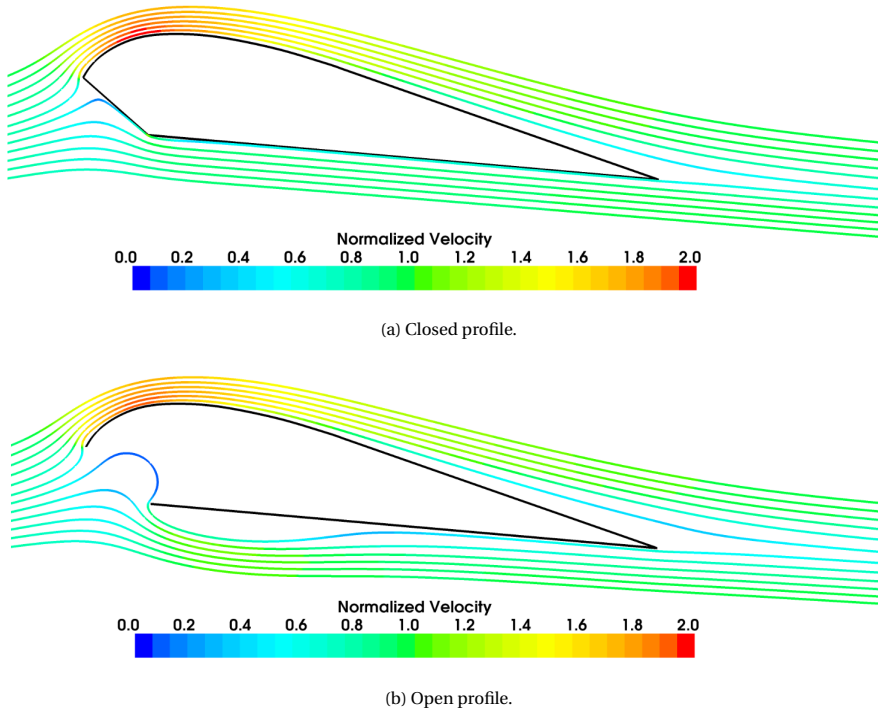
(a) Closed profile.

(b) Open profile.

Figure 2.8: Velocity streamline plots obtained by two-dimensional CFD analysis on closed and open parafoil profile [30].

with periodic boundary conditions to simplify the problem. The structural response was modelled with linear elastic isotropic material properties using LS-DYNA's commercial software. To correctly model the influence of slight compression in the membrane, the finite elements were enriched with a non-compressive model. In a more recent publication, Fogell performed a simulation study of a semi-rigid ram-air kite where the ribs were made of sheet metal and reported an error of 15% in lift coefficient and an underestimation of drag coefficient by 27% [68].

Another LS-DYNA analysis was performed by Perin et al. [69] on a ram-air parafoil with a strongly coupled FSI approach. The analysis approach is similar to the first studies done by Fogell, except that an entire kite is modelled. For validation of the numerical model, visual and load measurements were done in a wind tunnel test. The optical measurements were done with the digital image correlation technique to compare the shape of the actual and modelled kite. Load measurements were taken to determine lift and drag values depending on various angles of attack. The simulation showed resemblance with the visually measured shape, but the simulated glide ratio differed by 40% for larger angles of attack.

Paraglider dynamics was studied within a high-fidelity transient FSI simulation done by Lolies et al. [70] where they presented an Immersed Boundary coupling approach.

2

The flow is simulated using the Lattice Boltzmann method, and their structural model consists of an arrangement of structural springs, which allows using larger time steps during transient time integration. Their resulting paraglider shape agrees with the shape obtained in a wind tunnel experiment, but they reported an under-resolved boundary layer caused by the Immersed Boundary Method.

2.5.3. Round Parachute Simulation

Round parachutes follow a similar modelling approach as ram-air kites, and the application of round parachutes ranges from airdrops for personnel and equipment to spacecraft deceleration after the reentry phase in the atmosphere. The glide behaviour of round parachutes has been modelled to approximate the landing speed and aero-elastic effects due to the strong coupling between fluid and structure. Several publications from a US research group applied a finite element solver based on a space-time formulation to solve both fluid and structural domains. Their method was applied to simulate a descending T-10 parachute [71, 72], whilst improvements on the structural model via a dynamic contact algorithm for multiple parachute systems was done [73], and advances in mesh moving techniques based on the theory of elasticity were shown [74, 75].

Fan et al. applied a finite volume discretisation on the fluid domain with the Spalart–Allmaras turbulence model to describe the fluid-structure interaction of a round parachute from opening phase until steady glide [76]. A wrinkling model was used for the tensile structure, and their model shows agreement with experimental results and previous literature.

2.5.4. Sails

The sail dynamics of sailing boats and yachts is another FSI research field due to large occurring deformations of the thin sailcloth, and the analysis approach is similar to the ram-air and parachute FSI. The first publication found in literature about sail FSI was presented by Fukasawa et al. [77], where the sail structure was modelled with truss elements and an analytical expression gave the aerodynamic load. More recent publications by Renzsch utilised a RANS approach with membrane elements, including a non-compression model [78, 79]. Their simulations were validated using wind tunnel experiments and showed a good resemblance. Their finite element solver with wrinkling model was also based on the Dynamic Relaxation approach, which finds the force equilibrium for given pressure distribution and reported good numerical convergence behaviour and robustness.

Compared to most other publications, Trimarchi et al. [80] modelled the sail structure with shell elements which show the actual shape of wrinkles on the sail. An interpolation scheme included the occurring wrinkles on the sail in the fluid dynamics analysis, and a lower lift and increased drag were observed. As the wrinkles can only be modelled if the elements are smaller than the smallest wrinkle, this type of analysis requires a very dense mesh which causes a drastic increase in computation time.

2.5.5. Airbags

Several authors presented airbag simulations for the automotive sector [81, 82]. The challenges in a proper numerical airbag model are the high accelerations due to infla-

tion, contact modelling, compressibility effects of the pressurised air, folding, and material models. In some cases, an explicit time integration method is applied to simulate the airbag's transient behaviour in real-time and to measure its response to various initial conditions.

The inflation of a life jacket was studied by Garcia [83], where a multitude of dynamic relaxation methods was compared, such as kinetic and viscous damping and mass scaling. It was found that kinetic dynamic relaxation has the fastest convergence behaviour and the mass scaling dependent on the structure's stiffness effectively keeps the explicit time integration stable without falling below the critical time step.

2.6. EXPERIMENTS

To understand the structural and flight behaviour of ram-air kites, NASA and various research facilities in the US started with experimental setups in wind tunnels or drop-tests. Since wind tunnel experiments occur in a controlled environment, it serves much better for model validation of an FSI analysis compared to a drop-test. Full-scale wind tunnel tests were performed to measure the flight performance characteristics, such as glide ratio, lift and drag versus angle of attack, and dynamic flight behaviour. Lift and drag were determined by integrating the measured forces acting on the lines over the whole canopy. The resulting glide ratios obtained from studies such as done by Burk [84], Nicolaides [85], and Ware [86] for different parafoils vary between 2-6. In Ware's experimental setup, several ram-air wings with rectangular planform and open leading edge with several aspect ratios and chord lengths were compared, and their static and dynamic behaviour were studied. These studies show how tedious experimental wind tunnel tests for soft kites are. Measuring the angle of attack of an inflated wing is challenging because of the large deformations which occur during flight operation, e.g. the leading edge distortion. Also, the line drag has a direct influence on the measured results. In some cases, it constitutes approximately 50% of the drag and has to be corrected only to obtain flight characteristics of the parafoil.

Scaling effects were studied in Geiger et al. [87], where the flight characteristics were compared between a 300ft^2 and 1200ft^2 kite (approximately 28m^2 and 111.5m^2 respectively). The difference in testing configurations due to structural deformation was significant, and no general conclusion could be made about scaling effects. A general problem with small scale models of kites mainly originates from the nature of the flexible structure. The fluid properties, e.g. Reynolds number, can be changed in a wind tunnel through wind speed variations to account for the length difference between the two models. The problem arises from the ram pressure, which does not scale linearly but quadratically for the wind speed.

Other than measuring the line forces to determine the lift and drag coefficients, Askins [88] performed several wind tunnel tests on large aerodynamic decelerators, including the orbiter drag parachute and several large ram air kites. The pressure distribution was measured using a chord-wise strip with pressure sensors on the canopy. The pressure sensors were connected with tubes inside the structure, causing a restriction on the number of sensors attached due to additional weight and resulting wing stiffening. Experiments on wing scaling were performed by comparing the deformation of a 3×9 m^2 and 6×18 m^2 parafoil. Concluding remarks were that the smaller scale kite deformed

Figure 2.9: Ram-air kite in a wind tunnel experiment by de Wachter [23]. The white dots were used to compute the deformed shape of the parafoil for a CFD analysis. A striking detail are the dents located at the leading edge where the stagnation pressure compresses the membrane structure and the profile loses its curvature.

differently and reduced the glide ratio, also attributed to a slightly higher suspension line area used in the smaller model. A comparison between the intake size was also experimentally tested. It was found that smaller intakes improve the overall aerodynamic performance, a larger glide ratio of up to 25%. Simultaneously, no significant effect on the inflation characteristics was observed.

Finally, de Wachter [23] investigated the aerodynamics and structural deformations of a six square meters ram-air wing by the manufacturer FlySurfer in two wind tunnels. The deformations were measured using photogrammetry and laser scanning, see the white dots on the canopy for photogrammetry referencing in Figure 2.9, which provided a 3D point cloud of the kite's deformed surface. The kite was fixed at the leading edge with two metal rods, and the reaction force was measured at the risers to determine the aerodynamic forces. Also, thermography measurements were taken from the flow such that laminar and turbulent flow regions could be found. A range of wind speeds and angles of attack were tested, and a CFD analysis on the deformed 3D model was also performed comparing flow characteristics. The computed lift and drag from the CFD analysis showed a good fit compared to the measured forces.

2.6.1. Flight Testing of AWE Systems

The AWE community has published several publications on flight testing and aerodynamic parameter estimation. Hummel [89] developed a test plant to measure the aero-

dynamic performance of a tethered leading edge inflated wing in his PhD thesis. He used a car to tow the tethered wing and measured the kite's position using a camera setup and rotary encoder, the tether force using a load cell, and the relative flow velocity using a cup anemometer and wind data from a 20m mast in close proximity. The setup enabled to measure both C_R and glide ratio but due to the ground based test plant it is limited to small kite sizes. Also, the ground based wind sensor setup did not provide the V_a close to the kite.

Oehler et al. [13, 90] investigated a method to directly measure aerodynamic characterisation of a deformable LEI kite together with ground-based measured traction force by attaching a Pitot tube sensor with vanes below the canopy attached to the bridle system. They reported considerable variations in the aerodynamic coefficients during the power cycle, while the angle of attack of the kite varied only in a narrow range. This finding confirms the necessity of an aeroelastic model which can simulate the coupled fluid-structure interaction which captures the change in profile and planform due to deformations. Also, the steering capability of the LEI kite was quantified and they found that the yaw rate would drastically increase when the kite was in the high lift power setting i.e., a trim with a high angle of attack.

A different approach to finding the aerodynamic characteristics of a flexible tethered wing directly is based on parameter identification using the Extended Kalman Filter (EKF) technique, see e.g. [61, 91, 92]. Here, several sensors such as load cells, anemometers, and GPS are connected to the kite system and combined with a dynamic model of the kite the EKF is able to estimate states and parameters such as kite position, glide ratio and angle of attack, and wind speed at flight altitude. The model results are strongly dependent on the validity of the mathematical model and the sensor data quality. Based on the results found in literature, the approach is attractive even for live data acquisition but due to the nature of the EKF method, no theoretical convergence is guaranteed.

2.7. RESEARCH GOALS

Based on the literature review in this section about parafoil modelling, it can be concluded that many different models have been developed in the past to simulate ram-air wings and other thin-walled structures during flight. The structure was always modelled with thin membrane elements and a non-compression model that correctly determines each element's stress state, as could be seen in all publications mentioned above. While high fidelity models focus on resolving flow phenomenal using CFD, e.g. caused by the intake, low fidelity models incorporate the panel method to determine the pressure distribution acting on the canopy. Due to the inherently flexible nature of membrane structures, a fluid-structure interaction approach is crucial that correctly finds the inflatable structure's deformed state. Several coupling strategies were employed, ranging from loosely coupled fluid and structure domains without considering physical mass and damping, up to dynamic coupling to simulate the dynamic response and interaction of both fluid and structure. Wind tunnel experiments found in the literature imply that measuring the aerodynamic properties of a flexible wing is not a trivial task. Intricacies like supporting the wing and measuring forces without influencing the experiment are complicated. Also, defining the angle of attack on a flexible wing that rotates and deforms under load is not as simple as with a rigid wing. The motivation of this work posed

in the previous chapter is to find the aerodynamic and structural properties of a SkySails Power kite in a numerical model. Based on this motivation and the literature review, the following research goals were formulated:

1. **Develop an integrated aero-structural model to determine the aerodynamic characteristics such as C_R and glide ratio for a given tethered parafoil.**

2. **Analyse the structural design of a parafoil and identify shortcomings and important design aspects which may be crucial for airborne wind energy application.**

3. **Validate the developed model using measurements from SkySails Power obtained during flight.**

2.8. RESEARCH QUESTIONS

Based on the formulated research goals, the following research questions were formulated:

1. How do different FSI methods for determining a ram-air kite's shape with bridle line system under load compare with respect to computational robustness and efficiency?

2. Is a panel code based on the potential flow assumption sufficiently accurate in estimating the aerodynamic characteristics of a ram-air kite?

3. How can an engineering methodology be developed to design an efficient ram-air kite for AWE applications?

4. Is the current set of sensors in the operational airborne kite system sufficient for proper validation of integrated models?

3

COMPUTATIONAL STRUCTURAL DYNAMICS

This chapter introduces the theoretical background for the finite element solver that computes the kite's deformations under a given aerodynamic load. The derivation of nonlinear finite elements for membranes is shown, which includes kinematics and strain measures in a curvilinear coordinate frame and the final expression for internal and external force vectors using 2-node cable elements for the bridle lines and 3-node triangular elements for the membrane structure. The structural analysis of thin membranes poses mainly numerical challenges due to their inability to resist neither bending nor compression. To avoid refined meshing, the introduction of a wrinkling model adds another dimension of numerical noise. The choice of using flat 3-node shell elements rather than higher-order elements is to provide strong numerical stability at the cost of a less accurate stress field and possibly a stiffer structure, as described in Wriggers [93]. The implemented solver including two non-compression models for the membrane are verified on an inflatable airbag model. For further details on the derivation of the finite element method for membranes, refer to Wriggers [93], or Chapelle [94]. The tensor notation and algebra are extensively used during the derivation, as its notation is specifically handy in curvilinear coordinate systems. For an introduction to tensor algebra and the notation used in this work, refer to Appendix A.

Next to the spatial discretisation using the finite element method, the equations of motion are solved using the Kinetic Dynamic Relaxation (KRD) method, first introduced by Day [95]. It is an explicit time integration scheme that simulates the structure over a pseudo time scale and tracks the kinetic energy. When a peak in kinetic energy is detected, the solver sets all nodal velocities to zero and restarts with the current deformation field. The velocity reset usually occurs several times during the simulation and essentially damps the motion of most modes until a force equilibrium is found. The method has proven to be inherently stable for highly nonlinear problems and requires little pre-processing such as tuning damping parameters.
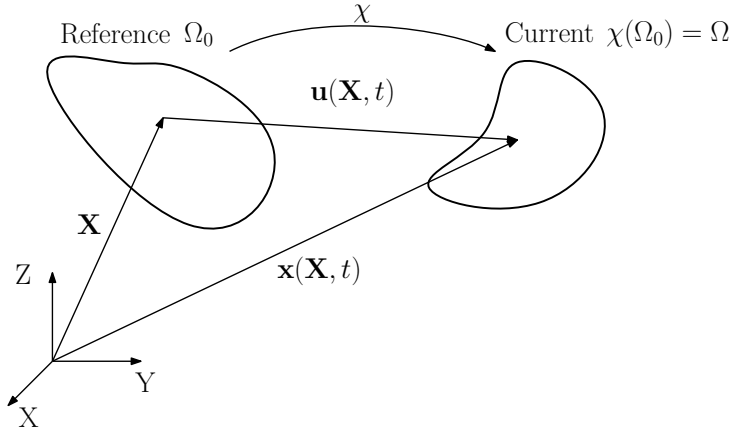
Figure 3.1: Motion of a deformed continuum Ω_0 in Lagrangian description.

3.1. MEMBRANE KINEMATICS

The kinematics of a deformable body can best be described with a reference and deformed configuration. Let Ω_0 be the domain of a continuum body which is filled with a material without voids or cracks placed in a Euclidean space $\mathbb{R}^3$. A position vector $\mathbf{X}$ as depicted in Figure 3.1 can be used to define all possible locations in Ω_0. Position vector $\mathbf{X}$ with a Cartesian basis and index $i = 1, 2, 3$ is then written as

$$\mathbf{X} = X^i \mathbf{E}_i. \tag{3.1}$$

Due to rigid body motion and elastic deformation, the body moves to its deformed or current configuration whose domain is given by Ω. A linear mapping function describes the motion χ, which maps the position vector $\mathbf{X}$ into the deformed body with

$$\chi(\mathbf{X}, t) = \mathbf{x}(\mathbf{X}, t) = \mathbf{X} + \mathbf{u}(\mathbf{X}, t). \tag{3.2}$$

The new position vector $\mathbf{x}$ is uniquely defined for the reference configuration and time t and can also be expressed as the vector summation of the reference position $\mathbf{X}$ and the relative displacement vector $\mathbf{u}(\mathbf{X}, t)$ between current and reference configuration. The description of all field variables concerning the reference configuration is called the Langrangian (material) description, whereas the description of the current configuration is the Eulerian (spatial) description. Both descriptions are equivalent, as they produce the same results, but the formulations of certain field variables are easier to express in either material or spatial description. The Eulerian description is primarily found in fluid dynamics because it enables a straightforward formulation of fluxes. On the other hand, the Lagrangian description is preferred when expressing mechanical stress and is used in this work. With this formulation, the velocity of a given point in the continuum is determined by the temporal derivative

$$\mathbf{v}(\mathbf{X}, t) = \frac{\partial}{\partial t}(\mathbf{X} + \mathbf{u}(\mathbf{X}, t)) = \dot{\mathbf{u}}, \tag{3.3}$$
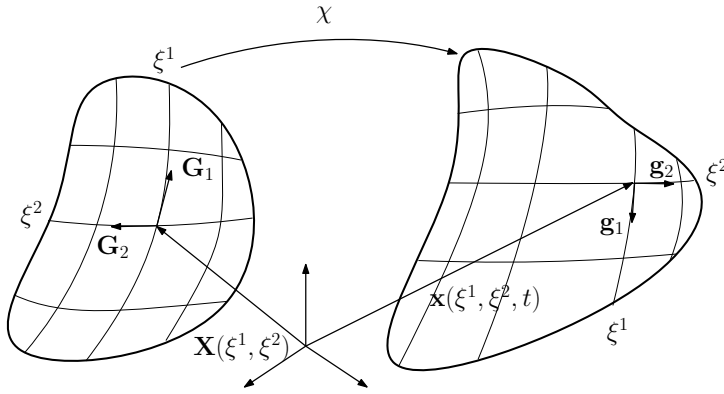
Figure 3.2: Reference and current configuration of membrane surface in curvilinear convected coordinates.

and similarly, the acceleration can be expressed as

$$\mathbf{a}(\mathbf{X}, t) = \frac{\partial}{\partial t}(\mathbf{X} + \mathbf{u}(\mathbf{X}, t)) = \ddot{\mathbf{u}}. \tag{3.4}$$

3.1.1. CONVECTED CURVILINEAR COORDINATES

A membrane structure can be approximated as a curved surface embedded in $\mathbb{R}^3$ with its position vector formulated in a curvilinear coordinate system with two coordinates (ξ^1, ξ^2). Curvilinear coordinates can be thought of as grid lines convected or embedded on the manifold, and they may be curved, and their basis vectors do not have to be orthonormal. Figure 3.2 depicts such a surface in both reference (undeformed) Ω_0 and current (deformed) configuration Ω, respectively. Its two coordinates and basis vectors uniquely define each point on the reference configuration. If the body deforms, the grid lines will follow, and both reference and deformed configuration of a position vector use the same coordinates, whereas the basis vectors differ. Equation 3.1 in curvilinear coordinates with co-variant basis vectors is then expressed as

$$\mathbf{X} = \xi^\alpha \mathbf{G}_\alpha, \tag{3.5}$$

where the index $\alpha = 1, 2$. Similarly, Equation 3.2 becomes

$$\mathbf{x} = \chi(\mathbf{X}(\xi^1, \xi^2), t) = \xi^\alpha \mathbf{g}_\alpha, \tag{3.6}$$

with $\mathbf{g}_\alpha$ being the basis vectors in the current configuration. The set of two tangent basis vectors on the membrane's surface is found by the partial derivative of the position vectors for the curvilinear coordinates in both initial and current configurations, respectively

$$\mathbf{G}_\alpha = \frac{\partial \mathbf{X}}{\partial \xi^\alpha} \tag{3.7a}$$

$$\mathbf{g}_\alpha = \frac{\partial \mathbf{x}}{\partial \xi^\alpha}. \tag{3.7b}$$

From there, the contra-variant basis vector can be determined with

$$\mathbf{G}^\alpha = G_{\alpha\beta} \cdot \mathbf{G}_\beta \tag{3.8a}$$

$$\mathbf{g}^\alpha = g_{\alpha\beta} \cdot \mathbf{g}_\beta, \tag{3.8b}$$

where the index β=1,2, and $G_{\alpha\beta}$ and $g_{\alpha\beta}$ are the respective metric tensors in the initial and current configuration. Also, the normal vector of both reference and the current configuration is important in later stage to formulate the pressure load, and they are determined by the cross-product of both tangent vectors normalised by their magnitude as

$$\mathbf{n}_0 = \frac{\mathbf{G}_1 \times \mathbf{G}_2}{||\mathbf{G}_1 \times \mathbf{G}_2||} = \frac{\mathbf{G}_3}{||\mathbf{G}_3||} \tag{3.9a}$$

$$\mathbf{n} = \frac{\mathbf{g}_1 \times \mathbf{g}_2}{||\mathbf{g}_1 \times \mathbf{g}_2||} = \frac{\mathbf{g}_3}{||\mathbf{g}_3||}. \tag{3.9b}$$

3.1.2. DEFORMATION GRADIENT

The tensor mapping between reference and the current configuration is the deformation gradient tensor **F**. It is a second-order tensor and maps a line element **dX** from the reference configuration into the current configuration. The resulting vector **dx** is then found by

$$d\mathbf{x} = \mathbf{F}d\mathbf{X}, \tag{3.10}$$

The line element in the reference configuration is determined by

$$d\mathbf{X} = \frac{\partial \mathbf{X}}{\partial \xi^\alpha} d\xi^\alpha = \mathbf{G}_\alpha d\xi^\alpha, \tag{3.11}$$

and the line element in the current configuration is given by

$$d\mathbf{x} = \frac{\partial \mathbf{x}}{\partial \xi^\alpha} d\xi^\alpha = \mathbf{g}_\alpha d\xi^\alpha. \tag{3.12}$$

In order to find the expression for the deformation gradient, recall that any second-order tensor can be formulated as the tensor product of two vectors, as stated in Equation A.9

$$\mathbf{F} = \mathbf{a} \otimes \mathbf{b}, \tag{3.13}$$

here given as arbitrary vectors **a** and **b**. Substituting Equation 3.13 into 3.10 results in

$$dx = (a \otimes b)dX = a(b \cdot dX). \tag{3.14}$$

To satisfy the left hand side, a and b become

$$b = G^\alpha \tag{3.15a}$$

$$a = g_\alpha, \tag{3.15b}$$

and this results in a compact expression for the deformation gradient tensor in curvilinear coordinates

$$F = g_\alpha \otimes G^\alpha. \tag{3.16}$$

3.1.3. GREEN-LAGRANGIAN STRAIN

Strain measures relative deformation inside a body given by normal and shear components. Several strain formulations exist, but the nonlinear Green-Lagrangian strain tensor is used in this work, which fully describes relative deformation without being influenced by rigid-body motion. The strain expression can be derived by changing the length and orientation of a differential line element. The relative deformation of an arbitrary differential line element can be described by the difference in lengths of current and reference configuration. The differential lengths are

$$dS = \sqrt{dX \cdot dX} \tag{3.17a}$$

$$ds = \sqrt{dx \cdot dx}, \tag{3.17b}$$

and the squared difference is defined as

$$(ds)^2 - (dS)^2 = dx \cdot dx - dX \cdot dX = dX(F^T F - I)dX, \tag{3.18}$$

where F^T is the transpose of the deformation gradient tensor, and I the identity tensor. The identity tensor in curvilinear coordinates can be expressed as

$$F^{-1}F = (G_\alpha \otimes g^\alpha)(g_\beta \otimes G^\beta) \tag{3.19a}$$

$$= \delta_\beta^\alpha G_\alpha \otimes G^\beta \tag{3.19b}$$

$$= G_{\alpha\beta} G^\alpha \otimes G^\beta, \tag{3.19c}$$

where Equation 3.8 was used to change the basis from the co- to contra-variant. Substituting Equation 3.19c into Equation 3.18 and writing the deformation gradient tensor in curvilinear coordinates results in

$$(ds)^2 - (dS)^2 = dX(G^\alpha \otimes g_\alpha \cdot g_\beta \otimes G^\beta - G_{\alpha\beta} G^\alpha \otimes G^\beta)dX \tag{3.20a}$$

$$= dX(g_{\alpha\beta} G^\alpha \otimes G^\beta - G_{\alpha\beta} G^\alpha \otimes G^\beta)dX \tag{3.20b}$$

$$= dX2EdX, \tag{3.20c}$$

where $\mathbf{E}$ is the Green-Lagrangian strain tensor, defined as twice the difference of the squared lengths. The final expression of the Green-Lagrangian strain tensor is

$$\mathbf{E} = E_{\alpha\beta}\mathbf{G}^{\alpha} \otimes \mathbf{G}^{\beta}, \tag{3.21}$$

with its components

$$E_{\alpha\beta} = \frac{1}{2}(g_{\alpha\beta} - G_{\alpha\beta}). \tag{3.22}$$

It can be seen that the components of $E_{\alpha\beta}$ are dependent on the symmetric metric tensors, which means that the strain tensor is symmetric as well. Introducing the Voigt notation applicable to symmetric tensors $E_{\alpha\beta}$ can be written in vector form such that

$$E_{\alpha\beta} = \begin{bmatrix} E_{11} & E_{12} \\ E_{21} & E_{22} \end{bmatrix} \quad \Rightarrow \mathbf{E}^{\text{Voigt}} = \begin{bmatrix} E_{11} \\ E_{22} \\ 2E_{12} \end{bmatrix} = \begin{bmatrix} E_{11} \\ E_{22} \\ \gamma_{12} \end{bmatrix}, \tag{3.23}$$

where γ_{12} is the shear strain. Similar to strain, the stress in a continuum is a second-order tensor. Depending on which reference area and force is used to describe stress, the tensor varies accordingly. Both Cauchy and Piola-Kirchhoff stress measures are introduced in Appendix B including how to transform between each one of them. Also, the constitutive model, which resembles the material properties in a continuum element for both isotropic and orthotropic linear elastic materials, can be found in Appendix C.

3.2. Principal of Virtual Work by Galerkin Method

The Total Lagrangian formulation of the Cauchy Momentum equation derived in Appendix D is referred to as the strong form. Whereas the strong form requirement is generally difficult to enforce on arbitrary domains, the formulation can be weakened using the Galerkin method. The weak formulation is more approachable and solved using the finite element method, while the strong formulation can be solved using finite difference [96]. The procedure of transforming a set of differential equations into its weak formulation using the Galerkin method is done by taking the product of the governing equation with a kinetically admissible test field $\delta\mathbf{u}$, also known as virtual displacement or variation, and then integrating over the domain Ω_0. Kinetically admissible means that the test field satisfies the Dirichlet boundary conditions of prescribed displacements, i.e. $\delta\mathbf{u} = 0$ on Γ_{u_0}. Following this procedure, one obtains

$$\int_{\Omega_0} \delta\mathbf{u}^T \left(\nabla_0 \cdot \mathbf{P} + \rho_0\mathbf{b} - \rho_0\ddot{\mathbf{u}}\right) dV = 0. \tag{3.24}$$

The integral can be further simplified using Green's Theorem, which is a particular expression of integration by parts and written as

$$\int_{\Omega_0} \delta\mathbf{u}^T \nabla_0 \cdot \mathbf{P} dV = -\int_{\Omega_0} \nabla_0 \cdot \delta\mathbf{u}^T \mathbf{P} dV + \int_{\Gamma_0} \delta\mathbf{u}^T \mathbf{P}\mathbf{n}_0 dS, \tag{3.25}$$

with Γ_0 referring to the union of traction and prescribed displacement boundaries. Substituting Equation 3.25 into Equation 3.24 results in

$$\int_{\Omega_0} \rho_0 \delta\mathbf{u}^T \ddot{\mathbf{u}} dV + \int_{\Omega_0} \delta\mathbf{F}^T : \mathbf{P} dV = \int_{\Omega_0} \rho_0 \delta\mathbf{u}^T \mathbf{b} dV + \int_{\Gamma_0} \delta\mathbf{u}^T \mathbf{Pn}_0 dS, \tag{3.26}$$

where the divergence of the test field is expressed as the variation of the deformation gradient tensor. Next, the surface integral can be split into two domains where Dirichlet and Neumann boundary conditions are active such that

$$\int_{\Gamma_0} \delta\mathbf{u}^T \mathbf{Pn}_0 dS = \underbrace{\int_{\Gamma_{u_0}} \delta\mathbf{u}^T \mathbf{t}_0 dS}_{0} + \int_{\Gamma_{t_0}} \delta\mathbf{u}^T \mathbf{t}_0 dS, \tag{3.27}$$

with the first integral being zero due to the kinetic admissibility of the test field $\delta\mathbf{u}$. Using Equation 3.27, Equation 3.26 can be written as

$$\int_{\Omega_0} \rho_0 \delta\mathbf{u}^T \ddot{\mathbf{u}} dV + \int_{\Omega_0} \delta\mathbf{E} : \mathbf{S} dV = \int_{\Omega_0} \rho_0 \delta\mathbf{u}^T \mathbf{b} dV + \int_{\Gamma_0} \delta\mathbf{u}^T \mathbf{t}_0 dS, \tag{3.28}$$

where the second Piola-Kirchhoff stress tensor was substituted using Equation B.3, and the variation of $\mathbf{E}$ was determined by decomposing the deformation gradient into its symmetric and skew-symmetric part, see Wriggers p. 85 [93]. The expression in Equation 3.28 is called the virtual work principle and can be divided into virtual work components with

$$\delta W_{\text{kin}} + \delta W_{\text{int}} = \delta W_{\text{ext}}, \tag{3.29}$$

with δW_{kin} being the virtual kinetic work, δW_{int} the virtual internal work due to elastic strain, and δW_{ext} the virtual external work due to body forces and surface traction.

3.2.1. DEFORMATION DEPENDENT LOAD
Deformation dependent load like the pressure is expressed in the current configuration with the area and its normal vector changing with deformation. The virtual work due to pressure load in the current configuration is defined as

$$\delta W_{\text{ext, p}} = \int_{\Gamma_t} \delta\mathbf{u}^T p\mathbf{n} dS, \tag{3.30}$$

where p is the pressure and $\mathbf{n}$ is the normal vector in the current configuration. Since the Total Lagrangian formulation is based on the reference configuration, Equation 3.30 is transformed using Nanson's relation, which describes the change in area and normal vector from reference to the current configuration as

$$\int_{\Gamma_t} \mathbf{n} dS = \int_{\Gamma_{t_0}} \det(\mathbf{F})\mathbf{n_0}\mathbf{F}^{-T} dS. \tag{3.31}$$

Substituting 3.31 into Equation 3.30 results in

$$\delta W_{\text{ext, p}} = \int_{\Gamma_{t_0}} p\det(\mathbf{F})\delta\mathbf{u}^T \mathbf{F}^{-T}\mathbf{n_0} dS. \tag{3.32}$$

3.3. FINITE ELEMENT METHOD

So far, the equations of motion were derived in integral (weak) form. The derived formulation can be solved analytically for only a limited number of geometries and boundary conditions. In order to solve the formulation for arbitrary shapes and boundary conditions, the finite element method is utilised. This solution method is based on splitting the domain into many geometric elements like triangles or quadrilaterals. The field variables such as position, displacement or strain are approximated within each element with continuous interpolation functions, also called shape functions. A wide range of shape functions can be used to express field variables inside a finite element. The most common approach is the Lagrangian interpolation polynomial which takes field variables known at given locations inside the element, called nodes, and provides a continuous expression of the field between the nodes. The Lagrangian interpolation polynomial for a field $\varphi(\xi^\alpha)$ is approximated as

$$\varphi(\xi^\alpha) \approx \hat{\varphi}(\xi^\alpha) = \sum_{i=1}^{M} N_i(\xi^\alpha)\varphi_i, \tag{3.33}$$

where $\hat{\varphi}(\xi^\alpha)$ is the field variable approximation, φ_i the field variable at node level, M the number of nodes used in the finite element, and $N_i(\xi^\alpha)$ the shape function written as the Lagrangian polynomial

$$N_i(\xi^\alpha) = \prod_{j=1, j\neq i}^{D} \frac{\xi^\alpha - \xi_j}{\xi_i - \xi_j}, \tag{3.34}$$

with index i and j indicate node numbers in a finite element, and D is the degree of the interpolation function. The shape function N_i takes the value one at node i and zero at all other nodes. Between the nodes, N_i is interpolated and takes a value between zero and one, based on the degree of interpolation. Applying the Lagrangian polynomial approximation to position vectors in both configurations and deformation results in

$$\mathbf{X}(\xi^\alpha) = \sum_{i=1}^{M} N_i(\xi^\alpha)\mathbf{X}_i \tag{3.35a}$$

$$\mathbf{x}(\xi^\alpha, t) = \sum_{i=1}^{M} N_i(\xi^\alpha)\mathbf{x}_i(t) \tag{3.35b}$$

$$\mathbf{u}(\xi^\alpha, t) = \sum_{i=1}^{M} N_i(\xi^\alpha)\mathbf{u}_i(t), \tag{3.35c}$$

and with the position vector, the co-variant base vectors in reference and the current configuration can be written as

$$\mathbf{G}_\alpha = \frac{\partial \mathbf{X}}{\partial \xi^\alpha} = N_{i,\alpha}\mathbf{X}_i \tag{3.36a}$$

$$\mathbf{g}_\alpha = \frac{\partial \mathbf{x}}{\partial \xi^\alpha} = N_{i,\alpha}\mathbf{x}_i. \tag{3.36b}$$

Splitting the domain Ω_0 into several finite elements, the virtual work principle can be approximated as an assembly of elements where the shape functions provide continuity between nodes such that

$$\delta W_{\text{kin}} \approx \bigcup_{e=1}^{N_e} \int_{\Omega_{0_e}} \delta \mathbf{u}^T \ddot{\mathbf{u}} \rho_0 dV \tag{3.37a}$$

$$\delta W_{\text{int}} \approx \bigcup_{e=1}^{N_e} \int_{\Omega_{0_e}} \delta \mathbf{E} : \mathbf{S} dV \tag{3.37b}$$

$$\delta W_{\text{ext}} \approx \bigcup_{e=1}^{N_e} \int_{\Omega_{0_e}} \delta \mathbf{u}^T \mathbf{b} \rho_0 dV + \bigcup_{s=1}^{N_s} \int_{\Gamma_s} \delta \mathbf{u}^T \mathbf{t}_0 dS. \tag{3.37c}$$

where $\bigcup$ is the assembly operator which adds each element's contribution to a global scalar (or vector in case of element forces). Also, N_e is the number of elements and N_s the number of surface edges in Ω_0. The expression for each virtual work contribution on the element level can be found using the shape functions. The virtual kinetic work in a single finite element using Equation 3.35a is then written as

$$\delta W_{\text{kin},e} = \delta \mathbf{u}_i^T \int_{\Omega_{0_e}} \rho_0 N_i(\xi^\alpha) N_j(\xi^\alpha) dV \ddot{\mathbf{u}}_j \tag{3.38a}$$

$$= \{\delta \mathbf{u}\}_e^T [\mathbf{M}]_e \{\ddot{\mathbf{u}}\}_e, \tag{3.38b}$$

both nodal virtual displacement and acceleration vectors indicated by curly brackets can be taken out of the integral because they are nodal properties. The integral is written in matrix form indicated by square brackets and is called the local mass matrix $\mathbf{M}_e$. Similarly the virtual external work for a single element due to body forces can be found

$$\delta W_{\text{body},e} = \delta \mathbf{u}_i^T \int_{\Omega_{0_e}} \rho_0 N_i(\xi^\alpha) \mathbf{b} dV \tag{3.39a}$$

$$= \{\delta \mathbf{u}\}_e^T \{\mathbf{f}_{\text{body}}\}_e. \tag{3.39b}$$

For the virtual internal work, first the variation of the strain tensor $\delta \mathbf{E}$ in terms of shape functions is derived as

$$\delta E_{\alpha\beta} = \frac{1}{2}\delta(g_{\alpha\beta} - G_{\alpha\beta}) \tag{3.40a}$$
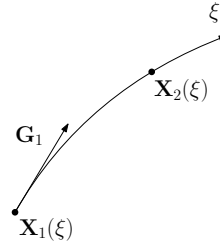
$$= \frac{1}{2}\delta g_{\alpha\beta} \tag{3.40b}$$

$$= \frac{1}{2}(\delta \mathbf{g}_\alpha \mathbf{g}_\beta + \mathbf{g}_\alpha \delta \mathbf{g}_\beta) \tag{3.40c}$$

$$= \delta \mathbf{u}_i \frac{1}{2}(N_{i,\alpha} N_{j,\beta} + N_{j,\alpha} N_{i,\beta})\mathbf{x}_j \tag{3.40d}$$

$$= \{\delta \mathbf{u}\}_e [\mathbf{B}]_e^T, \tag{3.40e}$$
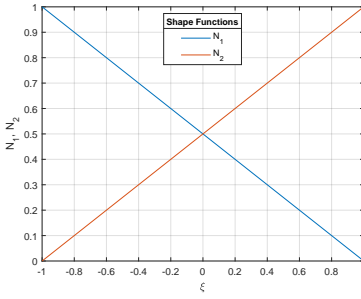
(a) Linear shape functions N_1 and N_2 in natural coordinates for cable element.

(b) Cable discretised using two nodes in curvilinear coordinate system.

Figure 3.3: Truss element with linear shape functions.

where $[\mathbf{B}]_e$ is the strain-displacement matrix which contains the shape function derivatives. Substituting Equations 3.40 and into 3.37b results in the virtual internal work formulation

$$\delta W_{\text{int},e} = \int_{\Omega_{0e}} \{\delta \mathbf{u}\}_e^T [\mathbf{B}]_e^T \{\mathbf{S}\}_e \, dV. \tag{3.41}$$

The equations of motion expressed as a global system of equations can be assembled by adding the element contributions of each type of virtual work such that

$$\delta W = \bigcup_{e=1}^{N_e} \bigcup_{s=1}^{N_s} \delta \mathbf{u}_{e,s}^T (\mathbf{f}_{\text{kin}} + \mathbf{f}_{\text{int}} - \mathbf{f}_{\text{ext}})_{e,s} = 0. \tag{3.42}$$

A non-trivial solution of Equation 3.42 corresponds to the equations of motion expressed as a force balance

$$[\mathbf{M}]\{\ddot{\mathbf{u}}\} + \{\mathbf{F}_{\text{int}}\} - \{\mathbf{F}_{\text{ext}}\} = \{\mathbf{0}\}, \tag{3.43}$$

which can be integrated in time to find its dynamic response, or in the case of a static approach where the acceleration term is negligible, the deformations can be found with a root-finding algorithm. Next, the shape functions of both bridle line and membrane elements are derived, which are used to model the kite.

3.3.1. C2 - 2-NODE CABLE ELEMENT
A 2-node truss element used to describe bridles lines can be written with two shape functions in natural coordinates as

$$N_1 = \frac{1}{2}(1 - \xi) \tag{3.44a}$$

$$N_2 = \frac{1}{2}(1 + \xi) \tag{3.44b}$$

where ξ is the coordinate ranging from -1 to 1 and uniquely defines the position vector and base vector as depicted in Figure 3.3b. Both linear shape functions are plotted for all

ξ in Figure 3.3a, and it can be seen that the field is linearly interpolated between the two nodes. The element mass matrix from Equation 3.38a using the shape functions is

$$[\mathbf{M}]_e = \frac{1}{2}\rho_0 A_0 L_0 [\mathbf{I}],$$ (3.45)

with the bridle line cross-section area given by A_0 and initial element length by L_0. It should be noted that this is a lumped mass matrix where all off-diagonal terms are zero, and this format allows for a cheap inversion. Next, the external body and traction forces due to gravity and distributed edge loads can be expressed as

$$\{\mathbf{f}_{\text{ext}}\}_e = \{\mathbf{f}_{\text{body}}\}_e + \{\mathbf{f}_t\}_e$$ (3.46a)

$$= \frac{1}{2}\rho_0 A_0 L_0 [\mathbf{g}^T \quad \mathbf{g}^T]^T + \frac{q d_0}{2}[\mathbf{L}^T \quad \mathbf{L}^T]^T,$$ (3.46b)

with the gravitational acceleration vector written as $\mathbf{g}$, edge load q, bridle diameter d_0, and the projected length vector $\mathbf{L}$. Finally, the internal force vector from Equation 3.40 is written as

$$\mathbf{f}_{\text{int}} = A_0 L_0 \{\mathbf{B}\}^T S$$ (3.47)

where S is the scalar Second Piola-Kirchhoff stress, and the strain-displacement vector $\mathbf{B}$ is

$$\{\mathbf{B}\} = \frac{1}{L_0^2}[(\mathbf{x}_1 - \mathbf{x}_2)^T \quad (\mathbf{x}_2 - \mathbf{x}_1)^T].$$ (3.48)

The following element modification can be applied to the cable when it is in compression to account for the slack state,

$$S = \begin{cases} 0 & \text{if} \quad E_G \leq 0 \\ E \cdot E_G = E\frac{L^2 - L_0^2}{2L_0^2} & \text{if} \quad E_G > 0, \end{cases}$$ (3.49)

which summarises the finite element formulation of force vectors for the bridle lines.

3.3.2. T3 - 3-NODE TRIANGULAR MEMBRANE ELEMENT
Similar to the truss element, the 3-node membrane element has linear shape functions as depicted in Figure 3.4b which are written in natural coordinates (shown in Figure 3.4a) as

$$N_1 = 1 - r - s$$ (3.50a)

$$N_2 = r$$ (3.50b)

$$N_3 = s,$$ (3.50c)

where the natural coordinates (r, s) are simply the normalised edge lengths given by $\mathbf{x}_2$-$\mathbf{x}_1$ and $\mathbf{x}_3$-$\mathbf{x}_1$ respectively. The lumped element mass matrix is then written as
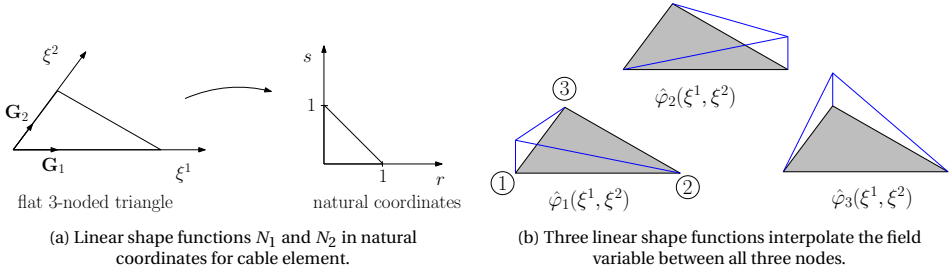
(a) Linear shape functions N_1 and N_2 in natural coordinates for cable element.

(b) Three linear shape functions interpolate the field variable between all three nodes.

Figure 3.4: Truss element with linear shape functions.

$$[\mathbf{M}]_e = \frac{1}{3}\rho_0 A_0 h [\mathbf{I}], \tag{3.51}$$

with the initial triangle's surface area given by A_0 and the element's thickness by h. The external body forces due to gravity are expressed similar to the truss element as

$$\{\mathbf{f}_{\text{body}}\}_e = \frac{1}{3}\rho_0 A_0 h [\mathbf{g}^T \quad \mathbf{g}^T]^T. \tag{3.52}$$

The pressure load as derived in Section 3.2.1 acts normal to the surface in the current configuration and can be transformed to the initial configuration. To avoid this operation, the pressure load acting on each node is instead expressed in the current configuration

$$\{\mathbf{f}_{\text{p}}\}_e = \frac{1}{3} A p [\mathbf{n}^T \mathbf{n}^T \mathbf{n}^T]^T, \tag{3.53}$$

with the element's area in the current configuration written as

$$A = \frac{1}{2}||\mathbf{g}_1 \times \mathbf{g}_2|| = \frac{1}{2}||(\mathbf{x}_2 - \mathbf{x}_1) \times (\mathbf{x}_3 - \mathbf{x}_1)||. \tag{3.54}$$

Similarly, the normal vector in the current configuration can be written as

$$\mathbf{n} = \frac{\mathbf{g}_1 \times \mathbf{g}_2}{||\mathbf{g}_1 \times \mathbf{g}_2||} = \frac{(\mathbf{x}_2 - \mathbf{x}_1) \times (\mathbf{x}_3 - \mathbf{x}_1)}{||(\mathbf{x}_2 - \mathbf{x}_1) \times (\mathbf{x}_3 - \mathbf{x}_1)||}. \tag{3.55}$$

Substituting both area and normal vector expression into Equation 3.54 results in the external force vector due to pressure load, here only written for an individual node i

$$\{\mathbf{f}_{\text{p}}\}_i = \frac{1}{6}(\mathbf{x}_2 - \mathbf{x}_1) \times (\mathbf{x}_3 - \mathbf{x}_1). \tag{3.56}$$

Finally, the internal force vector in Equation 3.40 using linear shape functions are expressed as

$$\{\mathbf{f}_{\text{int}}\}_e = A_0 h [\mathbf{B}]^T [\mathbf{T}_\sigma] \{\mathbf{S}_{\text{fibre}}\}, \tag{3.57}$$

where $[\mathbf{T}_\sigma]$ is the rotation matrix that transforms the stress components in Voigt notation from the local fibre orientation to the element's local coordinates. This rotation matrix can be disregarded in the case of isotropic material. Its components are

$$[\mathbf{T}_\sigma] = \begin{bmatrix} \cos^2\theta & \sin^2\theta & -2\sin\theta\cos\theta \\ \sin^2\theta & \cos^2\theta & 2\sin\theta\cos\theta \\ \sin\theta\cos\theta & -\sin\theta\cos\theta & \cos^2\theta - \sin^2\theta \end{bmatrix}. \tag{3.58}$$

Next, the strain-displacement matrix in Cartesian coordinates is derived using the Jacobian transformation given in Section A.0.3. The local Cartesian coordinate system is defined such that the triangle edge connecting the first two nodes acts as the x-axis, and the y-axis lies normal to the plane spanned by the x-axis and the element's normal vector. The Jacobian in matrix form is then written as

$$[\mathbf{J}] = \begin{bmatrix} ||\mathbf{X_{21}}|| & (\mathbf{X_{21}} \cdot \mathbf{X_{31}})/(||\mathbf{X_{21}}||) \\ 0 & (||\mathbf{X_{21}} x \mathbf{X_{31}}||)/(||\mathbf{X_{21}}||) \end{bmatrix} = \begin{bmatrix} J_{11} & J_{12} \\ 0 & J_{22} \end{bmatrix}, \tag{3.59}$$

where the notation $\mathbf{X_{21}} = \mathbf{X_2} - \mathbf{X_1}$ is used. The inverse of $\mathbf{J}$ is then written as

$$[\mathbf{J}]^{-1} = \begin{bmatrix} 1/J_{11} & -J_{12}/(J_{11}J_{22}) \\ 0 & 1/J_{22} \end{bmatrix} = \begin{bmatrix} T_{11} & T_{12} \\ 0 & T_{22} \end{bmatrix}. \tag{3.60}$$

With the inverse Jacobian the element Green-Lagrangian strain tensor in Cartesian coordinates is expressed as

$$\{\mathbf{E}_{\text{Cart}}\}_e = [\mathbf{Q}]\{\mathbf{E}_{\text{Curv}}\}_e, \tag{3.61}$$

where matrix $[\mathbf{Q}]$ is the Jacobian matrix for the strain tensor using Voigt notation defined as

$$[\mathbf{Q}] = \begin{bmatrix} T_{11}^2 & 0 & 0 \\ T_{12}^2 & T_{22}^2 & T_{12}T_{22} \\ 2T_{11}T_{12} & 0 & T_{11}T_{22} \end{bmatrix}. \tag{3.62}$$

Finally, the Green-Lagrangian strain tensor components are written in Cartesian coordinates

$$E_{xx} = \frac{1}{2}(\frac{g_{11}}{J_{11}^2} - 1) \tag{3.63a}$$

$$E_{yy} = \frac{g_{22}J_{11}^2 - 2g_{12}J_{11}J_{12} + g_{11}J_{12}^2}{2J_{11}^2 J_{22}^2} - \frac{1}{2} \tag{3.63b}$$

$$E_{xy} = \frac{J_{11}g_{12} - J_{12}g_{11}}{J_{11}^2 J_{22}} \tag{3.63c}$$

Similarly, the strain-displacement matrix in Cartesian coordinates is given by

$$[\mathbf{B}] = [\mathbf{Q}][\mathbf{B}_{\text{Curv}}], \tag{3.64}$$

where the strain-displacement matrix in curvilinear coordinates is

$$[\mathbf{B}_{\text{Curv}}] = \begin{bmatrix} -(\mathbf{x_2}-\mathbf{x_1})^T & (\mathbf{x_2}-\mathbf{x_1})^T & \mathbf{0} \\ -(\mathbf{x_3}-\mathbf{x_1})^T & \mathbf{0} & (\mathbf{x_3}-\mathbf{x_1})^T \\ (\mathbf{x_3}-\mathbf{x_2}+2\mathbf{x_1})^T & (\mathbf{x_3}-\mathbf{x_1})^T & (\mathbf{x_2}-\mathbf{x_1})^T \end{bmatrix}. \tag{3.65}$$

A global system of equations can be assembled and solved with the mass matrix, internal and external force vector expressions.

3.3.3. Wrinkling Model

The previously derived membrane elements cannot correctly determine the actual stress state as soon as compression occurs and effectively overestimate the structure's stiffness. Therefore, a wrinkling model is introduced that corrects the stress state of each element in case of compression. This correction can be done by either manipulating the deformation gradient or the constitutive tensor. The latter correction method is preferred with orthotropic material, and two methods found in the literature are implemented and compared.

The first method by Jarasjarungkiat et al. [50] is based on a penalisation and manipulation method of the constitutive tensor. Using the mixed wrinkling criterion, which takes compression due to the Poisson's effect into account and is shown in Table 3.1, the membrane state is first found on the element level. If wrinkling occurs, the wrinkling direction has to be found, and the constitutive tensor is rotated accordingly such that the compressive stress state vanishes. The wrinkling direction can be determined with the *Newton's method* where the gradient is analytically available, leading to a quick solution. When the constitutive tensor is rotated for the wrinkling direction, it becomes singular, and therefore a penalty factor is introduced, which is scaled with a maximum allowable compressive stress the user has to define.

The second method by Raible et al. [51] also applies the mixed wrinkling criterion to differentiate between the three stress states. The stress state is first determined on a local element basis, and a wrinkling strain is introduced, which becomes active in case of a wrinkled or slack state. It effectively reduces compressive stress and is updated every iteration if active. In order to find the components of the wrinkling strain, the *Newton's method* is applied as well.

The disadvantage of both methods is the absence of continuity concerning the deformation vector, which may cause numerical instabilities for a static solution method.

Table 3.1: Mixed wrinkling criterion.

Membrane state	Taut	Wrinkled	Slack
Stress and strain	$S_2 > 0$	$S_2 \leq 0$ and $E_1 > 0$	$E_1 \leq 0$

3.4. Dynamic Relaxation

With a dynamic formulation of the equation of motion derived in the previous section, the next step is to find a suitable solution method that is numerically robust and efficient. For this purpose, one must decide whether a static or dynamic solution method is favoured. Mathematically, both approaches should obtain the same result, i.e. a steady-state of the inflated structure with all external and internal forces in equilibrium. A static

solution method for nonlinear problems such as *Newton's method* solves a system of linear equations by inverting the stiffness matrix and reiterating until the residual forces are sufficiently small. The static approach was applied to the airbag inflation problem (Section 3.5.1), and no stable solution could be found with none of the wrinkling models, and instead, a dynamic solution method based on Kinetic Dynamic Relaxation (KDR) [45] is used. KDR is based on an explicit time integration with constant time step and variable mass, which is scaled such that the time integration is strictly stable. During the time stepping, kinetic energy is tracked, and as soon as an energy peak is detected, the nodal velocities are reset to zero. This process is repeated until the force residual or kinetic energy is sufficiently decayed, reaching a static solution.

3.4.1. EXPLICIT TIME INTEGRATION

Kinetic dynamic relaxation is based on the second-order *leap frog* explicit time integration method, which computes the position and velocity components staggered in half time steps. The equation of motion at time step n is written as

$$\mathbf{M}\ddot{\mathbf{u}}^n = \mathbf{f}_{\text{ext}}(\mathbf{u}^n) - \mathbf{f}_{\text{int}}(\mathbf{u}^n) = \mathbf{R}(\mathbf{u}^n). \tag{3.66}$$

Using the first-order expression for temporal derivatives from finite-difference for acceleration, and velocity leads to

$$\ddot{\mathbf{u}}^n \approx \frac{\dot{\mathbf{u}}^{n+\frac{1}{2}} - \dot{\mathbf{u}}^{n-\frac{1}{2}}}{\Delta t} \tag{3.67}$$

$$\dot{\mathbf{u}}^{n+\frac{1}{2}} \approx \frac{\dot{\mathbf{u}}^n - \dot{\mathbf{u}}^{n-1}}{\Delta t}, \tag{3.68}$$

from which the displacement at the next time step $n + 1$ can be found with

$$\mathbf{u}^{n+1} = \mathbf{u}^n + \Delta t \dot{\mathbf{u}}^{n+\frac{1}{2}}. \tag{3.69}$$

Similar for the velocity at the next half-time step substituting Equation 3.67 into Equation 3.66 and solving for $\dot{\mathbf{u}}^{n+\frac{1}{2}}$ results in

$$\dot{\mathbf{u}}^{n+\frac{1}{2}} = \dot{\mathbf{u}}^{n-\frac{1}{2}} + \Delta t \mathbf{M}^{-1} \mathbf{R}(\mathbf{u}^n). \tag{3.70}$$

Both Equation 3.69 and 3.70 determine the velocity and displacement of every structural degree of freedom for the next time step $n + \frac{1}{2}$ and $n + 1$, respectively. The kinetic energy of the structure is found using

$$W_{\text{kin}}^{n+\frac{1}{2}} = \left(\dot{\mathbf{u}}^{n+\frac{1}{2}} \right)^T \mathbf{M}\dot{\mathbf{u}}^{n+\frac{1}{2}}. \tag{3.71}$$

An energy peak is detected if the previous time step's kinetic energy is larger than at the current time step. In order to obtain a more accurate estimate of the deformation field during the peak, a quadratic interpolation between the two previous and the current time step is applied, which results in an updated deformation vector

$$\mathbf{u}^* = -(1 + q)\dot{\mathbf{u}}^{n-\frac{1}{2}} + \frac{q\Delta t}{2} \mathbf{M}^{-1} \mathbf{R}(\mathbf{u}^n), \tag{3.72}$$

where the factor q is

$$q = \frac{W_{\text{kin}}^{n-\frac{1}{2}} - W_{\text{kin}}^{n+\frac{1}{2}}}{2W_{\text{kin}}^{n-\frac{1}{2}} - W_{\text{kin}}^{n-\frac{3}{2}} - W_{\text{kin}}^{n+\frac{1}{2}}}. \tag{3.73}$$

After the kinetic energy peak the routine is restarted using

$$\dot{\mathbf{u}}^{n+\frac{1}{2}} = \frac{\Delta t}{2}\mathbf{M}^{-1}\mathbf{R}(\mathbf{u}^n), \tag{3.74}$$

which corresponds to a half-step in time with $\dot{\mathbf{u}}^n = 0$. This procedure is repeated until equilibrium is reached, specified by the convergence criteria of energy and force residuals. The energy residual is defined as the ratio between kinetic and internal energy, and the force residual is defined as the ratio between the Euclidean norm of force residual and reaction force vectors. The reaction force vector is determined using

$$\mathbf{f}_{\text{r}}^n = \mathbf{f}_{\text{int}}^n(\text{dof}_{\text{fixed}}), \tag{3.75}$$

where $\text{dof}_{\text{fixed}}$ are the degrees of freedom with Dirichlet boundary conditions applied. Finally, the complete time integration scheme is summarised in Algorithm 1.

3.4.2. MASS SCALING
The explicit time integration scheme used for the KDR method requires a time step Δt, which is strictly smaller than the critical time step. With a Δt much smaller than the critical time step, the time integration requires many iterations to reach static force equilibrium and is generally inefficient. Therefore a Δt as close to the critical time step as possible while guaranteeing a stable time integration should be chosen. Alternatively, a dynamic mass scaling approach can be applied, which changes the mass matrix entries in every step while keeping a constant Δt. This approach does not change the outcome because the inertial mass term becomes zero for a static solution and has no influence on the final state. All solutions between the start and static state are non-physical. Barnes [45] suggested a mass matrix formulation based on the maximum eigenvalue of the stiffness matrix. Instead of performing the costly eigenvalue analysis, the Gershgorin circle theorem can be applied, which results in

$$M_i = \lambda \cdot \max\left(\sum_{j=1}^{N} |K_{ij}|\right), \tag{3.76}$$

where $|K_{ij}|$ is the absolute value of the stiffness matrix entry ij. The λ is an additional mass scaling parameter that provides good convergence if set between 0.8 and 1 depending on the problem. A formulation of the stiffness matrix is not stated here but can be found in Wriggers [93]. A final note on implementing the KDR method is that the stiffness matrix is generally sparse, and its sparsity pattern does not change over time. Thus it can be initialised once and kept in memory without re-initialisation.

Algorithm 1 Kinetic dynamic relaxation with variable mass scaling.

1: Initialise deformations **u**, velocities **v**, and kinetic energy W_{kin}
2: **while** $W_{kin}^n / W_{int}^n > \varepsilon_{KE}$ && $\|\mathbf{R}^n\|/\|\mathbf{f}_r^n\| > \varepsilon_R$ **do**
3:      Initialise kinetic energy W_{kin} for previous time steps
4:      Determine external force vector $\mathbf{f}_{ext}$ (Eq. 3.46, 3.52 and 3.56)
5:      **while** True **do**
6:          Determine internal force vector $\mathbf{f}_{int}$ (Eq. 3.57 and 3.47) and mass matrix M (Eq. 3.76)
7:          Compute nodal velocity $\dot{\mathbf{u}}^{n+\frac{1}{2}}$ and displacement $\mathbf{u}^n$ using Eq. 3.70 and 3.69 respectively
8:          Correct $\dot{\mathbf{u}}^{n+\frac{1}{2}}$ and $\mathbf{u}^n$ for Dirichlet boundary conditions
9:          **if** pressure load active **then**
10:             Update external force vector $\mathbf{f}_{ext}$ (Eq. 3.56)
11:         **end if**
12:         Compute kinetic energy $W_{kin}^{n+\frac{1}{2}}$ and update from previous time steps (Eq. 3.71)
13:         **if** $W_{kin}^{n+\frac{1}{2}} < W_{kin}^{n-\frac{1}{2}}$ **then**
14:             Correct deformation vector **u** (Eq. 3.72)
15:             Update internal force vector $\mathbf{f}_{int}$ (Eq. 3.57 and 3.47)
16:             Correct for Dirichlet boundary conditions
17:             Determine reaction force vector $\mathbf{f}_{reaction}$ (Eq. 3.75)
18:             break
19:         **end if**
20:     **end while**
21: **end while**
22: Save results

3.5. VERIFICATION

The derived KDR method with 2-node cable elements and 3-node membrane elements was implemented in Python/Cython as an in-house solver called *mem4py* [97]. Its capabilities are tested on an airbag inflation simulation found in the literature to verify the correct implementation.

3.5.1. INFLATED AIRBAG

A verification problem in form-finding is the inflated square airbag. It consists of two initially flat coinciding square surfaces which are connected at their edges. By applying constant internal pressure, a square pillow forms as depicted in Figure 3.5. The teal mesh corresponds to the undeformed flat airbag, and the grey surface is the inflated airbag after convergence. The displacement in z-direction w_M and the first principal stress component S_1 at the midpoint M has been studied by several researchers for various solution algorithms and wrinkling models [50, 98–100]. Due to symmetry, only an eighth of the square airbag needs to be modelled. The simulation is started with an unstressed flat surface loaded with pressure acting in the normal direction of each element. The edge $\overline{MA}$ is constrained in the y-direction, while $\overline{MB}$ is constrained in the x-direction to
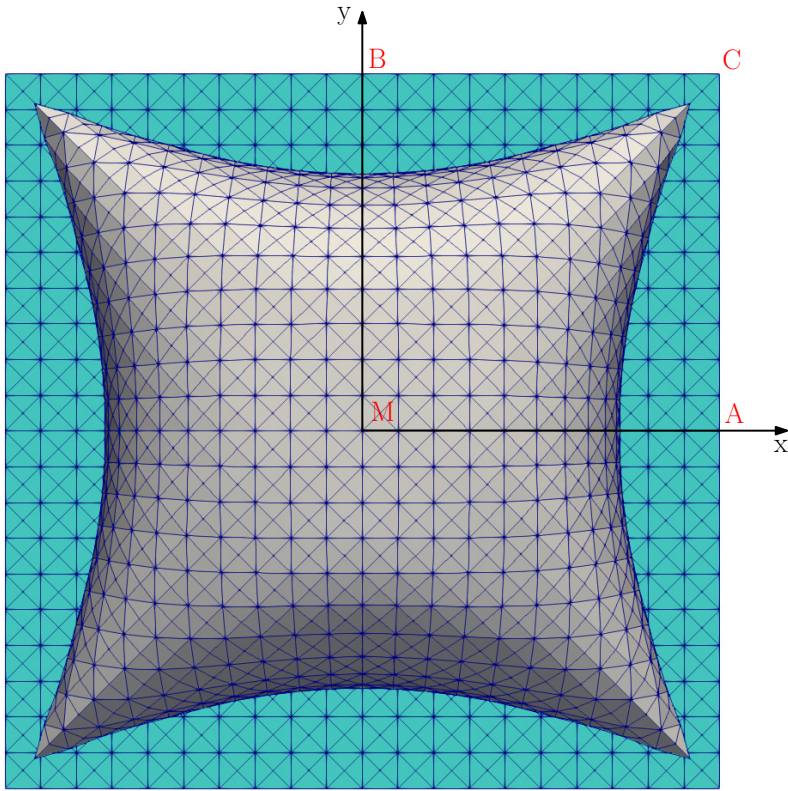
Figure 3.5: Flat (teal) and inflated (grey) airbag

account for symmetry. Also, the edges $\overline{AC}$ and $\overline{BC}$ are constraint in z-direction. Table 3.2 contains input parameters Young's modulus E, Poisson's ratio ν, membrane thickness h, and internal pressure p. The airbag is discretised into quad elements, and each quad is again refined into four triangles of the same size to avoid mesh dependence.

Table 3.2: Inflated airbag simulation input parameters and geometry.

Property	E [MPa]	ν	h [mm]	$\overline{AM}$ [mm]	p [kPa]
Value	588	0.4	0.6	422	5

The simulation was run for various mesh densities without a wrinkling model and Raible's and Jarasjarungkiat's wrinkling approaches. Figure 3.6 depicts the top view of the deformed airbag with and without using a wrinkling model. The contour corresponds to the second principal stress component, which must not be negative according to tension field theory. The right-hand side figure exhibits negative stress regions caused by non-physical material compression. Also, the mesh deforms such that wrinkles occur along the airbag's edges. These wrinkles are merely numerical artefacts that do not represent real wrinkles and are caused by the finite element edges that behave as hinges.
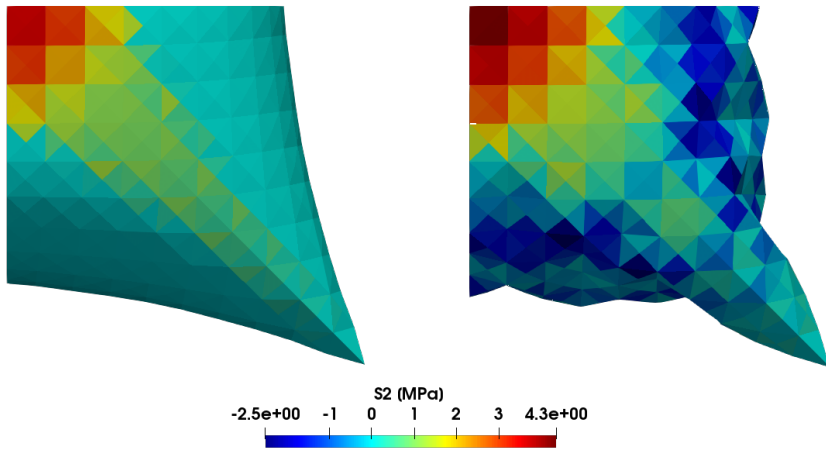
Figure 3.6: Second pricipal stress S_2 field on inflated airbag. Left without wrinkling model, right with wrinkling model based on Jarasjarungkiat et al. [50]

On the other hand, the airbag model on the left-hand side shows no negative principal stress, which confirms that the wrinkling model is working correctly. The elements align smoothly along the surface with the stress field compression-free. For post-processing purposes, the wrinkle orientation can be found through the direction of the first principal stress in each finite element.

A set of meshes with 16 to 10000 equally sized triangles is run, and the resulting z-displacement w_M and first principal stress component S_1 at node M are depicted in Figure 3.7. The mid-point displacements and stress components found in the literature are presented in Table 3.3 which were determined from meshes with 64 and 128 quadrilateral elements.

Table 3.3: Inflated airbag simulation results with 64 quadrilateral or 128 triangular elements.

Author	Contri [98]	Kang [99]	Ziegler [100]	Jarasjarungkiat [41]
w_M **[mm]**	205	214	216	216.5
S_1 **[MPa]**	3.5	-	3.7	3.8

Figure 3.7a depicts w_M plotted against number of elements. The mid-point displacement is underestimated by the simulation without the wrinkling model but slowly approaches the value found in the literature for higher mesh densities. The underestimation can be explained by the membrane element's ability to absorb compression, resulting in a stiffer structure. For higher mesh densities, fewer elements absorb compression because more element edges act as hinges in wrinkled regions. The wrinkling model by Jarasjarungkiat shows a good convergence behaviour, and even for smaller mesh densities, w_M agrees well with values from the literature. Raible's approach results in displacements close to the literature for coarser mesh densities but exhibits oscillatory behaviour

(a) Mid point z-displacement against number of elements.

(b) First principal stress component S_1 at mid point against number of elements.
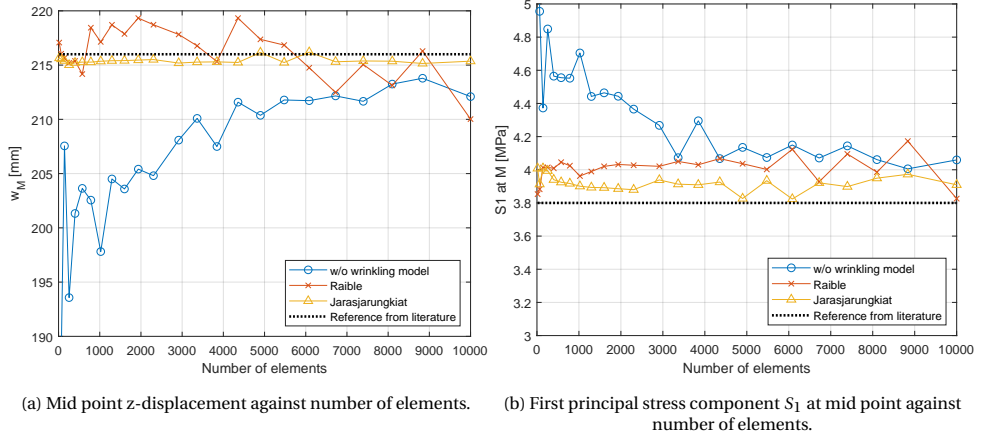
Figure 3.7: Mesh sensitivity

with increasing the number of elements. The oscillations occur because the solver was not able to converge to a satisfying force residual, and when the mesh was manually inspected it could be seen that some elements at the boundary between taut and wrinkled state flipped their state successively which prevents global convergence.

Figure 3.7b depicts the mesh sensitivity of S_1, determined by the stress average of the two elements closest to the corner point M. The stress determined by all three airbag models is overestimated, with the airbag without wrinkling model having the highest stress for small numbers of elements. Both wrinkling model approaches show similar stress values as the literature despite overestimating stress. Raible's method oscillates for higher mesh density, whereas Jarasjarungkiat's method is stable. The difference from the literature can be explained by the use of constant strain triangles, which are less accurate in determining the local stress gradient.

Figure 3.8 shows the energy residual plotted against the pseudo time steps for the three airbag model approaches in two mesh densities. After each energy peak, the kinetic energy reduces consistently, driving the solution to a static state. As mentioned above, Raible's method exhibits oscillatory behaviour in displacement and stress during the mesh sensitivity study. It can be observed in Figure 3.8a that the kinetic energy is oscillating after approximately 3000 time steps without further reducing it. Instead, the kinetic energy jumps between two values after each consecutive peak. By inspecting the finite element model, the stress state in individual elements along the boundary of the wrinkled/taut state oscillates. Therefore, a kinetic energy peak occurs immediately after the restart, and the overall movement of the airbag is prevented. Conversely, Jarasjarungkiat's method fully converges to steady-state, even without employing a maximum number of iterations after which the stress state is kept constant. Similar behaviour is seen in the model without wrinkling model, which takes fewer time steps to converge on the larger mesh.

By inspecting the force residual in Figure 3.9 the oscillatory behaviour of Raible's method is more apparent. It also reveals a shortcoming of the KDR method, which can-
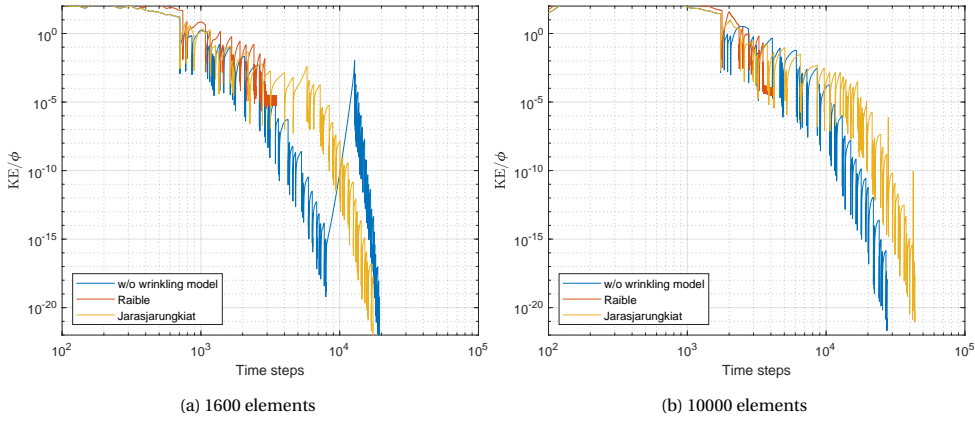
(a) 1600 elements

(b) 10000 elements

Figure 3.8: Ratio between kinetic and strain energy against pseudo time steps.

not proceed to damp the dynamical system effectively to steady-state if a single element is swapping state after each energy peak. Adding additional mass to respective nodes or introducing viscous damping did not stop the oscillations.

In all four figures in 3.8 and 3.9 it can be seen that both kinetic energy and force residual curves consist of two slopes. Most of the displacement occurs in the first region until approximately 6000 time steps. The steep slope occurs subsequently, and the overall airbag shape barely changes, which leads to the question of how much each convergence criterion has to be satisfied to expect sufficiently accurate results whilst keeping the number of time steps at a minimum. For that reason an error analysis for both w_M and S_1 is presented in Figure 3.10. The error is determined with

$$\text{Error}(w_M) = \frac{|w_M^i - w_M^N|}{w_M^N}, \tag{3.77}$$

where w_M^i is the converged z-displacement for given ε varying between $1 \cdot 10^{-1}$ and $1 \cdot 10^{-20}$ for ε_{KE} and $1 \cdot 10^{-1}$ and $1 \cdot 10^{-10}$ for ε_R. As a reference solution w_M^N is used which corresponds to the converged z-displacement for the most stringent ε. For this particular problem of inflating an airbag an error of 0.1% in both displacement and stress can be obtained by using $\varepsilon_{KE} = 1 \cdot 10^{-8}$ and $\varepsilon_R = 1 \cdot 10^{-3}$, respectively.

3.5.2. CONCLUSION

Based on these results, the KDR method successfully determines the shape and stress state of membrane structures. Also, Raible's wrinkling model is numerically unstable in combination with the KDR method and thus not used for the kite simulation. Despite a variable mass formulation, many time steps are still required to reach a static equilibrium. By visual inspection, it can be seen that the overall shape of the structure does not considerably change after 20-30 energy peaks, but the force residual is usually still above $1 \cdot 10^{-2}$ which leads to the conclusion that the force equilibrium is by far not reached and the solver has to continue iterating. A static solution approach using the *Newton-*
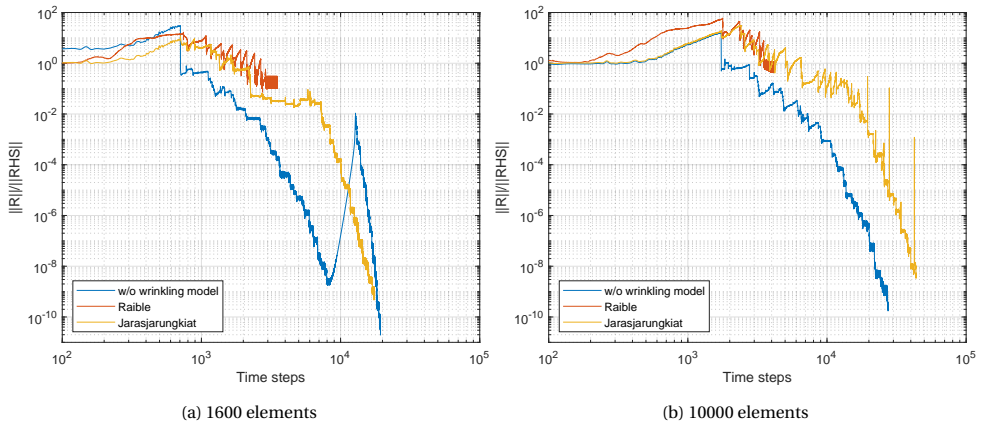
(a) 1600 elements

(b) 10000 elements

Figure 3.9: Ratio between Euclidean norm of residual and external force vectors.

(a) Error in z-displacement
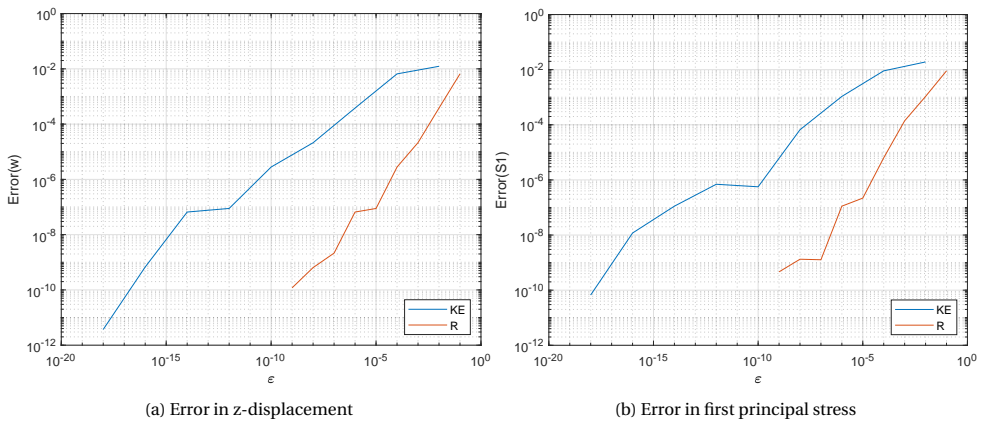
(b) Error in first principal stress

Figure 3.10: Simulation errors for airbag with 400 elements against convergence criterion stringency ε.

Raphson method was applied to the airbag simulation after 20 energy peaks, but the method always diverged.

4

FLUID-STRUCTURE INTERACTION

This chapter presents the coupling between the structural and fluid solvers, which provides the basis for analysing a ram-air kite's aerodynamic and structural properties. First, the fluid solver is introduced, and its functionality is verified on a box wing with a large anhedral. Also, the coupling procedure is introduced in more detail, and the FSI is tested on a ram-air wing for various mesh densities, wind speeds, and trim positions. A validation with flight data from SkySails Power is also presented, comparing simulation results.

4.1. FLUID SOLVER

As described in the literature review, the panel method is a fast computational tool that determines the velocity and pressure distribution over an object subject to airflow in two or three dimensions. Based on the assumptions that the flow is steady, inviscid, and irrotational, the flow field is described by the gradient of the velocity potential and is expressed in integral form with a set of boundary conditions (no wall penetration and Kutta condition at the trailing edge). Flat panels are used to approximate the surface of the wing, and both source and doublet strengths can be computed on each panel. At the wing's trailing edge, wake panels have to be introduced, which enforce the Kutta condition. The velocity and pressure field are then determined by solving linear equations for all unknown source and doublet terms in one step. The time complexity to solve the linear system of equations is proportional to $\mathcal{O}(n^2)$, where n is equivalent to the number of panels. For a thorough derivation of the three-dimensional panel method refer to Katz & Plotkin [101].

A range of publicly available panel codes have been compared based on the requirements that they can be run outside a graphical user interface, and the user should be able to define the mesh in a script format. The tool which satisfies both requirements was found to be *APAME* [102] which is an open-source project licensed under GNU General Public License and utilises linear interpolation for quad and triangular panels. Nodes and their connectivity that form panels define the mesh input for both wing surface and wake. No wake relaxation is done, which relocates the wake panels after each solution

step to form a wake roll-up. *APAME* has been used within a wing optimisation framework with AWE application and has proven to be stable for various wing designs [103, 104].

4.1.1. BOX WING VERIFICATION

APAME is tested on a box wing to study mesh sensitivity and compare its results with a CFD simulation found in the literature. A three-dimensional wing with a sizeable anhedral angle in the form of a biplane configuration joined by end plates for future aircraft was studied by Gagnon et al. [105]. Their wing optimisation framework solved the aerodynamic flow with a CFD solver based on the steady inviscid Euler equations. For verification purposes, their computed aerodynamic coefficients and the span-wise lift distribution are compared with *APAME*.
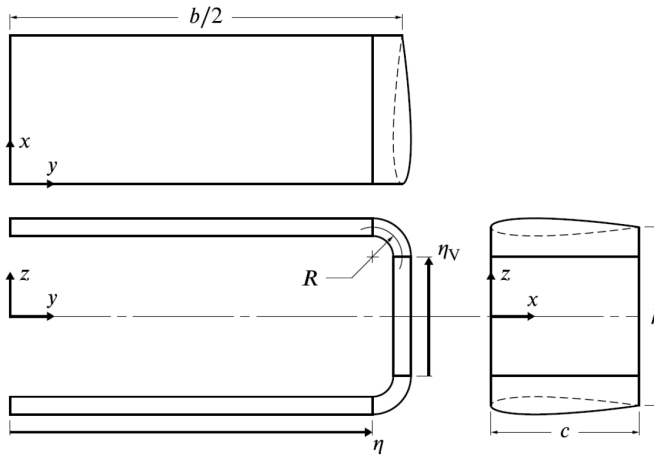

Figure 4.1: Box wing parametrisation [105].

Table 4.1: Mesh sensitivity for box wing.

Parameter	Elements	n_{span}	$n_{profile}$	C_L	C_D
Coarse	4424	9	78	0.5089 (1.78%)	0.01007 (9.32%)
Medium	8968	13	118	0.5067 (1.34%)	0.01000 (8.81%)
Fine	16432	19	158	0.5	0.0097 (5.65%)

Figure 4.1 depicts the box wing geometry and its parametrisation in half-span $b/2$, height h, and radius of corner fillet R. All parameters are defined as a function of chord length taken from their initial design during optimisation, with $h/b = 0.2$, $b = 12c$, and $R = 0.15c$. The wing's aerofoil is a NACA 0012 with a chord length c of one unit length, and the target lift coefficient is 0.5, which corresponds to their initial design during optimisation. A total of three mesh densities are compared, as shown in Table 4.1. The number of panels along the half-span varies from 9 to 19, and the profile outline varies from 78 to 158 panels. The wake panels are orientated parallel to the free stream. For all three mesh
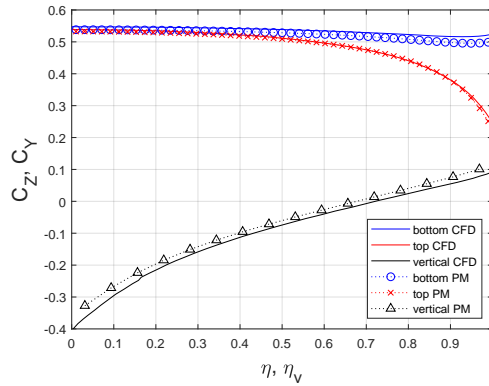
Figure 4.2: Section-wise force coefficients in comparison to CFD solution.

densities, a constant angle of attack of $\alpha = 5.86°$ was used, producing a lift coefficient of 0.5 for the finest mesh. It can be seen that a finer mesh reduces both lift and drag coefficients in comparison to the coarser mesh. In particular, the profile outline around the leading edge has a major influence on both lift and drag due to the surface integration of pressure.

Compared to the CFD solution, their angle of attack to produce the same lift coefficient of 0.5 is $\alpha = 5.41°$ which is 8% lower. In their study, the lift induced drag coefficient C_{Di} is not specifically stated, but the inverse of the span efficiency factor is shown in their figure for their initial design and is approximately equivalent to 0.69. The span efficiency factor for inviscid flow is defined as

$$e = \frac{C_L^2 S}{\pi b^2 C_{Di}}, \tag{4.1}$$

where S is the wing surface area, and by solving for the drag coefficient C_{Di} becomes 0.0092, which is a 6% error in comparison to the most refined mesh resolution. Next, the span-wise force coefficient over both wings and the vertical end-plate are compared, shown in Figure 4.2. The panel method's force coefficients along the span match closely with the CFD results. Discrepancies can be seen close to the wingtip of the lower wing and a constant offset on the vertical end-plate. Despite the discrepancies, it can be concluded that the panel method provides a good approximation of both the lift and drag coefficients, even for wing configurations with large anhedral. The lift induced drag force is more prone to error due to inaccurate surface integration when using a coarse mesh density which motivates a mesh convergence study of a ram-air wing.

4.2. INTERFACE COUPLING

The fluid-structure interaction of a flexible kite occurs on the model interface where aerodynamic pressure acts on the kite's surface, and the structure responds by deforming under the load. Since the deformed shape of the kite is unknown beforehand, an initial shape has to be assumed, and the fluid-structure interaction must be performed

multiple iterations until both fluid and structure interfaces match. The interface matching can be measured by a global variable such as a change in the lift or drag coefficients over the last two iterations or the vector norm of the change of interface deformation $||\Delta\mathbf{u}||$.

There are two general approaches to couple fluid-structure problems: partitioned and monolithic coupling. The partitioned approach couples two or more solvers while each solver simulates a sub-part of the whole physical system. The most straightforward partitioned approach is the explicit coupling, where fluid and structure are solved separately in a staggered scheme. The boundary information on the interface is exchanged after each time step. If both solvers have different time step sizes, the exchange can be done when both solvers reach the same time. Despite its simplicity, this approach may suffer from numerical instabilities or take many small steps. A more elegant approach consists of an implicit coupling between two time-steps such that the difference in displacement on the interface is minimised iteratively, and it is shown in this chapter that both approaches can be efficient methods for the parafoil FSI simulation depending on the kite model.

Finally, the monolithic coupling approach is defined by a single system of equations that represents the entire physical system. Each time step, the system is solved, and in theory, it provides the most accurate coupling approach because the interface boundary conditions are strongly enforced within the algebraic system of equations. Unfortunately, this approach suffers from two problems: time stepping and numerical instabilities. If the system is solved in each time step, the physical system with the smallest critical time step dictates the whole system's time-stepping, leading to massive overhead. Numerical instabilities can occur if the density ratio between fluid and structure strongly deviates from one, such that the algebraic system becomes close to singular.

The partitioned approach is chosen in this work because the Kinetic Dynamic Relaxation approach provides a static solution with many sub-iterations, while the panel method is solved in a single matrix operation. The coupling software *preCICE* [106] (Precise Code Interaction Coupling Environment) provides a solid toolchain that allows the user to easily couple two or more solvers with little effort. *preCICE* handles each solver as a black box, and only on the interface information is exchanged. In the case of non-conforming meshes, the information is interpolated, and *preCICE* provides an implicit coupling method which is introduced in more detail in the following section.

4.2.1. COUPLING ACCELERATION METHODS

Implicit time-stepping methods solve a fixed-point iteration problem between two time steps. Let F be the fluid solver which determines the pressure field p at time step n for a deformation field $\mathbf{u}$, and let S be the structure solver which computes $\mathbf{u}$ at time step n for a given pressure, thus

$$p^n = F(\mathbf{u}^n) \tag{4.2a}$$

$$\mathbf{u}^n = S(p^n). \tag{4.2b}$$

Combining both expressions for the deformation field results in the fixed-point iteration

$$\mathbf{u}_{i+1}^n = H(\mathbf{u}_i^n), \tag{4.3}$$

where $H(\mathbf{u}^n) = S(F(\mathbf{u}^n))$ and i is the iteration index. This formulation can be efficiently solved using *Quasi-Newton* methods making use of a gradient estimation that accelerate convergence at the interface. For a convergence measure, *preCICE* offers a relative and absolute two-norm convergence on an interface field variable such as displacement $\mathbf{u}$. The relative convergence is defined as

$$\frac{||\mathbf{u}_{i+1}^n - \mathbf{u}_i^n||}{||\mathbf{u}_i^n||} = \frac{||H(\mathbf{u}_i^n) - \mathbf{u}_i^n||}{||\mathbf{u}_i^n||} \tag{4.4}$$

and it is used for both implicit and explicit coupling schemes in this chapter. Finally, *preCICE* provides the following coupling schemes for explicit and implicit coupling:

- **Explicit coupling**: Data between both domains is directly transferred on the interface in a staggered scheme using constant relaxation, which the user has to define. According to the *preCICE* manual, this approach is prone to diverge or requires many coupling iterations in the case of strongly coupled applications.

- **Aitken under-relaxation**: The implicit Aitken under-relaxation method uses a variable relaxation factor that scales the deformation vector based on previous iterations. The user has to define a relaxation factor for the first iteration.

- **Anderson acceleration**: Interface Quasi-Newton Inverse Least-Squares (IQN-ILS) [107] this *Quasi-Newton* method estimates the inverse Jacobian matrix of the sub-problem via a pseudo-inverse using the least-squares method. Solutions from previous time steps can accelerate convergence between two time steps. The user must define an initial relaxation and the number of previous time steps and iterations used for the inverse Jacobian estimation. Additionally, a filter is used to ensure linear dependence of the singular value decomposition. Both initial relaxation and filter type and its cutoff limit have a significant impact on the success of the iterative method. Therefore the user has to find a set of parameters resulting in a stable acceleration which is problem-dependent.

4.3. VIRTUAL WIND TUNNEL AND MODEL ASSUMPTIONS

The parafoil's aerodynamic and structural characteristics such as glide ratio, tether and bridles forces, and mechanical stresses are determined in a virtual wind tunnel environment that attempts to replicate a tethered wing's flight conditions. As described in Chapter 1 the power harvesting envelope of a SkySails Power parafoil consists of four phases: the power, transfer, retraction and restart phase, respectively. The kite is flown through the power zone during the power phase, where the major part of the wind vector points along the parafoil's yaw axis. It is then steered in a figure-of-eight trajectory to produce maximum tether tension while the winch controls the apparent wind speed. In order to avoid modelling a whole figure-of-eight trajectory with steering input and transient aerodynamic and structure effects, a steady flight state is assumed to occur between two

turning manoeuvres when the parafoil reaches a constant flight velocity and inflow angle as depicted in Figure 4.3a. The steady flight is defined by an equilibrium state of forces that act on the wing: aerodynamic lift and drag forces, gravity, and tether tension. This equilibrium state is sought during the interface coupling, and with convergence, the model provides insight into the aerodynamic and structural characteristics.

Figure 4.3b depicts the gravity influence on the kite system, and it can be seen that gravity causes the tether to sag in the direction of the ground. Due to system weight and tether sag, the tension in the tether is slightly reduced, and its orientation is not aligned with the kite's geometric elevation angle. For an AWE system utilising soft kites, the weight of the parafoil and tether is less than 1% of the average produced tether force during the power phase, and therefore the gravity influence during the power phase has been neglected in this work.

(a) Kite manoeuvring a figure-of-eight trajectory during power phase. The blue line indicates the straight flight path between two turns where no steering input is given and the parafoil flies at a constant speed.

(b) Schematics tether sag and system weight due to gravity influence on kite system during power phase.
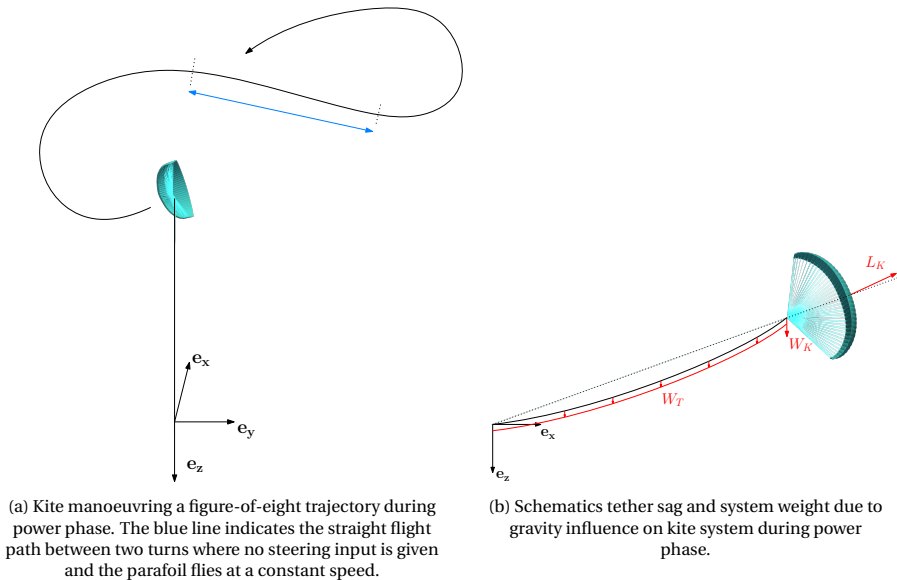
Figure 4.3: Model simplification for the virtual wind tunnel.

The simplified model in steady flight with neglecting gravity exploits a symmetry condition along the parafoil's centre rib. Figure 4.4 depicts the virtual wind tunnel where the tethered parafoil is vertically aligned and a linearly varying V_a inflow vector field acts on the undeformed kite system. Due to symmetry, only half the parafoil has to be modelled, but the *APAME* solver does not provide the functionality of symmetry boundary conditions, and therefore the pressure distribution is determined on the whole wing. Since the angle of attack during steady flight is unknown beforehand, the tethered parafoil can pitch. During the coupling iterations, the kite-tether system moves and pitches until it finds a force equilibrium and the angle of attack corresponding to the parafoil's trim. Effects like tether and bridle drag directly influence the force equilibrium, and for that reason, the overall sensitivities of tether length and deformation due to aerodynamic pressure are studied in more detail in the next section. To avoid a front stall in the first

coupling iteration, i.e. the parafoil produces negative lift and collapses due to a low angle of attack, the V_a inflow is angled with respect to the parafoil with the initial angle of attack α_0 and the aerodynamic coefficients have to be corrected (rotated) by α_0 after convergence.
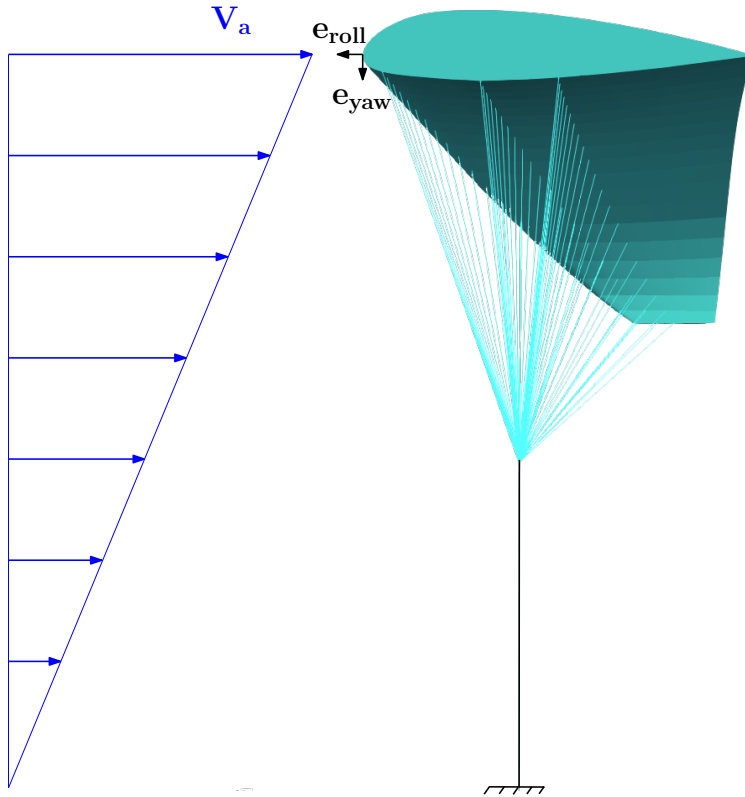

Figure 4.4: Simplified FSI model during power phase assuming steady flight and negligible influence of gravity. The symmetry condition allows to model only half the parafoil. Note that the tether length scale is shortened in this figure.

The V_a inflow distribution for a kite during the power phase can be expressed as the vector sum of winch speed, wind speed and kite speed, respectively, and with constant speed components, the distribution is linearly varying along the tether. In reality, the wind field is never uniform, and the wind field orientation might vary with increasing altitude. Also, the kite speed depends on the kite system's glide ratio, which varies depending on tether length and flight altitude. In order to simplify the V_a inflow, a linear distribution is assumed. From a model perspective, a nonlinear V_a inflow distribution or glide ratio dependence could be implemented with little effort but is beyond the scope of this work.

Finally, the interface coupling procedure is shown in detail in Algorithm 2 which de-

scribes the fundamental coupling between the fluid and structure solvers. The coupling tool *preCICE* initialises the communication between the solvers and, in each iteration, interpolates all field variables between the two interfaces. Due to the steady flight assumption, the coupling iterations occur in a single pseudo time step, and either explicit or implicit coupling methods can be used to find the equilibrium state. Unlike a dynamic analysis, this approach prohibits the Quasi-Newton method to re-use field information from previous time steps, which otherwise might help decrease the number of implicit coupling iterations. A growing difference between both interfaces defines divergent coupling behaviour, and it usually results in an *upside down* flying wing, which a negative lift coefficient can detect. Hence, if C_L becomes negative, the simulation is aborted.

Algorithm 2 FSI coupling procedure.

1: Read structure and fluid mesh. Initialise displacement field **u** and pressure field p.
2: Set iteration counter $i = 1$.
3: **while** $\|\mathbf{u}_i - \mathbf{u}_{i-1}\| > \varepsilon_{\text{FSI}}$ **do**.
4:      **if** $C_L < 0$ **then**
5:          break
6:      **end if**
7:      Run *APAME* on geometry with deformation field $\mathbf{u}_i$.
8:      Correct C_p distribution with internal pressure using Equation 2.7.
9:      Pass C_p distribution to *mem4py*.
10:     Run *mem4py* with current pressure distribution.
11:     $i = i + 1$.
12:     Pass $\mathbf{u}_i$ back to APAME. In case of implicit coupling scale $\mathbf{u}_i$.
13: **end while**
14: Post-processing

4.3.1. QUASI-STEADY AERODYNAMICS

A significant model assumption of the coupled fluid-structure solver using the panel method solver *APAME* is steady aerodynamics. The reduced frequency as a metric can determine whether steady aerodynamics is a fair assumption for a given flow problem. If the reduced frequency becomes too large, both the wing's motion and flow field effectively influence each other to such a degree that the resultant lift force vastly differs from reality without an unsteady aerodynamic model. The reduced frequency is defined as the ratio of characteristic flow and structure frequencies

$$k = \frac{\pi \text{fc}}{V}, \tag{4.5}$$

where f is the structure response frequency due to aerodynamic excitation, c the chord length of the wing and V the flow velocity, and according to aero-elastic theory, the highest reduced frequency for a fair steady assumption should not exceed 0.05 [108].

For a tethered parafoil during the power phase, one must distinguish between characteristic frequencies due to manoeuvres and kite deformations. A manoeuvre frequency is induced by steering and kite accelerations due to winch, gust and tether dynamics.
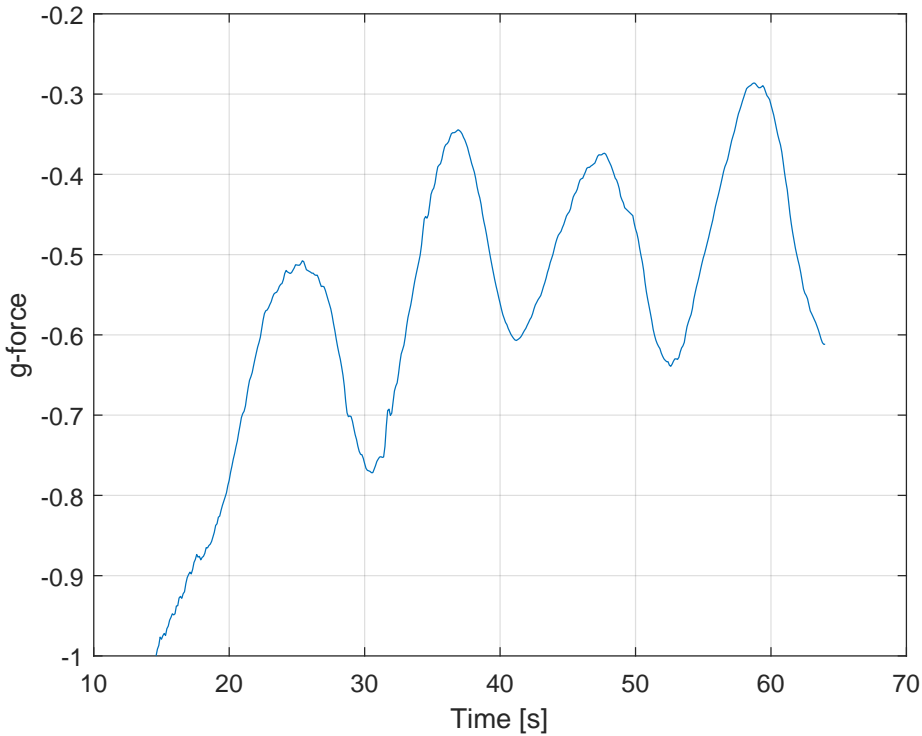
Figure 4.5: Normalised g-force in yaw-axis direction during power phase to illustrate plunging motion of the wing. Next to the periodic acceleration due to the reel-out manoeuvre small oscillations can be observed.

Conversely, characteristic frequencies due to kite deformations are induced by various deformation modes, ranging from global modes deforming the whole wing to sub-scale modes such as trailing edge flutter. Leuthold [109] summarised the aforementioned characteristic frequencies for an LEI kite used for power production. She concluded that a quasi-steady aerodynamic assumption is valid for the LEI kite if sub-scale flutter and seam-rippling effects are regarded as local with negligible influence on the total pressure force. From inspecting the flight video footage, she determined various characteristic deformation modes in the range of 1 Hz or lower. A similar approach was taken in this work by inspecting video footage and audible noises produced by the kite and measurements from the IMU (Inertial Measurement Unit) inside the control pod. Several characteristic effects could be deduced from both video footage and audible noises by the kite, such as the jellyfish mode (a mode where the canopy arc flattens and increases when the flow velocity varies) by the canopy, which was induced by the acceleration after each turn. Also, the bridle lines produced an audible sound but did not show any visible sign of resonance. Local sub-scale effects could be seen at the leading edge where the flow stagnates, and the tension in the fabric is comparably low, and therefore seam-rippling would occur. At the trailing edge, no sign of fabric flutter could be seen. Based on these

results, it can be summarised that both manoeuvre and large scale modes influence the pressure force on the kite, whereas sub-scale effects are purely local and therefore disregarded in this work.

The accelerations acting on the control pod were recorded during each flight and used to determine the characteristic manoeuvre and jellyfish mode frequency of a typical power phase. Figure 4.5 depicts the g-force normalised by its minimum value along the yaw-axis of the parafoil for a 50 seconds window during a power phase. Each peak in acceleration corresponds to the straight flight path between two turning manoeuvres when the kite flies in a steady-state, and the acceleration in the yaw-axis corresponds to a plunging mode with a frequency of approximately 0.1 Hz. Based on the definition of the reduced frequency, a value between 0.0178 and 0.0714 was obtained for tip and wing centre locations, respectively. It can be seen that the reduced frequency at the centre part of the wing slightly overshoots the quasi-steady margin while the rest of the wing lies below. Therefore, in this work, the quasi-steady assumption is applied. By further inspection of the acceleration, some moments during the flight exhibit higher frequencies caused by the unsteady wind field, the winch controller or tether dynamics (whipping). All these effects do not show a particular recurrence and therefore are beyond the scope of this simulation approach.

4.4. VERIFICATION: 160M^2 PARAFOIL

In this section, a parafoil with a flat (none-inflated) wing area of 160m^2 is simulated, and the capabilities of the FSI simulation tool are presented. The kite has never been built and merely serves as a numerical showcase. The bridle system is not optimised, which means all bridles directly connect each line attachment point (LAP) with the pilot position underneath the kite. Its trim position is chosen to be 42% of the centre rib's chord length. The same model has been studied by Folkersma et al. [110] where the authors follow a similar coupling approach, but a RANS solver with OpenFOAM was used instead of a panel method to determine the pressure field acting on the parafoil's surface. Their results serve as verification with the coupling method developed in this work. The aerodynamic and material properties selected for the simulation are stated in Table 4.2. Variable ρ corresponds to the air density, S_{proj} the project surface area used to compute the aerodynamic coefficients, E_m and E_b the membrane and bridle Young's modulus, h_m the membrane thickness, v_m the membrane Poisson's ratio, d_b the bridle diameter, and $C_{D,b}$ the bridle drag coefficient. All simulations were run on an HP ProBook laptop with an Intel CORE i7 1.8GHz processor.

Table 4.2: Aerodynamic and material properties for 160m^2 ram-air wing [110]

Property	V_a	ρ	S_{proj}	$E_m \cdot h_m$	v_m	E_b	d_b	$C_{D,b}$
Unit	[m/s]	[kg/m^3]	[m^2]	[kN/m]	[-]	[GPa]	[mm]	[-]
Value	30	1.2	125	10	0.3	83.6	2.5	1.2

4.4.1. INITIAL INFLOW ANGLE

As described in the previous section, the inflow angle for the global (wind tunnel) reference frame stays constant over all coupling iterations, and the kite is free to pitch and

move to find its equilibrium position eventually. The kite model is used to study the influence of initial inflow angles on convergence behaviour. In the first coupling iteration, the inflow angle corresponds to the angle of attack, but as soon as the kite starts to pitch, the angle of attack is found by the sum of inflow and pitch angle with respect to the centre rib. A range of initial inflow angles starting from 5 degrees to 30 degrees in steps of 5 is compared in Figure 4.6. The chosen coupling scheme is explicit without initial relaxation. It can be seen that both lift and drag coefficients converge to a constant value after approximately ten iterations when the kite approaches force equilibrium on the coupling interface. The graphs indicate that a sizeable initial discrepancy between α_0 and the trim angle of attack results in higher initial amplitudes in lift and drag coefficients. Also, angles of attack at 5 and 10 degrees require more than 20 iterations until convergence which lie below the trim angle of attack. Therefore, a value of 15 degrees for α_0 was chosen for the rest of this section.
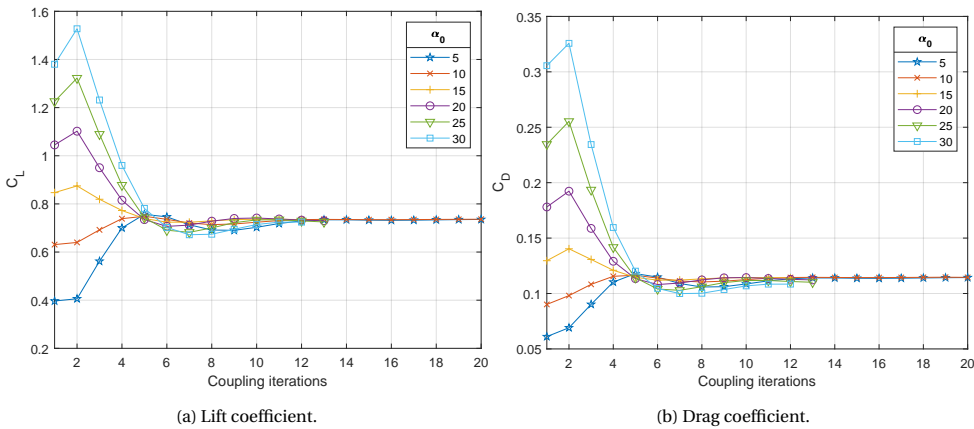

(a) Lift coefficient.

(b) Drag coefficient.

Figure 4.6: Aerodynamic coefficient against coupling iterations for various initial inflow angles.

4.4.2. MESH SENSITIVITY

A thorough study on mesh and coupling convergence is done on the parafoil using three mesh densities with details stated in Table 4.3. The refinement occurs along with the rib profile, with the coarsest mesh having 40 and the most refined having 80 nodes. The nodal distance is progressively reduced by 5% from trailing to the leading edge to account for the leading edge curvature. The span-wise discretisation is defined such that the panel element's aspect ratio is close to 1. The fluid surface mesh consists of quad elements, whereas in the FE mesh, the quads are broken into two triangles, and therefore both meshes conform on a nodal basis. A consistent nearest-neighbour interface interpolation between both meshes is chosen, interpolating the deformation and pressure field variables.

Figure 4.7 depicts three parafoil fluid meshes' front and top view after reaching coupling convergence. It can be seen that more detail in deformation, such as the dents at the leading edge, are more pronounced for the most refined mesh density, which in re-

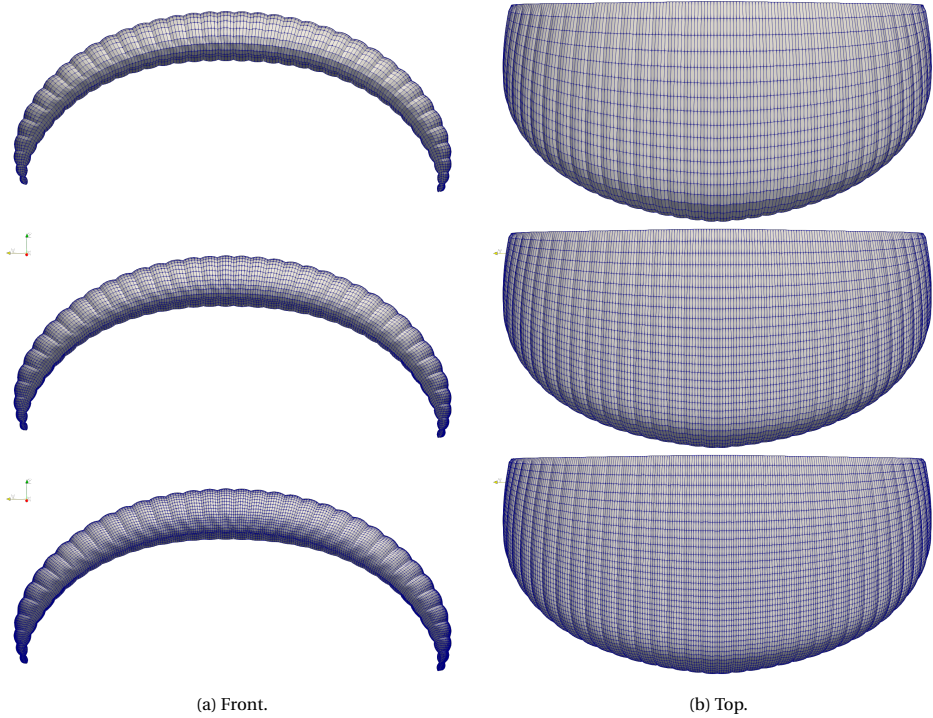(a) Front.   (b) Top.

Figure 4.7: Aerodynamic panel distribution from converged FSI for three mesh densities from top to bottom in decreasing order.

turn has an influence on the pressure field determined by *APAME*. The fluid mesh only consists of surface and wake panels, and due to the absence of symmetry boundary conditions in *APAME* the whole wing has to be simulated. The finite element mesh additionally consists of ribs and bridles such that the ratio of the number of elements between FE and fluid mesh is approximately 3:2.

Table 4.3: Mesh convergence study.

Mesh density	Coarse	Medium	Fine
FE elements	8713	17282	28234
Fluid panels	6460	12540	19950
Nodes along profile	40	60	80

All three computational models were solved with explicit, Aitken under-relaxation, and IQN-ILS using QR1 and QR2 filters with limits ranging from 10^{-1} to 10^{-6}, and in all cases, an initial relaxation was used ranging from 0.1 to 1.0 in steps of 0.1. First, the relative two-norm convergence of the interface deformation vector of all three models can be seen in Figure 4.8. Only cases that successfully converged to 10^{-3} within a total of 20 coupling iterations are shown here. For all cases, explicit coupling without initial relaxation took between 12 and 13 iterations and is one of the fastest coupling methods. The Aitken

coupling did not converge during the 20 coupling iterations, and the IQN-ILS method only converged using the QR1 filter with various initial relaxation factors. The excellent performance of the explicit coupling is surprising because, in the *preCICE* manual, it is recommended to avoid it due to stability issues and more significant numbers of coupling iterations it usually requires. Also, the IQN-ILS method appears very sensitive to the initial relaxation, where a change of 0.1 even leads to divergence in some cases.
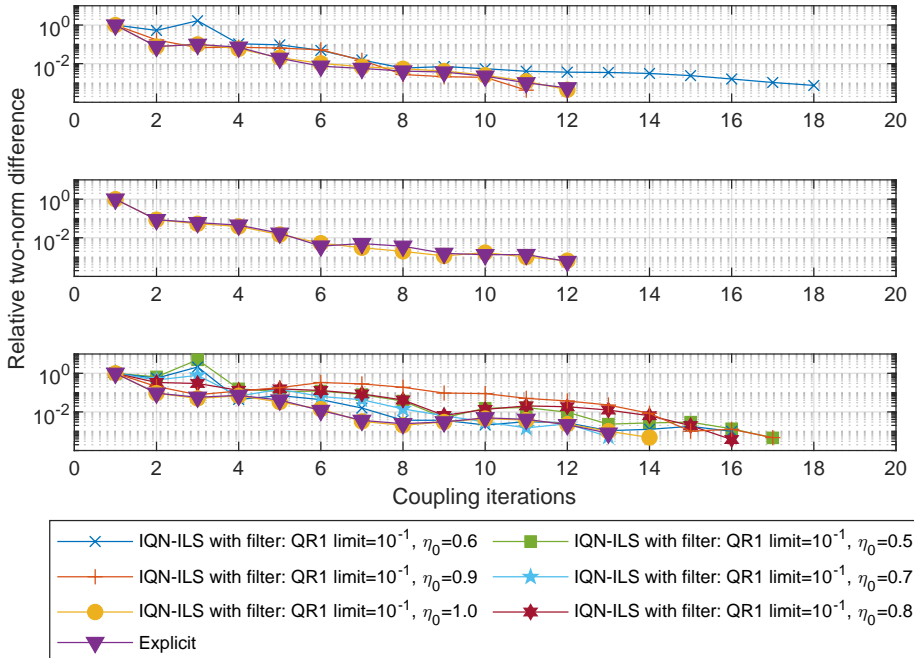
Figure 4.8: Relative two-norm convergence of the interface deformation vector during FSI simulation. Top figure corresponds to coarse mesh density, middle to medium, and bottom figure to finest mesh density.

By studying the lift and drag coefficient progression for the coarse mesh in Figure 4.9 an oscillatory behaviour in all cases can be seen. Both lift and drag coefficients drastically increase after the first iteration and drop close to the final value. The initial peak is caused by the parafoil reacting to the initial angle of attack, resulting in a pitch motion and aft movement of the entire wing. Both explicit and implicit coupling methods show a damped oscillation, while the IQN-ILS method tends to jump more drastically between coupling iterations.

   Similar oscillatory behaviour can be seen in Figure 4.10 for the medium-sized mesh while only the explicit and IQN-ILS method with $\eta_0 = 1$ converged within 20 coupling iterations. Also, the explicit and implicit coupling progression is very similar, which is valid for all mesh densities, implying that the QR1 filter with limit 10^{-1} and $\eta_0 = 1$ does not fully benefit from the Quasi-Newton method with these filter parameters.

   Figure 4.11 depicts the coupling progression of the fine mesh density. In this case, a wider range of IQN-ILS solutions converged within 20 coupling iterations. By inspecting
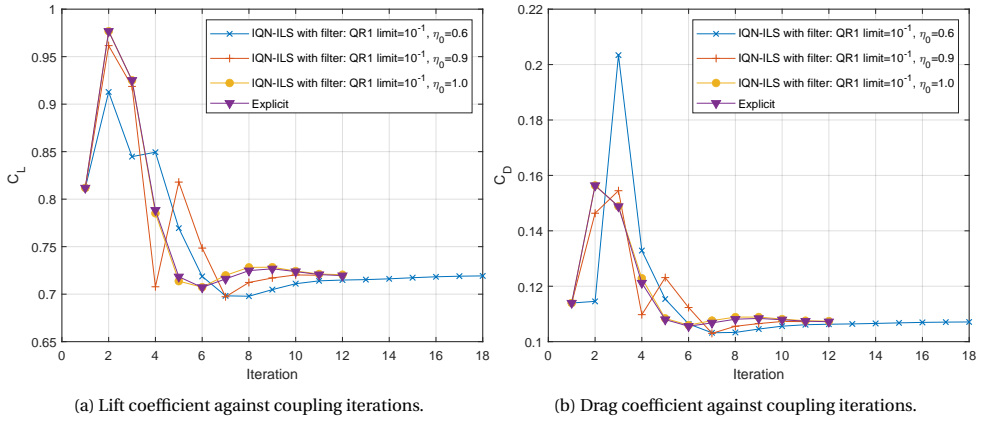
(a) Lift coefficient against coupling iterations.

(b) Drag coefficient against coupling iterations.

Figure 4.9: Coarse mesh convergence.

(a) Lift coefficient against coupling iterations.

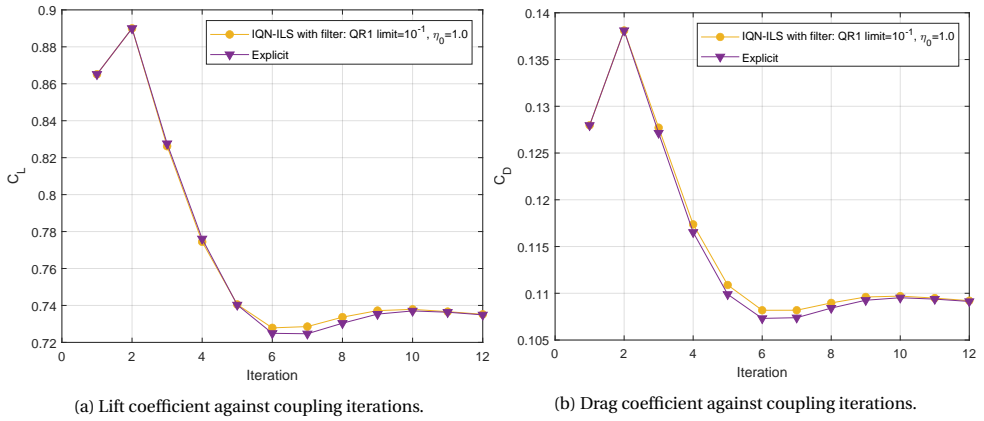(b) Drag coefficient against coupling iterations.

Figure 4.10: Medium mesh convergence.

the progression of different values of η_0, it can be seen that lower values result in larger initial oscillations. In the *preCICE* manual, an initial relaxation of 0.1 is recommended while large values tend to cause instabilities, but for this static coupling approach in this work, larger η_0 values stabilise the coupling rather than causing divergence.

In summary, both explicit and IQN-ILS methods exhibit an overall good convergence behaviour performing well for all mesh densities. While no initial relaxation for the explicit coupling is sufficient, a η_0 between 0.5 and 1 results in the fastest convergence for the IQN-ILS method depending on the mesh density. It should be noted that a more thorough tuning of η_0 could lead to a better performance of IQN-ILS as stated in the *preCICE* manual, but a convergence after 12-15 iterations is sufficiently fast for this application for now, and therefore no further effort in filter tuning was undertaken.

Next, the influence of mesh size on the converged lift and drag coefficients is studied, depicted in Figures 4.12. It can be seen that both lift and drag increase from coarse
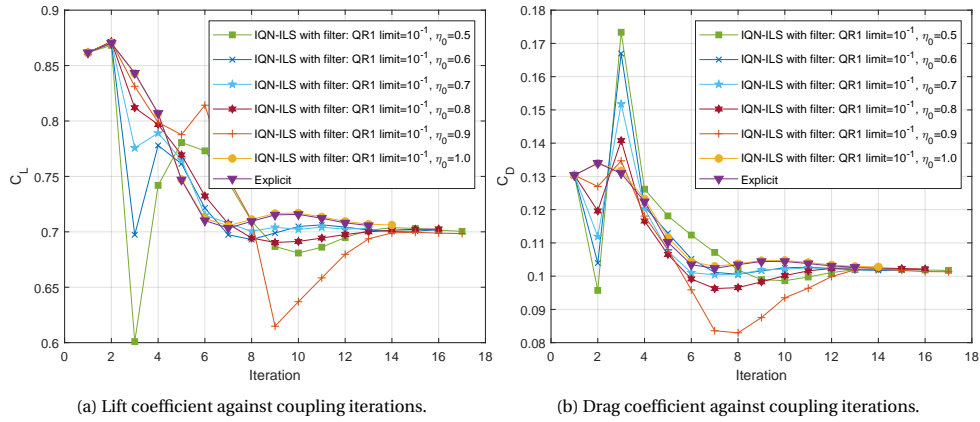
(a) Lift coefficient against coupling iterations.

(b) Drag coefficient against coupling iterations.

Figure 4.11: Fine mesh convergence.
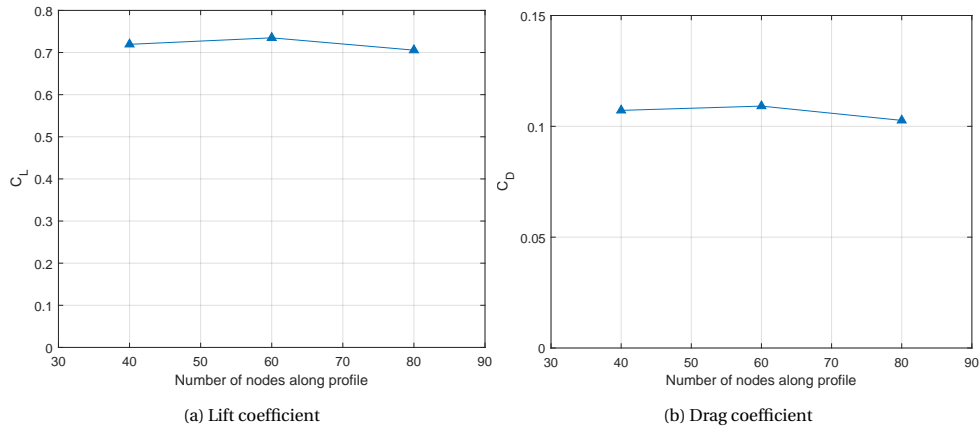

(a) Lift coefficient

(b) Drag coefficient

Figure 4.12: Lift and drag coefficient convergence for three mesh densities.

to medium mesh size and then drop to a lower value for the fine mesh. The change in lift and drag is caused by a refined representation of the profile's curvature and span-wise ballooning curvature. Also, a more refined mesh density introduces more pronounced local deformation effects like the leading edge dents due to stagnation pressure. As a result of the effects mentioned above, the aerodynamic pressure field will change accordingly, and with it, the profile shape and angle of attack lead to a slightly different wing geometry. For comparison, a refined mesh density using 100 nodes along the profile was set up and solved, which suffered from severe local deformations around the A-LAP to such a degree that the local pressure field became nonphysical. This clearly demonstrates that the mesh refinement does not necessarily result in a more accurate lift and drag coefficient when the local deformations increase to an extent where the material model assumptions for small strain become invalid. Also, local surface irregularities due to mesh refinement may result in nonphysical pressure spikes in the panel code. The
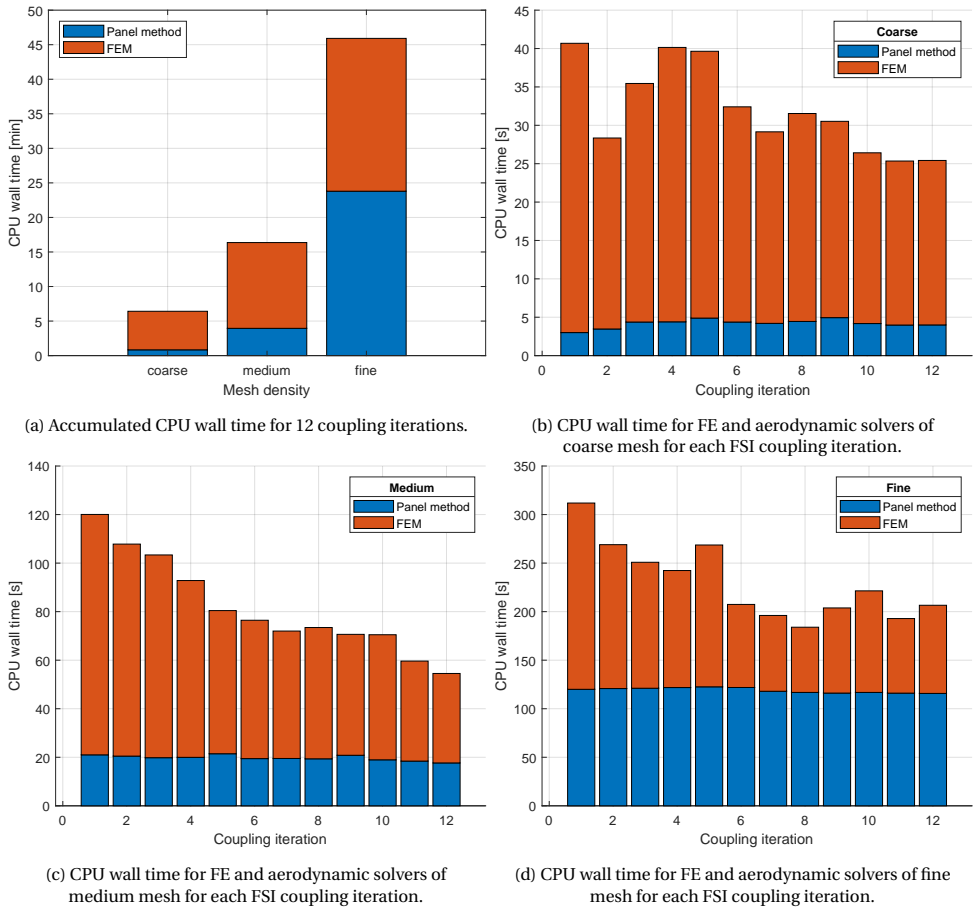
(a) Accumulated CPU wall time for 12 coupling iterations.

(b) CPU wall time for FE and aerodynamic solvers of coarse mesh for each FSI coupling iteration.

(c) CPU wall time for FE and aerodynamic solvers of medium mesh for each FSI coupling iteration.

(d) CPU wall time for FE and aerodynamic solvers of fine mesh for each FSI coupling iteration.

Figure 4.13: CPU wall time for various mesh densities.

most refined mesh resolution is used for the rest of this section unless expressly stated to capture most of the local deformation dependent effects.

Finally, the CPU wall time for each of the three mesh densities are compared in Figure 4.13. As already mentioned, both coarse and medium mesh densities converged after 12 coupling iterations using an explicit coupling, whereas the fine mesh took 13 iterations. For the sake of quantitative comparison, the first 12 iterations for all mesh densities are taken into account. Figure 4.13a depicts each mesh's accumulated CPU wall time and the respective FEM and panel method contributions. The coarse mesh took approximately 6 minutes, with the panel method contributing only 10% of the CPU wall time. The medium-mesh converged after 17 minutes, whilst the panel method took 4 minutes. The fine mesh resolution took approximately 46 minutes to complete 12 iterations with a much larger contribution of the panel method of almost 50% due to the quadratic scaling of the matrix solver. Figures 4.13b, 4.13c, and 4.13d show the time for each coupling iteration and it can be seen that the initial FEM computations are more time consum-
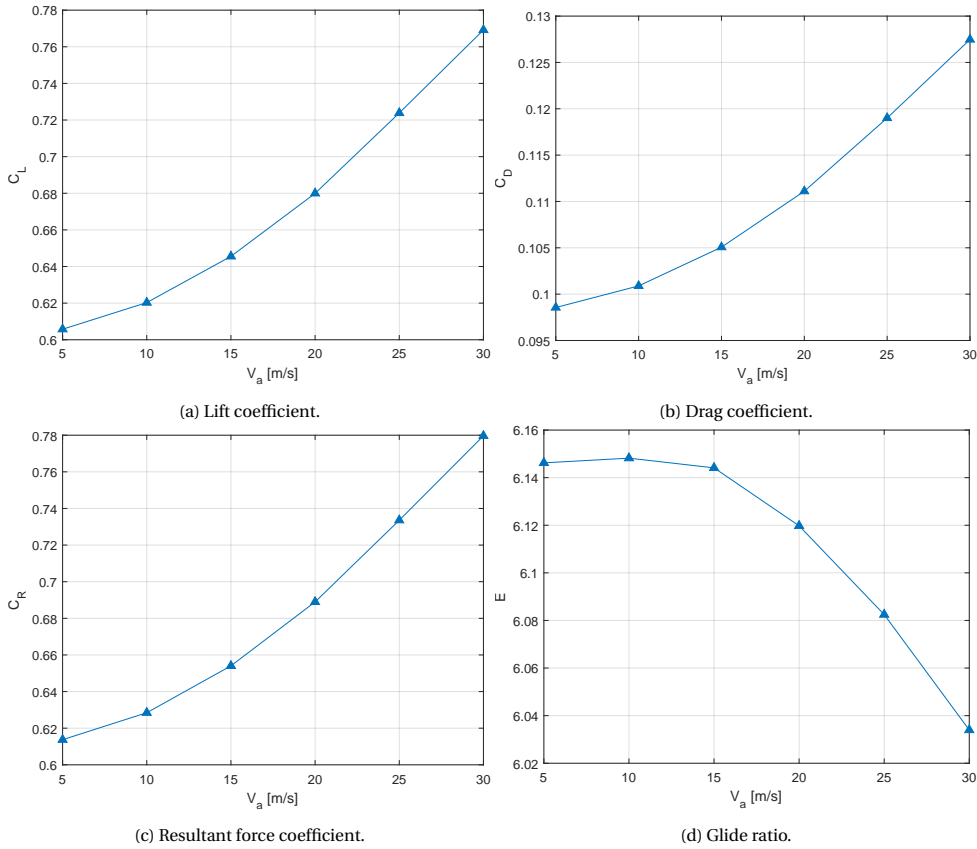
(a) Lift coefficient.

(b) Drag coefficient.

(c) Resultant force coefficient.

(d) Glide ratio.

Figure 4.14: Aerodynamic parameters plotted against apparent velocity V_a.

ing. During the initial coupling iteration, the structure is undeformed and far from its equilibrium position, and with more coupling iterations, the kite moves further towards its equilibrium. Since the dynamic relaxation is based on a time integration scheme, it requires more time increments if the model is far from its equilibrium.

4.4.3. APPARENT VELOCITY INFLUENCE

An important feature of the developed method is simulating the parafoil's deformation during the power phase and its influence on aerodynamic characteristics. In this section, the apparent wind speed is varied between 5 and 30 m/s and its influence on the lift, drag, glide ratio and C_R is shown. Figure 4.14 depicts the aerodynamic coefficients as a function of V_a, and it can be seen that all coefficients increase by approximately 30% going from 5 to 30 m/s apparent wind speed. The change in glide ratio in Figure 4.14d on the other hand slightly decreases with higher V_a. Figures 4.15a and 4.15b depict the change in angle of attack and projected wing area respectively. The angle of attack is measured using the chord line at the centre rib, which increases by 1 degree from 5 to
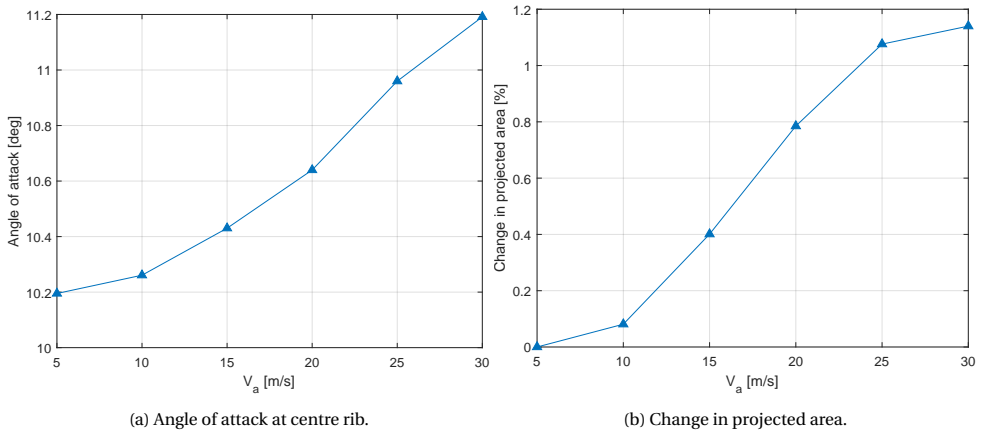
(a) Angle of attack at centre rib.

(b) Change in projected area.

Figure 4.15: Angle of attack and change in projected area plotted against apparent velocity V_a.

30 m/s of V_a. The projected area is determined by summing all wing surface panels and their respective normal vectors perpendicular to the inflow vector pointing in lift direction, and it can be seen that the area is increasing by 1%.

The most peculiar effect caused by larger values of V_a is the striking change in lift and drag coefficients whilst the angle of attack is only changing by 1 degree. To illustrate the reason for such lift and drag increment Figure 4.16 depicts the parafoil at its centre rib for $V_a = [10, 20, 30]$ m/s in the colours blue, red and turquoise respectively. A small change in profile shape can already be seen between 10 and 20 m/s, where the profile thickness and curvature at the suction side become more prominent, and the A-LAP to B-LAP distance slightly decreases due to the pressure load acting between them. This effect is even more prominent in the case of V_a=30 m/s where the overall profile curvature on the suction side is massively increased and the LAP distance is further decreased, and this change in overall profile shape is the main reason for the increased lift and drag for higher V_a. It should be noted that the potential flow solver *APAME* is not able to reproduce viscous flow effects, which could, on the contrary, represent local flow separation. Such a drastic increase in profile curvature in combination with the given angle of attack may otherwise result in a separation bubble after the pressure peak, which increases the local pressure and results in less prominent deformations. Therefore, the numerical results at high velocities should be interpreted with care due to their self-enhancing nature (a higher curvature leads to lower pressure and produces an even higher curvature).

It is important to note that the bulging at the bottom side between the A-LAP and B-LAP is a sign of poor rib profile layout and LAP positioning. A better design choice could move the lowest pressure further toward the leading edge such that more load is transferred to the A-LAP, or the A-LAP should be moved further aft in the current design such that the in-plane rib bending becomes less prominent. Additionally, the material model assumptions for small strain do not hold for the V_a=30 m/s case, and the results should be interpreted with care. At the same time, the large deformations indicate that either the rib should be made of thicker/stiffer material or local reinforcements should be attached to support each region around the LAPs such that the concentrated load
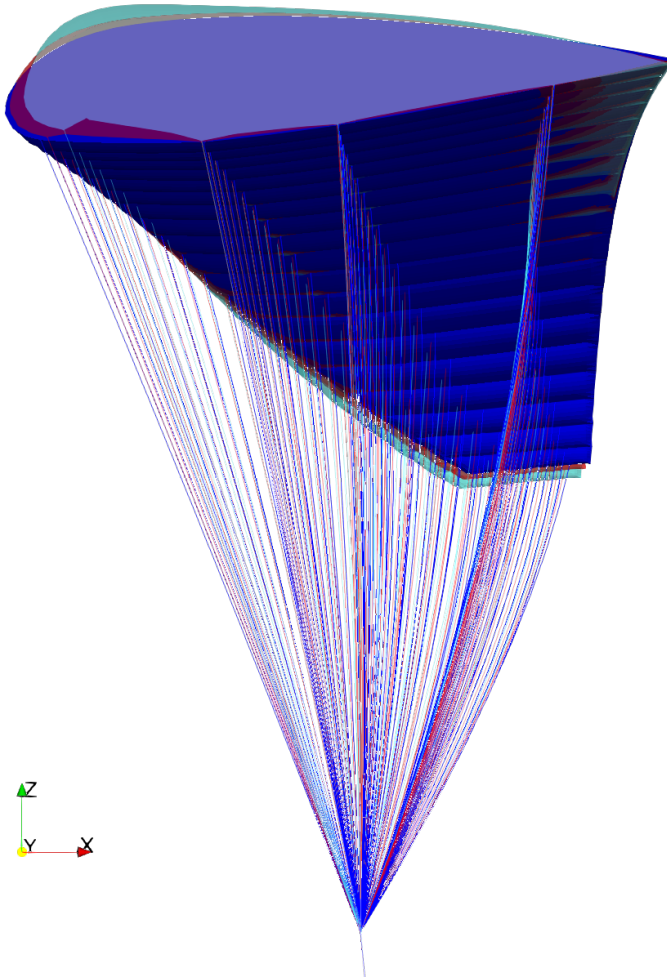
Figure 4.16: Deformed parafoil at symmetry plane for V_a=[10, 20, 30] m/s in blue, red and turquoise respectively.

does not cause the material to break.

4.4.4. INFLUENCE OF TRIM

This section studies the effect of trim position on the parafoil. The trim position is defined as the pilot's chord-wise position underneath the canopy. Similarly, for parafoils with AWE application, the chord-wise location of the tether connection is the trim position, and it determines the angle of attack the wing flies. Folkersma et al. [110] did study the trim position of the parafoil geometry using RANSE simulation and the same structure solver developed in this work. Their results provide a basis for verifying how both solving approaches differ and how the potential flow solver compares to a steady-

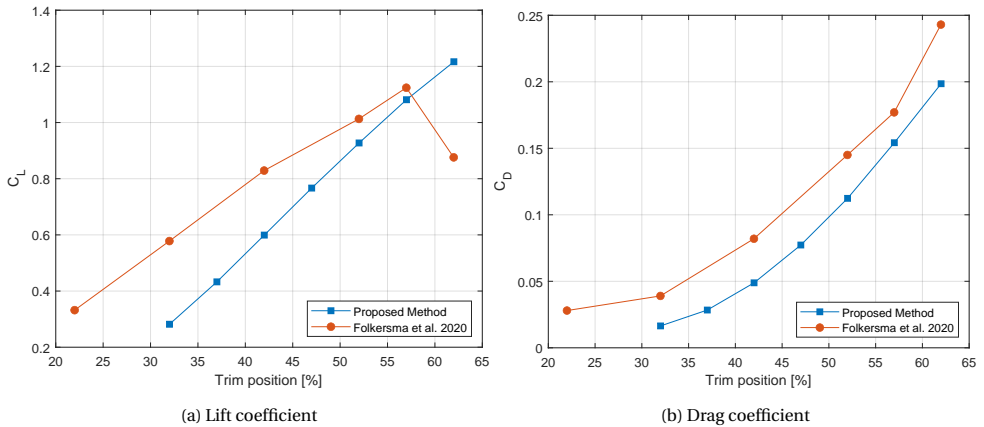(a) Lift coefficient   (b) Drag coefficient

Figure 4.17: Aerodynamic coefficients against trim position along centre rib in [%].

state RANSE solution. In their publication, the trim position is varied between 22 and 62% with respect to the centre rib, and lift and drag coefficients are presented for a V_a of 10m/s. Their lift and drag coefficients are determined solely from the RANSE simulation, while the tether and bridle drag is not shown but taken into account during the coupling iterations to find the equilibrium position. For a direct comparison Figure 4.17a and 4.17b depict the lift and drag coefficients as a function of trim position. It can be seen that the difference in lift slope and values at given trim positions strongly deviate between the proposed FSI method using the potential flow method and the RANSE approach. When inspecting the deformed parafoil geometry presented in Folkersma et al. [110] it was found that the A bridle line was not in tension which indicates that their finite element solution did not properly converge to a force equilibrium, and therefore a direct comparison is impractical.

In order to still compare the potential flow and RANSE solution, the angle of attack at the centre rib was extracted, and the corresponding lift and drag coefficients were determined. This approach only gives an approximation since the parafoil could twist due to the incoming flow, which is not reflected in the angle of attack at the centre rib. Also, as stated in the previous section, the change in profile due to deformations has a more prominent influence on the lift and drag coefficients. Figure 4.18a and 4.18b show both lift and drag coefficients as a function of angle of attack for both proposed method and RANSE solution. It can be seen that both lift and drag have a similar trend until larger angles of attack, where the RANSE solution starts to drop in lift due to flow detachment. As expected, the potential flow stays attached to the wing without reducing lift at high angles of attack. The drag coefficient shows a good match between the two solutions for angles of attack smaller than 15 degrees when both curves start to deviate.

Similarly, the resultant force coefficient and glide ratio in Figure 4.18d and 4.18c as a function of angle of attack are shown. The resultant force coefficient C_R plot is very similar to the lift polar, which emphasises the need for a high lift when a sizeable pulling force is desired since the lift dominates by a factor of 5-10 depending on the angle of attack. When comparing the glide ratio of both approaches, a good match except for low

(a) Lift coefficient

(b) Drag coefficient

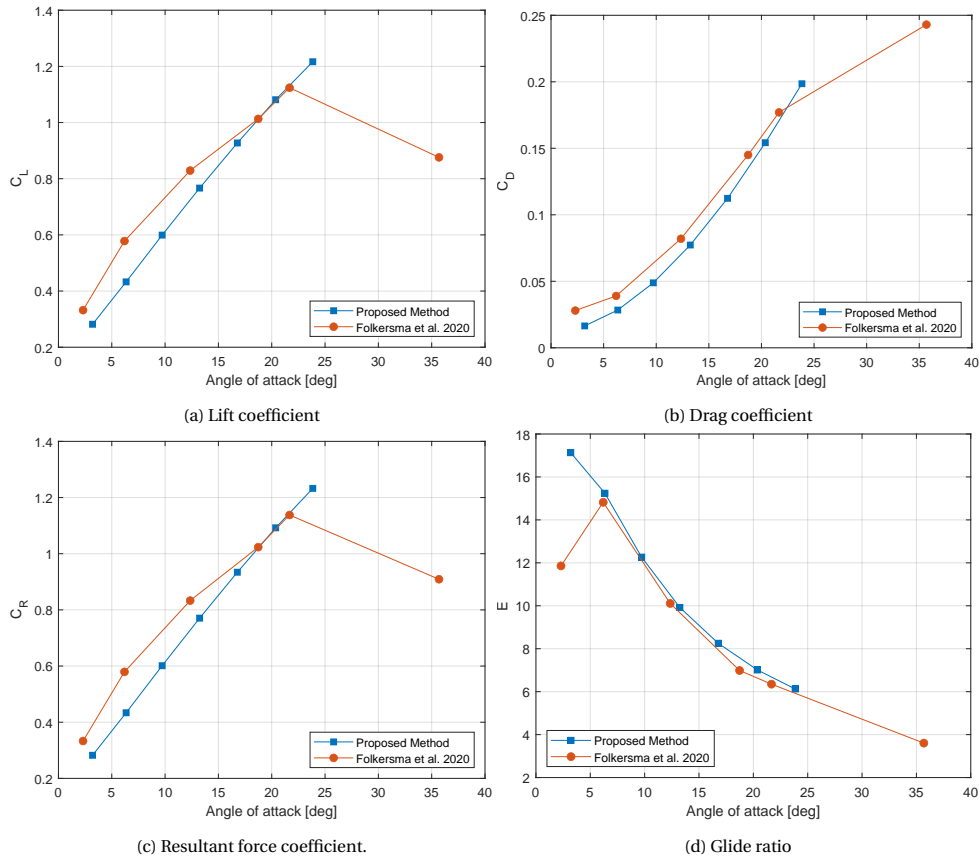(c) Resultant force coefficient.

(d) Glide ratio

Figure 4.18: Aerodynamic parameters for a range of angles of attack.

angles of attack of around 5 degrees can be seen despite the differences in lift and drag. A well-matching glide ratio means that the aerodynamic resultant force vectors obtained by both methods point in the same direction, whereas a difference in C_R indicates a difference in their magnitude.

Finally, the pressure coefficient acting at the centre rib for a trim of 42% is presented in Figure 4.19. Despite having the same trim, the measured angle of attack from the RANSE simulation corresponds to 12.4 degrees, whereas the angle of attack obtained by the proposed method is 14.8 degrees. The overall C_P distributions have a similar appearance. The panel method results in a steeper slope in the first 10% of the chord, and its peak is 0.5 lower than obtained by the RANSE. Also, the LAPs create a kink which causes a drop in pressure displayed by both solvers. Especially the panel method reacts to the A-LAP kink with a local pressure drop due to the local panel deformation resulting in larger angles between neighbouring panels.

It can be concluded that the panel method can determine a fair approximation of the pressure field compared to the RANSE simulation. Care should be taken at large defor-

4

mations that generally cause a strong and even nonphysical pressure drop. In the case of an initial design tool for parafoils, the panel method allows a fast and relatively accurate pressure field without extensive time investment in creating a volume mesh and computation time caused by the RANSE simulation. Also, aerodynamic parameters like lift and drag are approximated within a 30% difference for a range of angles of attack. Nevertheless, it should be emphasised that the definition of an angle of attack for soft kites is not trivial due to possible chord deformation and rotation. A better way to compare the solutions is the trim position defined on the undeformed kite geometry.
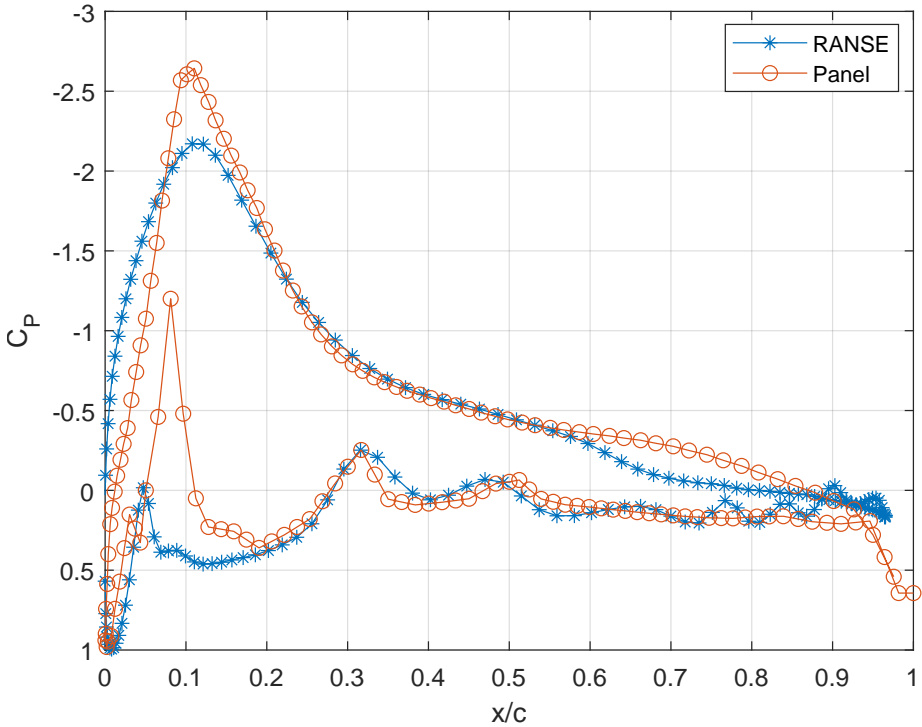

Figure 4.19: Pressure coefficient along chord on centre rib comparing RANSE and panel method solutions. The effective angle of attack is 12.4 degrees from the RANSE and 14.8 degrees from the panel method.

4.4.5. MECHANICAL STRESS IN PANEL AND RIBS

In this section, the mechanical stress acting on both panel and rib is analysed, and a comparison between the numerical solution obtained by the FSI and the analytical expression derived in Section 2.3 is presented. Each panel in the parafoil is enclosed by two ribs, and the tangential stress component σ_t acting in span-wise direction at the mid-plane between the neighbouring ribs is plotted for both top and bottom panel at cell 1 and 8 in Figure 4.20a and 4.20b respectively. All stress values were normalised by the dynamic pressure, and the Cauchy stress component in the span-wise direction determined by the finite element solver is illustrated in blue. The stress peak is located

(a) Cell number 1 (between first and second rib).

(b) Cell number 8 (between rib 8 and 9).

(c) Normalised maximum tangential panel stress for each cell starting from symmetry plane to wing tip from both numerical and analytical models.

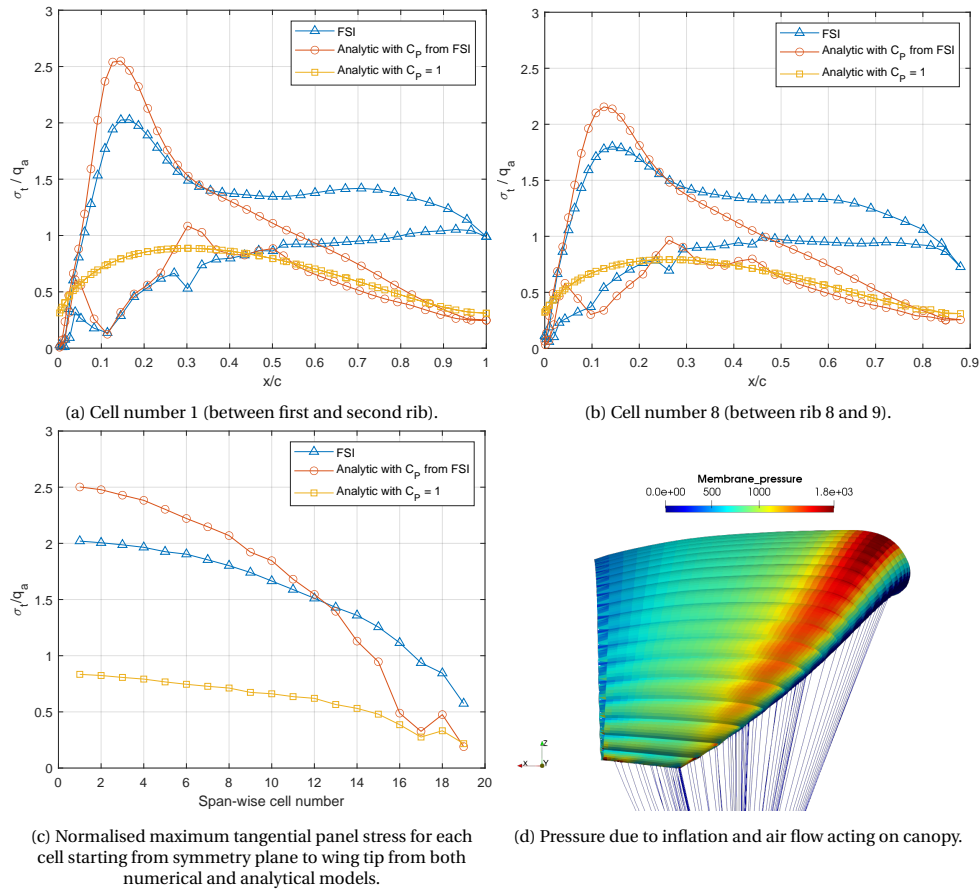(d) Pressure due to inflation and air flow acting on canopy.

Figure 4.20: Span-wise Cauchy stress in panels.

approximately at 15% chord length, and the stress approaches zero close to the leading edge where the flow stagnates. The stress peak is twice as large as the stress acting at the trailing edge, and the overall stress distribution for the top side is approximately twice as large as for the bottom panel. A similar trend can be seen in Figure 4.20b for cell number 8 with a less prominent stress peak than cell number 1.

Next to the numerical solution, two analytical solutions are shown. The yellow graph is the tangential panel stress based on Equation 2.10 with a constant $C_P=1$ distribution corresponding to the ballooned state without any external flow acting on the cell (the C_P here is defined positively to obtain the same sign as the panel stress). The stress peak occurs at the thickest location of the profile due to the assumption that the panel radius of curvature is a function of local rib thickness. The graph underestimates the acting stress by a factor of 2, and its peak is located further aft at approximately 30% chord length. The red graph is also based on Equation 2.10 but the C_P distribution is taken from the panel method based on the converged FSI geometry with internal and external
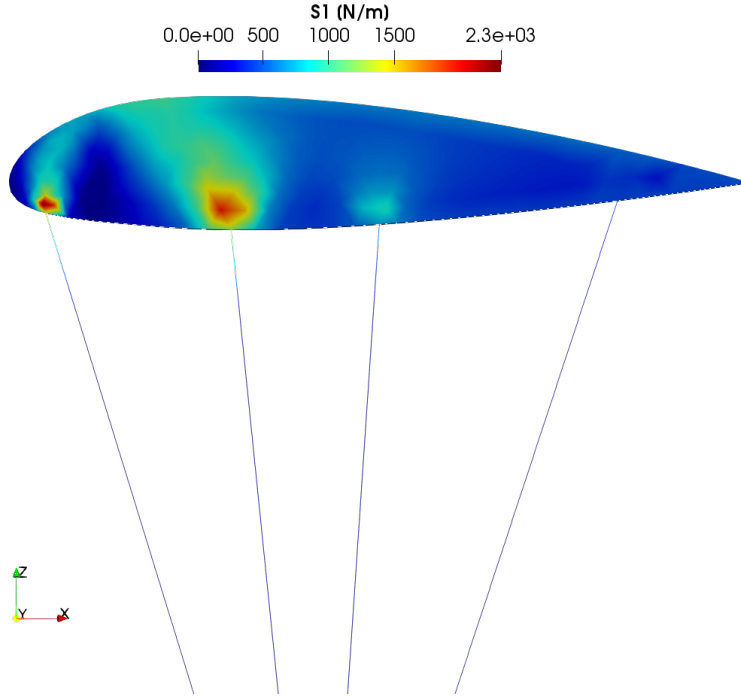
Figure 4.21: First principal stress component S_1 per unit thickness [N/m] contour plot showing loaded centre rib for $V_a = 30$m/s and trim at 42%.

pressure superimposed. In both cells, the stress aligns well with the numerical results in the first 10% of the chord length and then overshoots the stress peak and reduces to a similar value as the ballooned cell at the trailing edge.

The span-wise stress distribution of the top side panels is depicted in Figure 4.20c where the maximum stress from both numerical and analytical results are compared. The graph in blue corresponds to the numerical solution, and it exhibits a smooth decrease in panel stress starting from the centre to the wingtip. Interestingly, the cell width for the first 14 cells is of equal size, and the 25% difference in panel stress purely originates from a combination of span-wise acting forces and the reduction in local angle of attack, both due to the wing's anhedral. To illustrate the decrease in peak pressure when moving from the centre towards the wing tip Figure 4.20d shows the external pressure acting on the wing as a contour plot.

For the analytical solutions shown in yellow and red, the maximum panel stress in each cell was plotted, which is not necessarily located at the exact location as the maximum panel stress determined by the FE solution. It can be seen that the solution based on a $C_P = 1$ vastly underestimates the panel stress. Conversely, the analytical solution based on a pressure distribution from *APAME* overestimates the stress close to the centre due to the absence of span-wise forces, which effectively flatten the ballooning.

It can be concluded that the analytical expression does not correctly match the stress distribution along the chord and span in comparison to the numerical results. Especially the stress at 50% chord length until the trailing edge strongly deviates. Nevertheless, applying the analytical panel stress formulation with a C_P distribution from the actual wing results in maximum stress approximately 20% higher than the numerical solution without the need of a full FSI simulation. For the initial design phase of a parafoil, this information could be used to approximate the required fabric breaking strength of the panel.

Next, the first principal stress field S_1 acting on the centre rib obtained by the FE model is visualised in Figure 4.21. As expected, the highest stress peaks occur at A-LAP and B-LAP, where most of the aerodynamic pressure acts on the top side panel. The rib serves as a load transferring part by funnelling all forces into the bridle system. Also, the concentrated load at each LAP motivates the introduction of local reinforcements to avoid fabric tearing and deformations, which may change the rib profile shape (see Chapter 5). Table 4.4 summarises the load distribution of all four LAPs, and it can be seen that the B-LAP carries more than 50% of the total force acting on the rib structure. In common parafoils, the A-LAP usually carries most of the load while the load gradually decreases from LAP to LAP towards the trailing edge [111].

Table 4.4: LAP load distribution in centre rib.

LAP	A	B	C	D
Load distribution [%]	26	55	15	4

4.4.6. Tether Length Influence

The drag penalty of an airborne wind energy system due to the tether plays a vital role during system design. In this section, the analytical tether drag expression based on Equation 2.13 is compared to the tether drag obtained by the numerical simulation. First, the parafoil was simulated without any attached tether to determine the canopy lift and drag. Then the simulation was rerun with a tether of up to 1000m. The coupling convergence criterion had to be reduced to $1 \cdot 10^{-4}$ in order to obtain satisfactory results in the kite's position, and with the explicit coupling, a static position was found after approximately 12-15 coupling iterations. For the analytical expression, two approaches were tested. First, the influence of inclination angle on the tether was fixed to 90 degrees, called the simple approach. The second approach used the following expression for the angle of inclination

$$\Theta = \alpha_0 + \pi - \arctan\left(\frac{C_L}{C_D}\right), \tag{4.6}$$

where C_L and C_D correspond to the parafoil's aerodynamic coefficients. Figure 4.22 depicts four graphs illustrating the tether length influence on various aerodynamic parameters. Figure 4.22a shows the lift coefficient and local angle of attack at the centre rib for the range of tether lengths. It can be seen that the lift coefficient is decreasing by approximately 1.2% while the angle of attack stays almost constant for the whole range of tether lengths. It was mentioned in Chapter 2 that a kite system in force equilibrium flies

(a) Lift coefficient and change in angle of attack with respect to parafoil without tether.

(b) Analytical and simulated drag coefficient.

(c) Glide ratio.

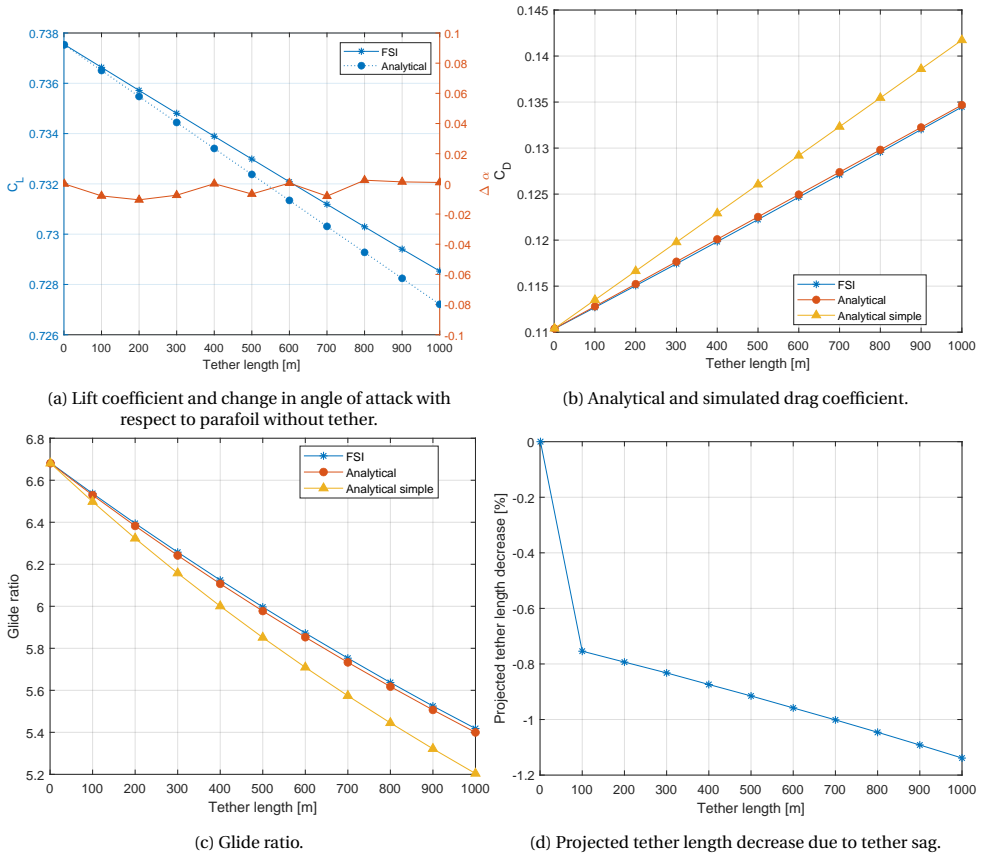(d) Projected tether length decrease due to tether sag.

Figure 4.22: Aerodynamic coefficients and projected tether length decrease for various tether lengths.

at a constant trim angle of attack, which is independent of the tether length as long as the kite's weight is small compared to the lift forces. The numerical simulation confirms this behaviour, and the decrease in lift coefficient can be attributed to the aerodynamic tether force acting towards the ground station due to tether sag. The analytical expression follows a similar trend as the numerical solution with a variation of 1.8% between both solutions.

Figure 4.22b depicts the drag coefficient of combined parafoil and tether. The tether drag coefficient of the numerical simulation was determined by the difference of tether forces in flow direction acting below the control pod and at the ground station. It can be seen that the simulation results in a lower drag compared to the simple analytical model (17% lower at maximum tether length) and matches well with the analytical model, which incorporates the expression in Equation 4.6. Figure 4.22c depicts the system glide ratio. The numerical result is slightly higher than the analytical expression due to a lower lift coefficient, and simple expression results in a 4% lower glide ratio. Finally, the projected tether length reduction due to tether sag is depicted in Figure 4.22d. It can be seen that

for a 1km tether length, the projected length is only reduced by 1.1%, which includes strain (approximately 0.4%) and tether sag concerning the flow direction. Overall, the analytical expression results in a good approximation of tether drag compared to the numerical solution. Utilising the analytical expression requires only a single run of the FSI simulation for a given geometry and wind speed.

4.4.7. CONCLUSIONS

It can be concluded that the developed coupling method can successfully determine the static flight state. The following findings can be summarised:

- The explicit coupling method without initial relaxation is the fastest method to converge on the studied wing geometry.

- No initial relaxation factor was found to converge the coupling using the Aitken method successfully.

- The IQN-ILS method with a QR1 filter and a limit of $1 \cdot 10^{-1}$ performed slightly worse than the explicit coupling. The initial relaxation factor significantly influenced the convergence behaviour, and no factor was found to result in a stable coupling for all cases.

- During the mesh sensitivity study, it was shown that a refined mesh resolution could result in local surface irregularities. The panel method reacted to local kinks by a pressure drop, and in return, the finite element solver would react with more significant deformations.

- The CPU time of the coupling method is mainly caused by the finite element solver for smaller mesh sizes and reduced when the parafoil approaches force equilibrium. The panel method's CPU time for refined mesh resolutions became significantly longer and stayed constant during coupling.

- Larger V_a caused an increase in lift and drag due to changes in profile geometry and an increased angle of attack.

- The panel method can predict similar lift and drag coefficients compared to a RANSE simulation up to an angle of attack of approximately 15 degrees.

- The analytical panel stress formulation can be used for a rough estimation of maximum panel stress without the need for a coupled simulation.

- The analytical tether formulation provides a good approximation of the tether drag compared to a full FSI simulation.

4.5. VALIDATION: 120M^2 SKYSAILS POWER PARAFOIL

In this section, a validation with actual flight data is presented. Two cases were simulated: a cross-wind flight and a neutral flight when the kite was placed passively in the air without any steering input. The data obtained during 154 power cycles and a 70 seconds neutral flight consisted of measuring tether and steering belt forces, orientation angles of the control pod and tow point at the ground station, apparent wind speed at the pod and a wind speed distribution from ground to flight altitude using a LIDAR system. All data shown here has been normalised as requested by SkySails Power. The coupling model was set up similarly to the previous section, where the symmetry boundary along the centre rib was exploited. During the neutral flight, V_a was low compared to cross-wind motion, and therefore gravity and the tether were both included in the finite element model. The parafoil geometry is based on a SkySails Power kite design with a (flat) surface area of 120m^2. The structure model built from the real geometry includes local reinforcements in each rib modelled with line elements. Material parameters of fabric and bridles were either given by the manufacturer or measured in the lab. Also, the two intakes at the leading edge were closed and their aerodynamic influence was disregarded in the model because of their small size. An important discrepancy between the model
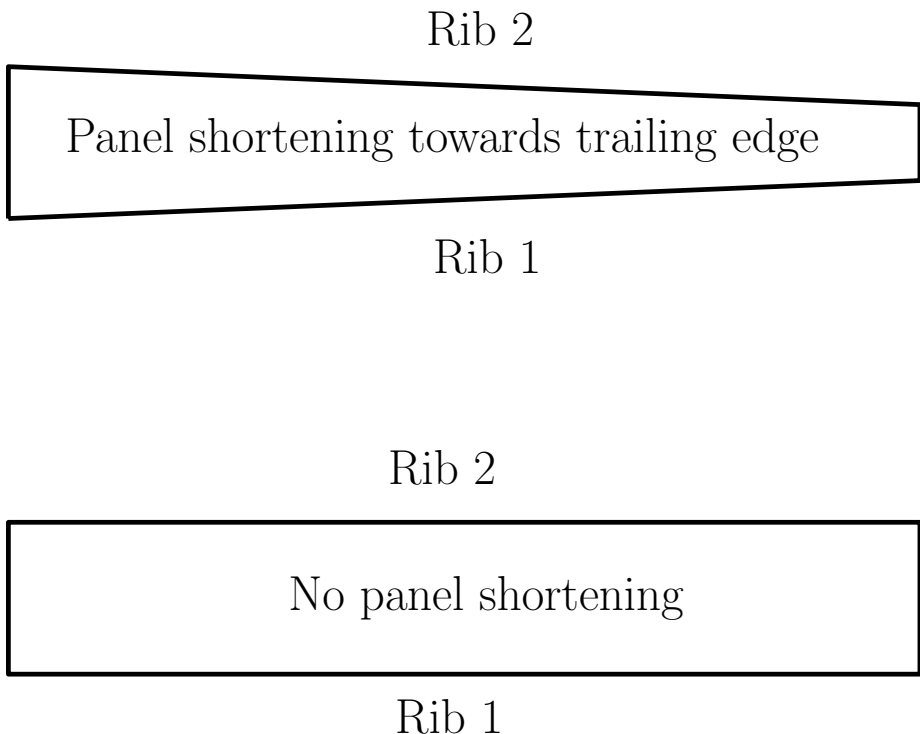

Figure 4.23: Illustration of panel shortening. The bottom panel shows a panel connecting two ribs without shortening, such that the rib-to-rib distance stays constant. The top panel has a linearly varying panel shortening towards the trailing edge.

and the real parafoil is the model's absence of geometric skin tension in some panels. Figure 4.23 illustrates two panels each connecting two ribs. The bottom panel has a constant rib-to-rib distance, and both ribs are parallel to each other, but the top panel has a linearly varying panel width such that both ribs are not parallel anymore. Parafoils often have this panel shortening to increase the tension at specific panel locations, e.g. the trailing edge, to enforce a planform shape or ballooning effect. The Skysails parafoil has several shortened panels of approximately 3-4% at the trailing edge. This shortening avoids a slack trailing edge during low speeds at which a dynamic pumping behaviour of the wing may occur such that the parafoil deforms spanwise like an accordion. Adding this feature into the three-dimensional finite element mesh caused significant difficulties and was therefore omitted. By ignoring the panel shortening in the FEM model, the profile orientation with respect to the flow is slightly different compared to the real kite. Also, the planform is slightly shorter at the trailing edge than the FEM model. Despite the differences, the panel shortening was not introduced because the parafoil was mostly studied at higher wind speeds such that the tension in the span-wise direction is sufficiently high. Also, a panel shortening of 3-4% does not change the planform geometry considerably. Nevertheless, a comparison between both models should be done in the future to validate the model assumptions.
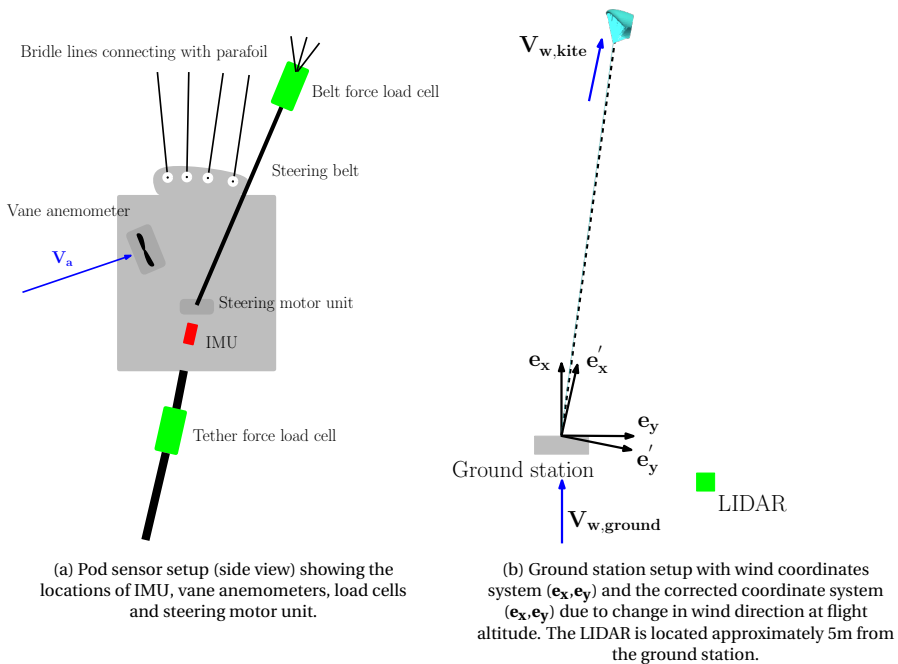
4

(a) Pod sensor setup (side view) showing the locations of IMU, vane anemometers, load cells and steering motor unit.

(b) Ground station setup with wind coordinates system ($\mathbf{e_x}$,$\mathbf{e_y}$) and the corrected coordinate system ($\mathbf{e_x'}$,$\mathbf{e_y'}$) due to change in wind direction at flight altitude. The LIDAR is located approximately 5m from the ground station.

Figure 4.24: Sensor setup at the ground station and control pod.

4.5.1. DATA MEASUREMENT SETUP
All measurement instruments used for the validation are listed in more detail, including the introduced uncertainties. The sensor setup is similar to the system found in Erhard 2018 [112].

FORCE MEASUREMENTS
There were three load cells to measure the tension force on the kite system during the flight. One cell measured the tether force below the control pod, and the other two instruments were connected to the steering belt, each at the end of the belt, to measure the steering force, see Figure 4.24a. All force measurements were done in a 10Hz frequency and were synchronised during the flight. The instruments were calibrated before the flight using a tension test machine, proving reliable over many flight hours.

WIND SPEED MEASUREMENTS
Two vane anemometers were attached to the sides of the control pod, measuring the apparent wind speed the parafoil experienced as depicted in Figure 4.24a. Their orientation was fixed for the pod frame, and therefore they only measured a projection of the wind speed vector. The vane's orientation was aligned with the kite's roll axis such that the measured wind speed has to be transformed in order to determine its magnitude during steady flight using

$$V_a^{\text{magnitude}} = V_a^{\text{measured}} \sqrt{\frac{1 + E^2}{E^2}}, \tag{4.7}$$

where E corresponds to the parafoil's glide ratio. In case of changes in the angle of attack, which may occur during the retraction phase and turning manoeuvres, the magnitude of V_a deviates because the transformation equation is used with a constant glide ratio. In order to reduce the data points in phases when a deviation in the angle of attack occurred, only the power and transfer phases are considered for validation when no steering input was given during flight. The manufacturer calibrated the vane anemometers, and before the flight, a new set of propellers was attached. A clear disadvantage of this measuring approach is the absence of measuring the angle of attack and the magnitude of V_a directly. Also, the control pod may influence the airflow around the vane anemometers, causing a deviation from measured and actual wind speed. Based on the possible influence of the control pod and the error due to wind speed transformation, uncertainty remains in determining V_a during flight.

Figure 4.24b shows the LIDAR system (acronym for Light Imaging, Detection And Ranging) located next to the ground station which measured wind speed and direction at various altitudes in a cone-shaped volume above the ground station. The instrument sends a LASER signal in four directions towards the sky and with back scatter from aerosols in the air it determines both magnitude and wind direction over a range of altitudes. With a sample rate of 1 Hz it is not able to detect all gusts occurring in the atmospheric layer above the ground station. The wind speed direction could be used to optimise the power and retraction phases during operation, and with the known kite's location in space, the wind speed could be extrapolated in time to the kite's current position. Another method to estimate the wind speed at the kite's location was done applying

an Extended Kalman Filter technique which uses the kinematic model derived in Erhard et al. [29] and sensor data from both pod and ground station, similar to the approach explained in Schmidt et al. [91]. With the approximated wind speed magnitude and direction at the kite's location the offset angle between wind at the ground and at flight altitude could be determined and corrected as shown in Figure 4.24b. The wind direction correction provide an improved estimate of the glide ratio using Equation 2.1 which utilises the wind speed at flight altitude. Additionally, a thermometer and barometer provided temperature and air pressure measurements at ground level, which were used to determine the air density using the ideal gas law.

Elevation and Pod Orientation Angles
The tow point at the ground station measured both ϑ and ϕ angles as well as tether length such that the location of the kite could be determined during the power phase when tether sag is slight. The control pod was equipped with an inertial measurement unit (IMU) which measured accelerations in three axes such that both orientation and turn rates of the kite system were determined. Also, the angle between the tether and control pod could be measured, which is used to improve the elevation angle approximation.

Data filtering
The following data filtering and selection procedures were applied to the raw data recorded during flight:

- The data was smoothed with three seconds moving average to level out short-term fluctuations using the Matlab function *movmean*. The three seconds were chosen because it provided data with less noise and still displayed the relevant kite dynamics. A shorter time averaging provided data with higher variance but similar mean values for the aerodynamic parameters determined in this section.

- The symmetry assumption of the parafoil was enforced by selecting only data points during the straight flight when the steering belt position was not further than 5cm from the neutral position in both directions.

- To enforce the quasi-static flight assumption, the magnitude of measured acceleration during the flight was used to select data points which satisfied a 10% offset of earth's acceleration.

4.5.2. FSI Convergence
The SkySails Power parafoil behaved differently during the coupling procedure compared to the parafoil geometry in the previous section. The explicit coupling scheme did not converge when simulating the power phase for various wind speeds. Even applying a constant damping factor between two consecutive iterations did not improve the behaviour and always resulted in divergence. Figure 4.25a depicts the C_L progression during coupling for a range of V_a using the IQN-ILS implicit coupling scheme, and it can be seen that after a few periods of damped oscillations the kite systems converges to a stable state. In all cases, the QR1 filter with a limit of 10^{-1} resulted in convergence while lower limits would diverge. The choice of the initial relaxation factor η_0 was more

arbitrary. Values for η_0 between 0.3 and 0.7 would often result in convergence, but there were cases when a slight change in η_0 (e.g. from 0.3 to 0.4) would result in divergence. Therefore, a range of simulations was run parallel using initial relaxation factors between 0.3 to 0.7 in steps of 0.1, and at least one combination converged.

In Figure 4.25b the convergence behaviour of the glide ratio for the neutral flight condition using explicit coupling can be seen. The progression exhibits damped oscillatory behaviour, which converges to a stable state after approximately 60 iterations, and it can be concluded that higher velocities result in more coupling iterations due to the increased influence of structural deformations.

(a) Lift coefficient for various V_a using IQN-ILS coupling.

(b) Glide ratio using explicit coupling for neutral flight.
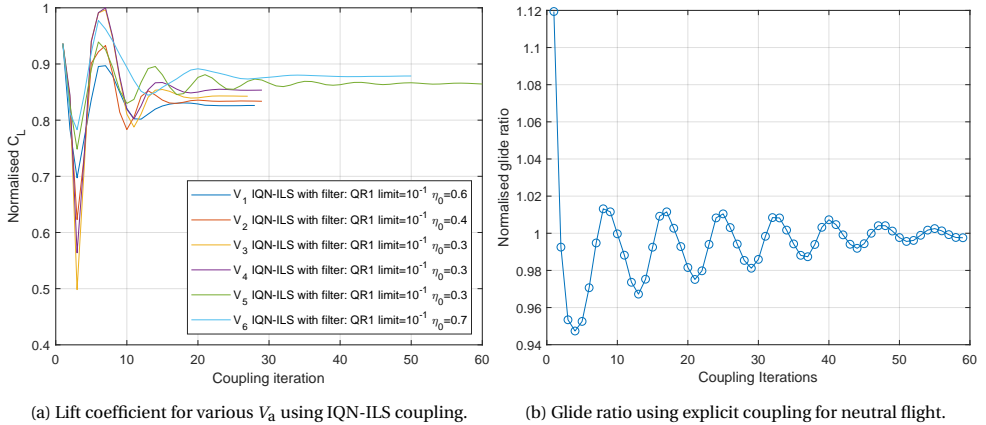
Figure 4.25: Convergence of normalised aerodynamic parameters during cross-wind and neutral flight.

During the course of this work a mesh sensitivity study was done on the SkySails Power parafoil and it was observed that for a finer mesh density with 80 nodes along the profile or higher all coupling methods would diverge. No set of filter parameters was found to alleviate the divergent behaviour. Figure 4.26a until 4.27d depict the deformed kite during the coupling procedure for a range of iterations. It can be seen that after the second coupling iteration the rear of the parafoil begins to bend downward forming a bulge along the span close to the trailing edge. The bulge effectively increases the wing profile's curvature which causes the parafoil to pitch up as can be seen in iteration 4 and 5. Due to the increased angle of attack the parafoil reacts by pitching down and moving forward in iteration 6, and a lower pressure field around the rear bulge starts to develop. Iterations 7 to 9 show how the pressure at the bulge decreases even further causing the whole canopy to drastically deform which eventually leads to flipping the kite upside down. This divergent behaviour is caused by the flexible canopy reacting to the nonphysical attached flow field computed by *APAME*. Potential flow is not able to model flow detachment which would otherwise occur at the rear of a wing especially for drastic changes in profile curvature like in iteration 7 to 9. Therefore, the aero-elastic coupling results in a positive feedback of canopy deformation and pressure acting on the bulge. Attaching additional bridle lines to the trailing edge or increasing the panel stiffness close to the trailing edge did not improve the divergent behaviour, and the only remedy found was to coarsen the mesh at the trailing edge.
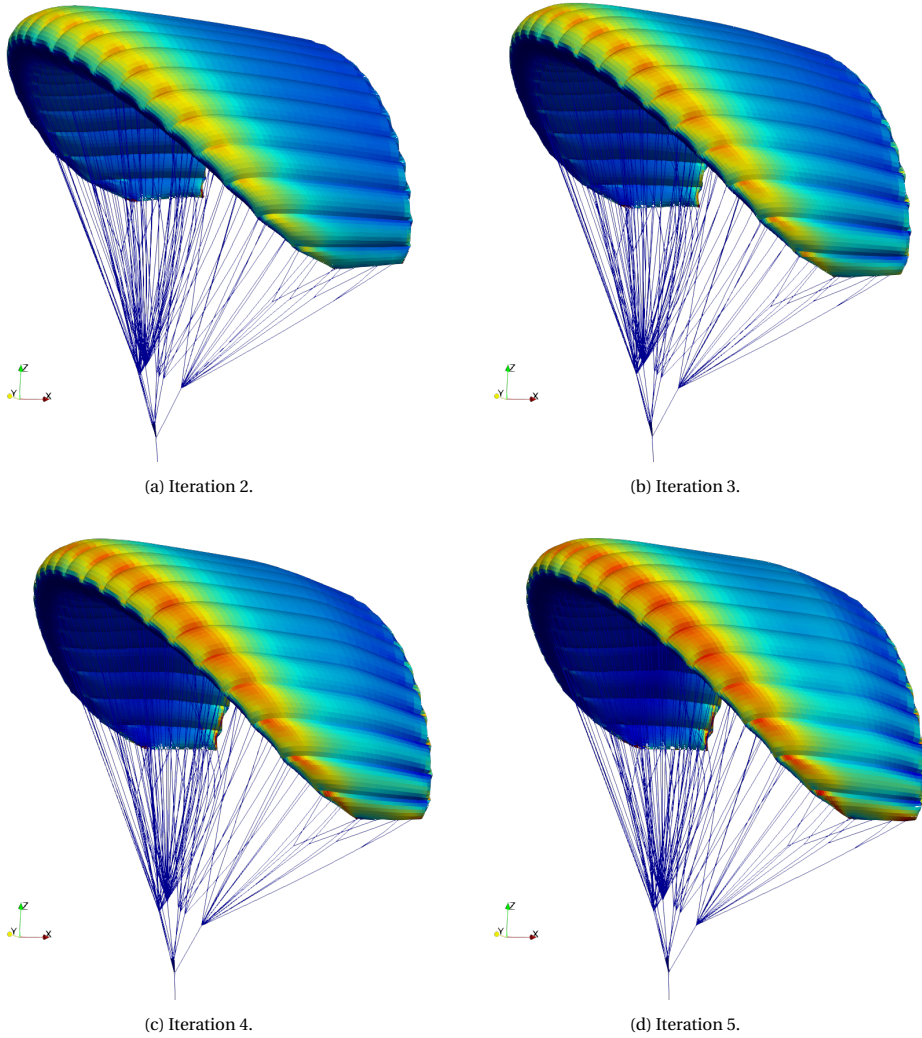
(a) Iteration 2.

(b) Iteration 3.

(c) Iteration 4.

(d) Iteration 5.

Figure 4.26: FSI divergence with explicit coupling on fine mesh density (iterations 2-5).

4.5.3. Tether and Steering Forces

The first model validation was done on the tether and steering forces measured during flight. The data is presented for different flight phases based on the studied aerodynamic parameter. The power phase mainly consisted of larger flight velocities, and therefore the transfer phase is added to the graphs to show force measurements for lower flight velocities. Figure 4.28 depicts the tether forces plotted against the belt force during all flight phases when no steering input was given. The resulting graphs clearly exhibit a linear trend with a coefficient of determination close to 1 using linear regression. The

(a) Iteration 6.

(b) Iteration 7.

(c) Iteration 8.
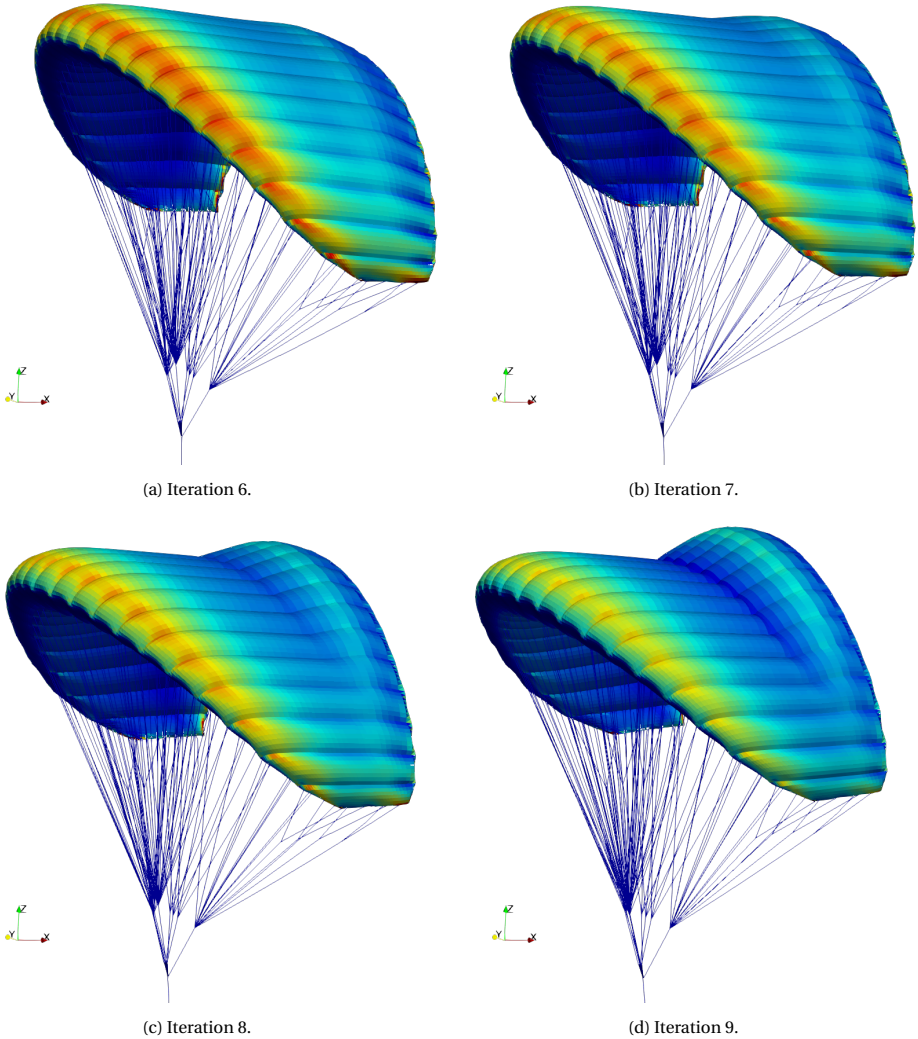
(d) Iteration 9.

Figure 4.27: FSI divergence with explicit coupling on fine mesh density (iterations 6-9).

FSI results match well with the linear regression, and an offset between the data points and the simulation can be seen for larger forces where the relative increase in belt force is more significant than the increment in tether force. This behaviour could result from a local increase in angle of attack at the tip section of the wing due to deformation.

Next, the tether force as a function of apparent wind speed V_a is examined. Figure 4.29a and 4.29b depict the measured data and simulation results for power phase and the combination of power and transfer phases, respectively. The data follows a quadratic trend with a coefficient of determination close to 1 using a quadratic fit with the intercept at
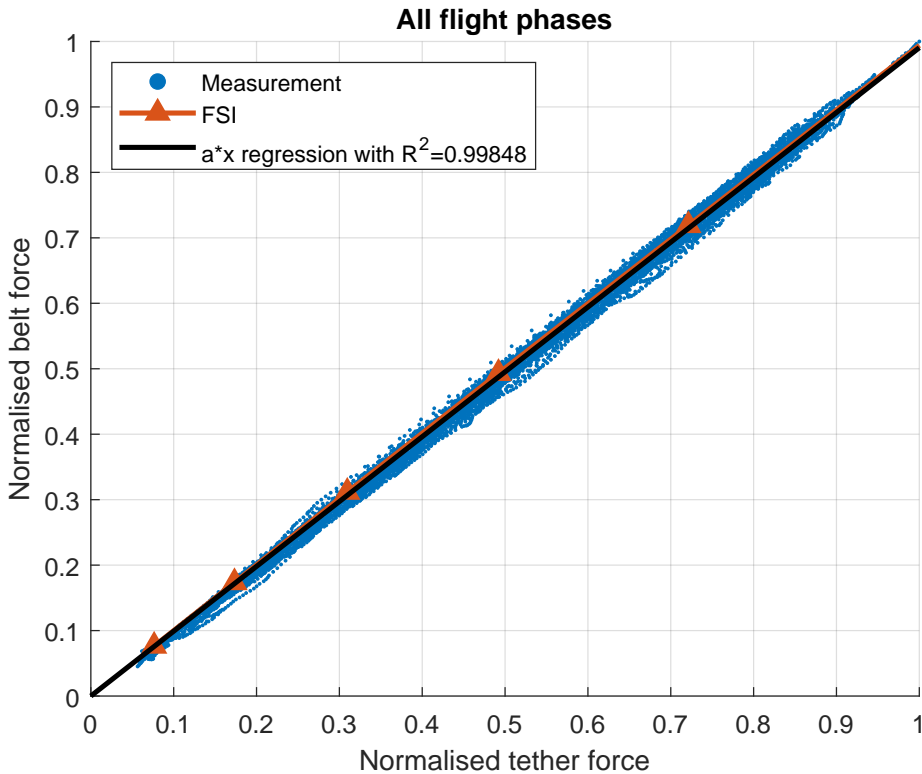
Figure 4.28: Normalised tether force against normalised belt force obtained during a total of 154 power cycles recorded during all flight phases. The measurements are smoothed with a 3 seconds moving average and only data points without steering input are shown here.

V_a=0. The spread in data is more prominent for lower values of V_a recorded during the transfer phase compared to the power phase. Two simulation results are compared to the measurement: the FSI solution without and with maximum tether length, and a minimal variation between the two simulations can be seen here. Also, the simulation results closely follow the quadratic regression except for larger values of V_a where the FSI results deviate from the regression towards larger forces.

Additionally, the number of recorded data points during flight for both graphs are shown in Figure 4.30a and 4.30b in shape of a histogram. It can be seen that the data points of V_a during the power phase varies between 80-90% of the maximum velocity recorded. During the flight a range of target velocities were flown which explains the spread in data. The retraction phase adds more data points between 40-80% of the maximum velocity.

In Figure 4.31a and 4.31b the belt force as a function of apparent wind speed V_a is shown for power and combined power and transfer phases, respectively. The quadratic regression also fits well with the data sets and the simulation results show good agreement with the regression except for larger values of V_a.
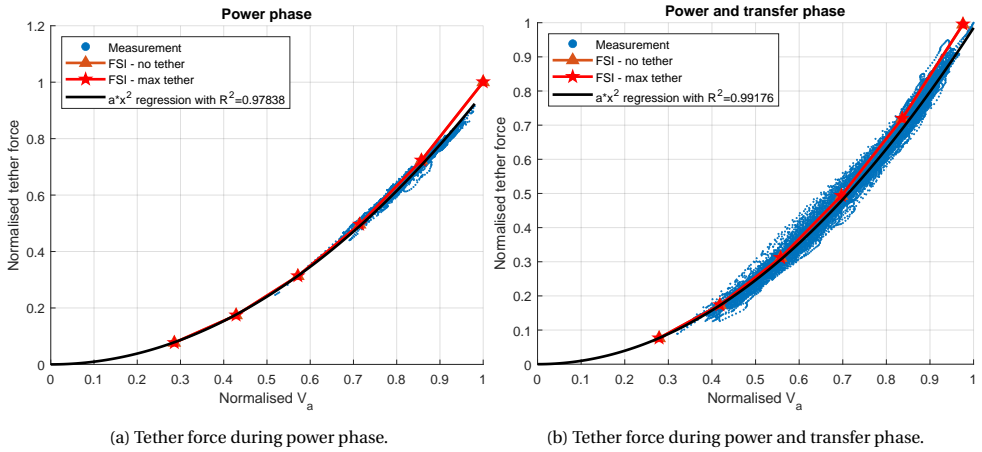
(a) Tether force during power phase.   (b) Tether force during power and transfer phase.

Figure 4.29: Normalised tether force against apparent wind speed obtained during a total of 154 power cycles for both power and transfer phase.
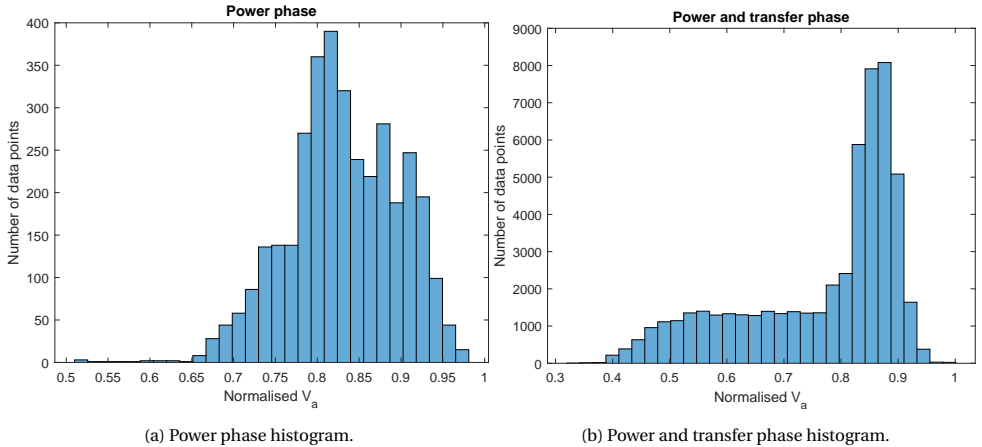

(a) Power phase histogram.   (b) Power and transfer phase histogram.

Figure 4.30: Normalised V_a histograms for power and transfer phase showing the distribution of data point collected during 154 power cycles.

4.5.4. FORCE COEFFICIENTS C_R AND C_B

With an overall good agreement between the regression and simulation results, the next step is to investigate the force coefficients in more detail. Figure 4.32 depicts the C_R normalised by the mean of all data points recorded during the power and transfer phase when no steering input was given. Each data point is plotted in colour representing its current tether length. It can be seen that a deviation from the mean is larger for lower apparent wind speeds when the tether force is small, and the kite is more susceptible to gusts and other unsteady external factors. For larger values of V_a the data exhibits a maximum deviation of 15% from the mean and the data exhibits an overall positive slope of C_R with increasing V_a. The observed change in C_R highlights the interesting feature

(a) Belt force during power phase

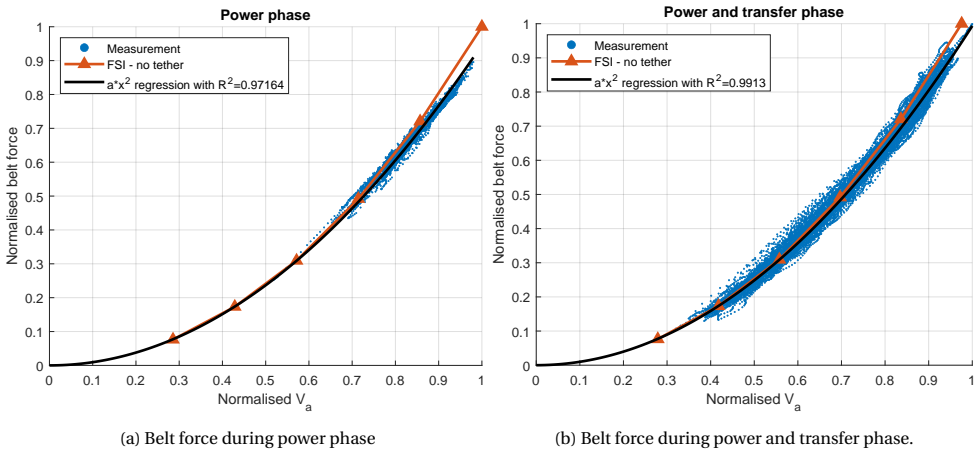(b) Belt force during power and transfer phase.

Figure 4.31: Normalised belt force recorded during 154 power and transfer cycles plotted against apparent wind speed V_a.

of the parafoil, which changed its flight performance for higher wind speeds. Possible reasons are an increase in the angle of attack due to deforming bridle lines, a change in rib profile, and a local change in a twist of the wing. The simulation results plotted in red lie approximately on the mean of the data points and exhibit a positive slope. No significant deviation between the simulation results using no tether and the maximum tether length on C_R can be seen.

To improve the visibility of the data points measured during the flight Figures 4.33a and 4.33b depict C_R in a histogram, where each tile represents the number of data points recorded for that specific range of C_R for a given range of V_a or tether length indicated by a colour map. Additionally, the binned mean of all tiles in a column is plotted as black crosses. With this representation a good agreement between simulation and binned means can be seen in Figure 4.33a except for low values of V_a. The resultant force coefficient is plotted against the tether length in Figure 4.33b, and it can be seen that the binned mean values and the simulation results with maximum V_a fit well for tether length above 0.8. C_R determined by the simulations appears to be slightly increased for longer tether lengths which are in accordance to the binned mean values of the measurements except for tether lengths lower than 0.6 where the measured C_R is increasing by almost 10%.

The resultant force coefficient is also compared to data points recorded during the power phase only. Figure 4.33c depicts the C_R against V_a and similar to the measurements including the transfer phase, the coefficient exhibits a positive slope for increasing V_a. The simulation results underestimate the binned mean values by approximately 5% where most data points were recorded. Similarly, Figure 4.33d shows the C_R plotted against the tether length, and the binned mean values display a slight decreasing slope which is the opposite trend compared to the transfer phase. The simulation results based on the maximum velocity slightly underestimates the binned mean values of the measurements.
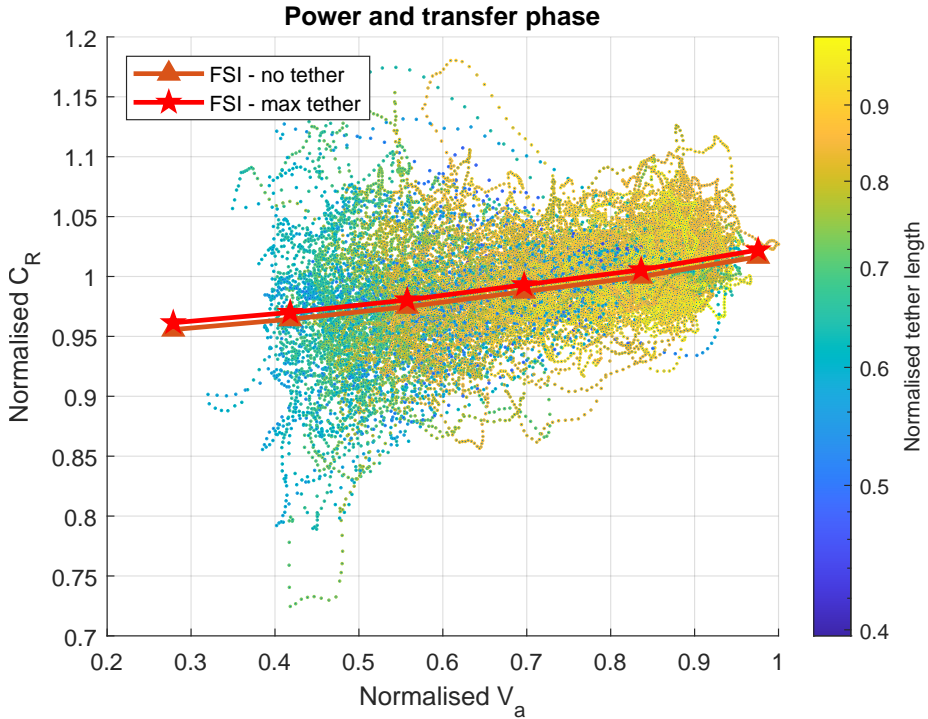
Figure 4.32: Resultant tether force coefficient C_R obtained during 154 power cycles.

Next, the belt force coefficient C_B is compared to the measurements. The coefficient is determined in the same manner as C_R by simply dividing the measured force by the dynamic pressure and the parafoil's projected area. Figure 4.34a and 4.34b depict the coefficient during power and transfer phase plotted against V_a and tether length, respectively. Both binned mean values of the measurements and simulation results exhibit a positive slope with increasing V_a and tether length. The simulation results lie within 5% of the binned mean, and the increasing trend for the force coefficient as a function of V_a has resembled as well.

Inspecting the power phase only as depicted in Figure 4.34c and 4.34d the data point density is lower but more concentrated around higher velocities. Again, the measured force coefficient and the simulation results show a good agreement except of the negative trend in the measured data in Figure 4.34c for values of Va between 0.8 and 0.95. The negative trend in the data is caused by a loss in lift forces at the wing tips. This loss could be the result of excessive profile deformations or local flow separation or a combination of both.

It can be concluded that the simulation results correctly reflect the increasing trend of the force coefficients with increasing velocity. Also, the data measurements do not show a clear trend in force coefficients with varying tether lengths. The discrepancy between measured and simulated force coefficients lies within 5%, satisfying for an initial design tool with an aerodynamic flow field obtained with potential flow theory. It should

(a) C_R against V_a.

(b) C_R against tether length.

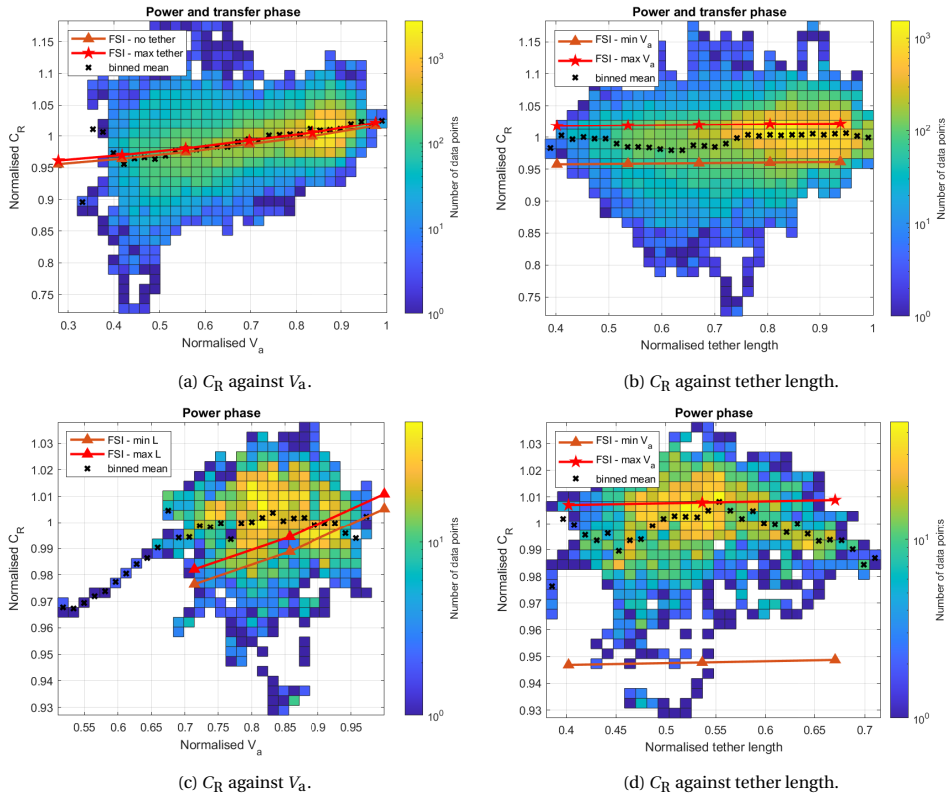(c) C_R against V_a.

(d) C_R against tether length.

Figure 4.33: Normalised tether force coefficient for various apparent wind speeds and tether lengths obtained during a total of 154 power cycles.

be noted that the spread in data points for various velocities and tether lengths clearly shows that the test setup is disturbed by the unsteady wind field and kite-tether dynamics, as well as possible changes in the angle of attack.

4.5.5. GLIDE RATIO

In this section, the system's glide ratio is determined using Equation 2.1 from measurements and compared with simulation results. Figure 4.35a and 4.35b depict the histogram of data points recorded during both power and transfer phase as a function of V_a and tether length, respectively. The glide ratio indicated by the binned mean values fluctuates between 0.9 and 1.15 over the range of velocities, especially in the mid-range, where the amount of data points is sparse, and the binned mean values should be interpreted with care. From the data points, it is not easy to interpret a clear increasing or decreasing trend due to V_a mostly because of the large spread in glide ratios occurring. A similar picture can be seen in Figure 4.35b where the binned glide ratio exhibits smaller fluctuations over the range of tether lengths, and a slight increase in glide ratio can be seen. This trend is opposite to the simulation results, which show a reduction in glide

(a) C_B against V_a.

(b) C_B against tether length.

(c) C_B against V_a.
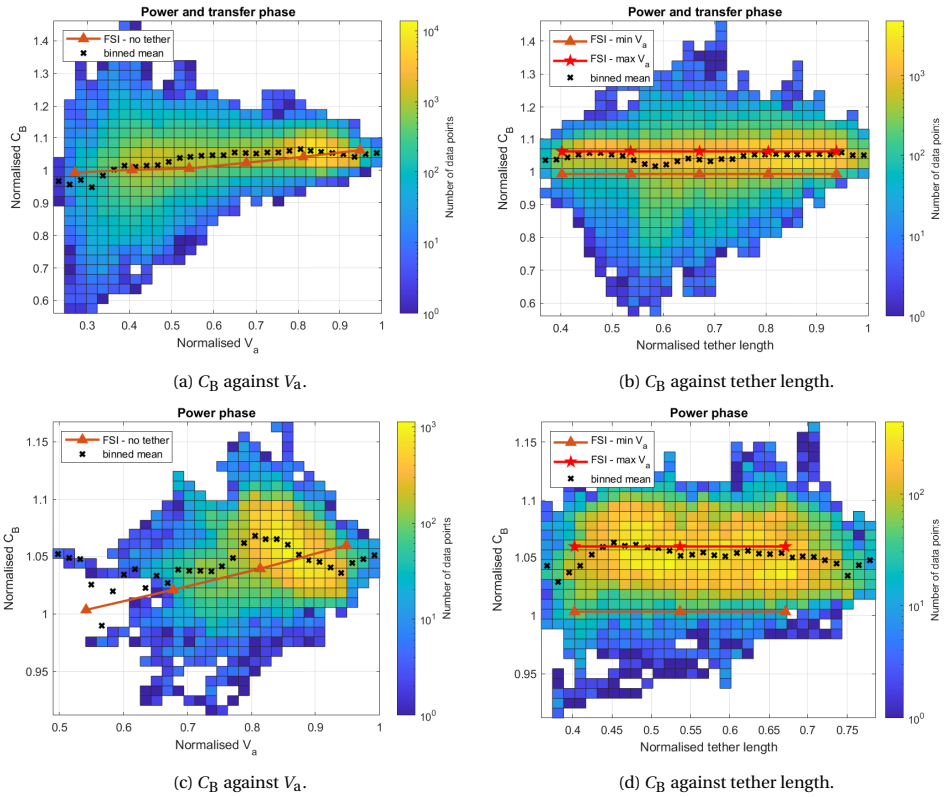
(d) C_B against tether length.

Figure 4.34: Normalised tether force coefficient against apparent wind speed obtained during a total of 154 power cycles.

ratio for a longer tether, and considering the verification done on the tether drag influence, this trend should be expected. For both graphs, the simulation results indicate an overestimation of the glide ratio by approximately 5-10%.

By inspecting the glide ratio solely measured during the power phase in Figure 4.35c and 4.35d a different behaviour can be observed. The glide ratio exhibits a negative trend for larger values in both figures. The difference between the binned mean and the simulation results varies between 5-12%. The overall overestimation of the glide ratio is expected due to the potential flow assumption, which overestimates lift at higher angles of attack, as could be seen in the comparison study with CFD results. Two factors possibly cause the large spread in glide ratio presented in this section. The first source of error lies in the model from which the glide ratio was computed (Equation 2.1). As stated in Chapter 2 the dynamic model assumes a perfectly stretched tether without sag and dynamic interaction between wind, kite and winch. Also, the model is based on a force equilibrium assumption that is not satisfied in a nonuniform wind environment and with a winch accelerating the kite during flight. The second source of uncertainties is the sensors used to determine the glide ratio. The LIDAR determines a wind speed average of

(a) Glide ratio against V_a.

(b) Glide ratio against tether length.

(c) Glide ratio against V_a.

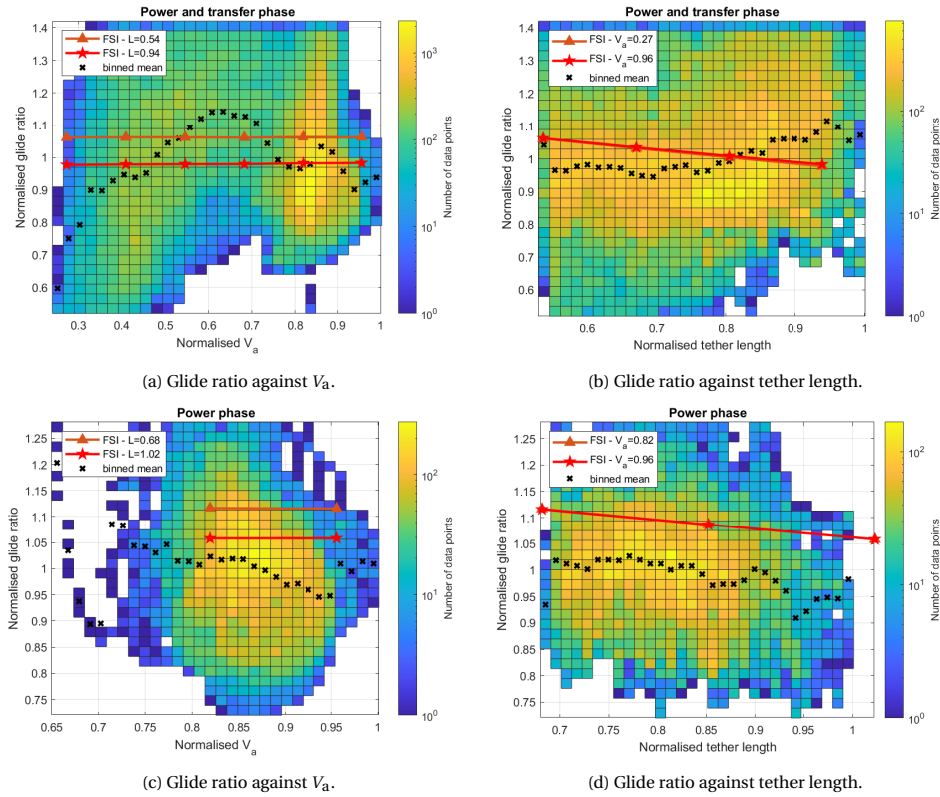(d) Glide ratio against tether length.

Figure 4.35: Normalised glide ratio during power phase.

over 1 minute and acts as a low pass filter. The tow point angle at the ground station measures ϑ to a high degree of accuracy, but due to the long tether, a time lag between forces acting on the kite and the angle measured at the ground station may occur.

4.5.6. NEUTRAL FLIGHT

The final model validation was done for a neutral flight during a time window of 5 minutes when the parafoil was positioned above the ground station such that the wind direction and tether were approximately aligned (zero azimuth). The kite was steered with small steering input to counteract gusts and turbulence to hold it in the same position. The simulation setup was done similarly as before: enforcing the symmetry boundary condition at the centre of the kite, thus modelling only half of the parafoil. Since the acting forces during a neutral flight are small compared to the power extraction phase, each component of the parafoil, such as fabric, bridle lines, control pod, and tether, were given the known weight values and the FE solver incorporated these into gravitational forces. For a kite in the neutral position, the apparent velocity is equivalent to the wind speed at flight altitude. Therefore, the measured LIDAR and ground wind speeds were taken as V_a at ground and flight altitude, while the values in between were linearly inter-
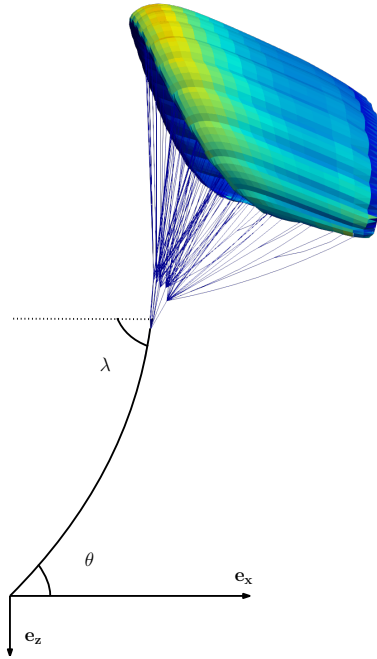
Figure 4.36: Schematics of elevation angles during neutral flight. The wind is aligned with $\mathbf{e_x}$.

polated. The converged result was then used to determine both elevation angles (θ, λ) below the control pod and at the ground station, as depicted in Figure 4.36.

The most relevant measurements during the 5 minute flight window are shown in Figure 4.37. Both angular rates of the tow point and the g-forces experienced by the control pod serve as a selection procedure for the data to ensure a steady flight. All data points with an angular rate deviation of 0.03 deg/s from zero and a g-force deviation larger than 0.01 were excluded. It can be seen in the azimuth angle that the kite was drifting during the 5 minutes of flight, and for the validation, only data points within -5 to 5 degrees azimuth were considered. The tow point elevation angle was measured with two rotary encoders, and the pod elevation was measured using the IMU data. Here, the difference operator Δ refers to the difference between the FSI result and measured value.

Figure 4.38a and 4.38b depict the difference in the measured elevation angle from the simulation at both ground station (tow point) and control pod, respectively. It can be seen that the number of data points is sparse due to the short flight window and data selection criterion. For the pod elevation angle, the difference between measurement and simulation stays within ±1 degree, while the difference for the pod elevation is approximately within ±2 degrees. The simulation results of the kite-tether system show that the developed method can approximate both elevation angles to a satisfying degree of accuracy. The measured data also shows how complex the interpretation of the kite system in a real wind environment is. Next to fluctuations in the wind field, dynamic interactions between kite and tether create a time delay between measured accelerations
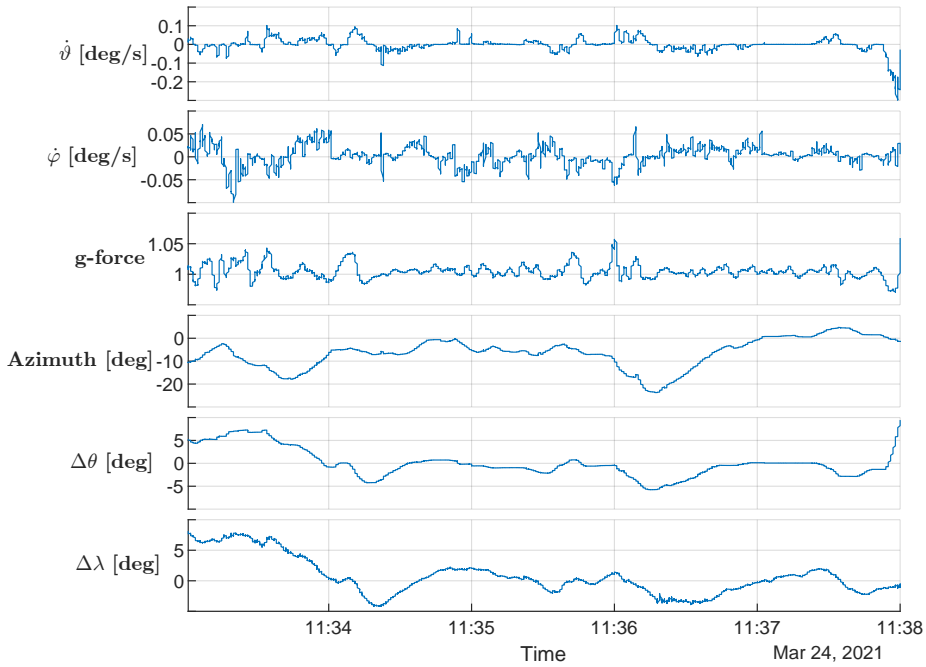
Figure 4.37: Measurements taken during neutral flight.

(a) Tow point elevation angle θ.
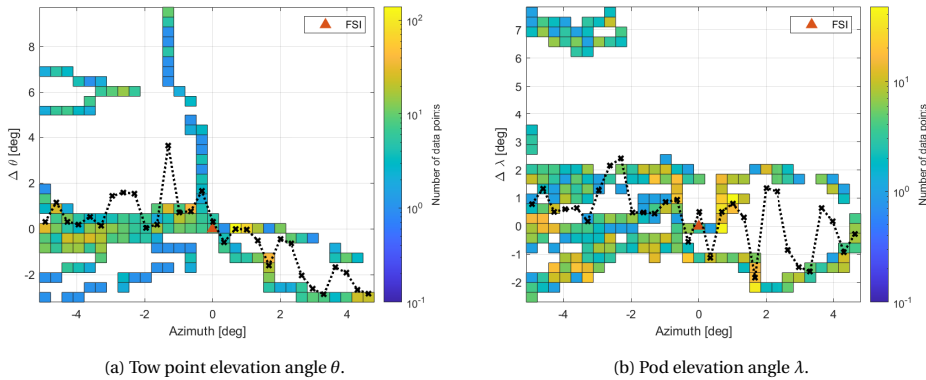
(b) Pod elevation angle λ.

Figure 4.38: Elevation angles at ground station and pod during neutral flight for various azimuth angles. The data is presented as the difference between measurements and simulated value.

at the kite and the ground station. Also, despite the pilot's effort to keep the kite aligned with the wind vector, the kite tends to drift slightly off, possible due to changing wind direction at flight altitude.

4.5.7. CONCLUSIONS

In this section, the developed numerical method was applied to a SkySails Power kite geometry, and key aerodynamic parameters were compared with measurements recorded during 154 power cycles and a 5 minutes neutral flight. It was shown that determining the resultant force coefficient C_R and glide ratio from measurements is not trivial due to many uncertainties occurring during the flight. To conclude the validation section of this work is can be stated that the developed numerical parafoil model is capable of estimating tether and belt forces and a glide ratio for a tethered wing to a satisfying degree of accuracy. The following highlights identified in this section are:

- Both tether and belt force follows a quadratic trend dependent on V_a and the numerical simulation results are in good agreement with the quadratic fit.

- The numerical simulation and measured resultant force coefficient C_R both exhibit a positive slope for increasing V_a and both match well.

- The C_R as a function of tether length is constant in both simulation and measurements.

- The belt force coefficient C_B exhibits a similar trend for both V_a and tether length compared to C_R. The numerical solution matches well until large values of V_a.

- The glide ratio determined by the measurements and the numerical simulation shows an offset of 5-15% (overestimation by the FSI) depending on the velocity and tether length. The data spread is substantial due to the apparent wind speed sensor, the time lag between pod and ground station, and the model assumptions used to determine the glide ratio.

- The measured elevation angles during neutral flight fit within 1-2 degrees of accuracy compared to the FSI simulation.

5

MULTI-DISCIPLINARY DESIGN OPTIMISATION

This chapter summarises the publication Thedens et al. [113] published in 2018, which presents a multidisciplinary design optimisation (MDO) to assess the influence of fabric orientation, reinforcement layout, and aerofoil shape on aerodynamic performance and rib deformation of a ram-air kite. The aim is to find an optimum rib profile as well as material orientation and reinforcement layout that maximise the power harvesting factor and, at the same time, reduce strain energy in the rib. The optimisation utilises an FSI routine, which is run in a staggered scheme until equilibrium. A simplified two-dimensional model is developed to avoid the extensive computations required for high-fidelity soft-kite simulations. The model considers a single rib loaded with a two-dimensional aerodynamic pressure field obtained by a viscous-inviscid interaction method. Aerodynamic effects caused by the inlets at the leading edge, fabric porosity and cross-ports in the rib are neglected.

The chapter is organised in the following manner. First, the two-dimensional rib model is introduced. Then, both structure and aerodynamic design parametrisations are shown, and finally, the MDO results obtained by an uncoupled and coupled (FSI) analysis are depicted and discussed.

5.1. RAM-AIR KITE MODEL
Based on the results stated in Chapter 4 the load acting on a ram-air kite rib depends on both aerodynamic pressure and geometrical layout of the kite, specifically anhedral, which influences span-wise acting load. Nevertheless, an MDO incorporating a full three-dimensional kite model is beyond the scope of this study, and therefore a simplified model is derived, which can be utilised to study qualitative design choices in rib profile shape and reinforcement layout. The simplified model consists of a single rib connected to a fixed trim point via four bridle lines. The induced drag is added to the total drag formulation to account for three-dimensional aerodynamic effects, which shall steer the

aerodynamic analysis towards a more realistic glide ratio. For details refer to Thedens et al. [113].

5.1.1. Structure Model

The rib deformations are determined with a static nonlinear finite element solver using 3-node triangular finite elements and 2-node bridle line elements derived in Chapter 3. The reinforcements modelled with line elements are superimposed on the membrane mesh [114] as depicted in Figure 5.1b which simplifies the meshing procedure in the case when reinforcements are crossing each other. The structure model consists of a single elastic rib with reinforcements starting at each line attachment point (LAP) and bridle lines that connect each LAP and the bridle point where all bridles connect to a single point. The static solver is based on the following equation

$$[\mathbf{K}(\mathbf{u})]\mathbf{u} = \mathbf{f}(\mathbf{u}), \tag{5.1}$$

where $\mathbf{K}$ is the structure's tangent stiffness matrix, $\mathbf{u}$ is the deformation vector, and $\mathbf{f}$ is the external force vector. The system of equation is solved iteratively with the *Newton-Raphson* method to obtain the displacement field of the loaded rib. The tangent stiffness matrix consists of stiffness contributions of all three members, i.e. membranes, reinforcements, and bridle lines

$$[\mathbf{K}] = [\mathbf{K}]_{\text{membrane}} + [\mathbf{K}]_{\text{reinforcements}} + [\mathbf{K}]_{\text{bridles}}. \tag{5.2}$$

It should be noted that no wrinkling model is used for the membrane elements within the multidisciplinary design optimisation because of convergence problems that occurred during the FEM solving process. The implications of the absence of a wrinkling model is a stiffness overestimation in areas of compression which occur at the bottom side between LAPs.

5.1.2. Aerodynamic Model

The flow around aerofoils of ram-air kites combines several multi-scale phenomena. On the pressure side, bridle attachment points create surface irregularities over which the flow may separate and eventually reattach. Shape irregularities are softer on the suction side, but dynamic compliance mechanisms can affect boundary layer transition in non-linear ways [115]. Furthermore, ram-air kites are made of woven fabrics whose surface is neither perfectly impermeable nor hydrodynamically smooth. While direct numerical simulation (DNS) of clean aerofoil flows is sometimes feasible [116], the DNS solution of FSI problems at relatively high Reynolds number remains entirely out of reach [117]. This is especially true for conceptual design and optimisation purposes [118, 119].

Following current practice in the aerofoil design community [120], the flow is solved with a viscous-inviscid interaction (VII) method [121]. Rfoil is a VII code derived from Xfoil [122]. It couples a panel method for the potential far-field flow with an integral method for the boundary layer flow of the near-field. Flow regions are tightly coupled through the Lighthill interaction law [123], and the two codes (Rfoil and Xfoil) differ in their handling of turbulent and transitional boundary layers [124, 125].

The turbulent boundary layer formulation of Rfoil was strengthened over the years to perform well in high-Reynolds number cases[124, 125] that include local perturbations like those caused by active flow control [126]. In this work, Rfoil's turbulent boundary layer formulation is further enhanced to deal better with the peculiarities of ram-air kite aerofoils:

- Separation and reattachment near line attachment points were handled by further improving the numerical implementation details. The main modifications consisted in refining the spatial discretisation of kinks, correcting closure relation inconsistencies for low shape factors (H<1.2) that occur upstream of boundary layer kinks, and increasing iteration count.

- Surface roughness of kite fabrics was handled by correcting the turbulent skin-friction correlation according to the recommendations of Betterman [127] through the procedure outlined by Tani [128].

In terms of workflow, Rfoil receives geometry and non-dimensional flow parameters as inputs and computes pressure distributions or force coefficients for one or more angles of attack. Higher-level execution is controlled through Python to run Rfoil and the structural solver in batch mode. This approach has proven robust enough for optimisation, even when including a fluid-structure interaction routine that requires several Rfoil runs inside an iterative loop.

The pressure acting on a single kite cell is integrated over the cell width to obtain a simplified two-dimensional aerodynamic load on the rib. The rib in a ram-air kite is loaded due to pressure forces consisting of external aerodynamic and internal ram pressure acting on the canopy. The external pressure is obtained with Rfoil, whereas the internal pressure is assumed to be at stagnation pressure.

Kites with AWE application produce maximum power during cross-wind flight with a specific wing configuration, maximising the power harvesting factor ζ. The power harvesting factor is chosen as the performance metric in the optimisation and is to be maximised for a deformed profile. Unlike rigid aircraft, which can be constantly trimmed by changing the elevator angle on the horizontal stabiliser, soft kites have a fixed trim. The trimming is done by positioning the trim point along the neutral line where the aerodynamic pitching moment is zero. Since the kite deforms during operation, this neutral line is not known a priory and is usually found experimentally. To ensure a moment equilibrium at all stages during the optimisation, the rib is trimmed in each FSI iteration by moving the bridle point along the chord to the neutral line while keeping the bridle length constant in the y-direction. The optimal angle of attack α^* in each FSI iteration, which maximises ζ_{max} is

$$\alpha^* = \operatorname*{argmax}_{\alpha} \frac{4}{27} C_R(\alpha)(1 + E(\alpha)^2). \tag{5.3}$$

5.1.3. FLUID-STRUCTURE INTERACTION

The strong coupling between the deforming profile and the aerodynamic flow is part of the analysis. Structural deformations in the rib will induce changes in the pressure field,

which will, in return, induce a new deformation field. The change in rib shape changes the flow field, and the elongation of the bridles, which increases the relative angle of attack, are considered. With every change in design variables, the FSI is run to determine the objective function in a steady and deformed configuration. The FSI convergence criterion is measured with the relative error in elastic energy ϵ, and convergence is achieved when the error is below 1×10^{-5}. The relative error in elastic energy is computed as

$$\epsilon = \frac{W_c^n - W_c^{n-1}}{W_c^{n-1}}, \tag{5.4}$$

with n being the iteration number and W_c the complementary energy expression. A pressure distribution determined by Rfoil for the angle of attack, which maximises the power harvesting factor, is used to deform the rib structure. In return, the deformed rib profile is fed back to Rfoil to determine a new pressure distribution.

The FSI algorithm is described in more detail in Algorithm 3. First, a series of angles of attack is run with Rfoil to find α^*, which maximises the power harvesting factor. Then, the rib is deformed based on the previously determined pressure field, and the trim position is shifted. This inner loop is run until the relative structural change is below $\epsilon_R < 1 \times 10^{-4}$. With the structure and flow in equilibrium, the new optimal angle of attack α^* is determined for the current rib, and the inner loop is rerun. This procedure is repeated until the relative error in complementary energy of 1×10^{-5} for the outer loop is satisfied. The complementary energy was chosen as the FSI convergence metric because it includes both deformations and applied forces, a tighter criterion than pure deformations.

Algorithm 3 Optimisation algorithm with FSI.

1: Initialise design variables **x**
2: **while** NSGA II not converged **do**
3:     Initialise FSI ($\mathbf{u_t} = \mathbf{0}$)
4:     **while** $\epsilon > $ 1e-5 **do**
5:         Run Rfoil to obtain lift and drag polar
6:         Find $\zeta_{\max}$ and α^* for current configuration
7:         **while** $\epsilon_R > $ 1e-4 **do**
8:             Run FE model with $C_p(\alpha^*)$ to obtain $\mathbf{u_{t+1}}$
9:             Move bridle point to neutral line
10:        **end while**
11:        Update deformed aerofoil shape for Rfoil
12:     **end while**
13:     Update design variables **x**
14: **end while**
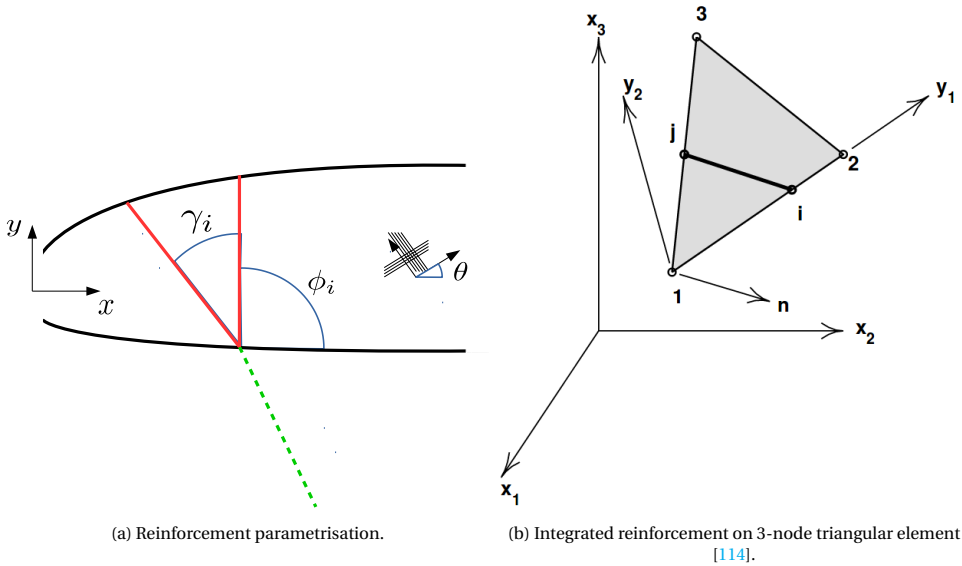
(a) Reinforcement parametrisation.

(b) Integrated reinforcement on 3-node triangular element [114].

Figure 5.1: Rib reinforcement layout.

5.2. Design Parametrisation

5.2.1. Reinforcements

The reinforcements are modelled as bar elements starting at each of the four LAPs in a group of five. For each group of reinforcements, two independent angles are defined to reduce the number of design variables to eight for the reinforcements only, shown in Figure 5.1a. By changing the absolute orientation angle ϕ_i, the whole group of reinforcements at LAP i is rotated, whereas changing the relative orientation angle γ_i changes the spread of reinforcement group i, respectively. The orthotropic material angle θ is defined as the angle between the x-axis and the warp threading of the fabric.

Compliance minimisation is a standard metric for structural optimisation and effectively maximises the structural stiffness. The compliance expression does not fully describe the force-displacement relationship for geometrically nonlinear structures due to its non-linearity. Instead, the complementary energy expression is chosen as a metric to describe the overall structural stiffness [129]. The complementary energy is computed as the integral of the deformation vector $\mathbf{u}$ with respect to the external load vector $\mathbf{f}$ [130]. This expression can be rewritten as

$$W_c = \int_0^{\mathbf{f}^*} \mathbf{u} \, d\mathbf{f} = \mathbf{u}^{*T} \mathbf{f}^* - W^*(\mathbf{u}),$$ (5.5)

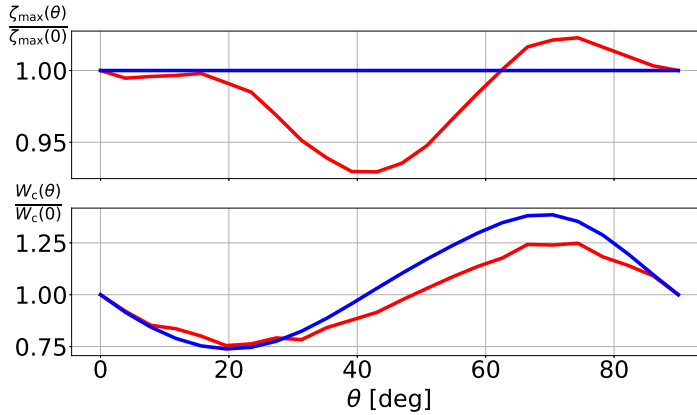where the asterisk denotes the quantities in equilibrium state and W the strain energy.

Figure 5.2: Material orientation angle θ against both objectives in deformed (red) and undeformed (blue) state.

5.2.2. Material Weave Direction

Figure 5.2 depicts both objectives normalised with their initial value at $\theta = 0$ as a function of the material orientation angle θ only, including (red) and ignoring (blue) the FSI routine, respectively. The chosen aerofoil shape is equivalent to the initial design for the optimisation introduced in the next section.

By excluding the FSI routine, the pressure load is applied to the undeformed profile only, and from it, the complementary energy is determined. As a result, a change in material orientation does not influence the power harvesting factor, and an overall variation of approximately 60% in complementary energy is observed. The lowest complementary energy is found at 20 degrees, corresponding to the overall stiffest structural layout in the given design space. On the other hand, the highest value corresponds to the material orientation such that the rib is primarily loaded in shear, causing maximum deformation.

Including the FSI routine introduces a dependence of the material orientation on the PHF, which peaks at 70 degrees causing the structure to deform in an aerodynamically economical manner. Conversely, at approximately 45 degrees material orientation angle, the deformed rib bulges at the suction side, reducing the effective PHF. A flat plateau can be seen between 10 to 30 degrees for the complementary energy and a peak at 70 degrees. Both objectives clearly work against each other for the initial aerofoil as their optima lay at different locations. Also, the peak in PHF results in a maximum in complementary energy, which means that the profile deforms so that the PHF is higher than the initial geometry. This peculiar phenomenon was not generally observed but rather a coincidence for this particular aerofoil.

5.2.3. Rib Profile Shape

Aerofoil profile optimisation has a broad application in aerospace for various design applications, such as finding profiles that maximise lift or glide ratio. Incorporating the profile into an optimisation routine requires a parametrisation that can describe a vari-

ety of profiles for a few design parameters. The Class Shape Transform (CST) parametrisation is such a method that represents shapes of aerodynamic bodies with a finite set of parameters. The method was initially introduced by Brenda Kulfan from Boeing [131] and has seen extensive use in aerodynamic and multidisciplinary design optimisation (MDO) applications. Special applications to wing design can be found in Ciampa [132] whereas interesting extensions have been proposed by Straathof [133]. A comparison of aerofoil parametrisation methods is presented by Sirpawadkul [134].

The design space for the rib profile was chosen to be CST aerofoil parameters consisting of the product of a class function $C_{(t)} : \mathbb{R} \to \mathbb{R}$ and a shape function $S_{(t,A_i)} : \mathbb{R}^{1+N} \to \mathbb{R}$, where N represents the order of the parametrisation and A_i is a tuple of N shape coefficients. The class function provides the base features of generic aerofoil shapes, whereas the shape function tailors the behaviour of the class function to represent specific aerofoils. The shape of aerofoil top (up/suction) and bottom (down/pressure) surfaces is written as

$$\eta(t) \quad = \quad \begin{cases} \eta_{(t)}^{top} = \ \ C_{(t)} S_{\left(t,A_i^{top}\right)} \\[2mm] \eta_{(t)}^{bot} = -C_{(t)} S_{\left(t,A_i^{bot}\right)} \end{cases} \tag{5.6}$$

$$\text{where} \quad \begin{cases} t = x/c \in [0,1] & \text{non-dimensional chord-wise coordinate} \\ \eta = z/c & \text{non-dimensional thickness coordinate} \\ A_i^{top} & \text{shape coefficient top side} \\ A_i^{bot} & \text{shape coefficients bottom side} \\ i = 0,1,2...M & \text{index of shape coefficients} \\ M = N-1 & \text{degree of parametrisation} \end{cases} \tag{5.7}$$

The class function for aerofoils with rounded leading edges and sharp trailing edges is written as

$$C_{(t)} = (1-t)\sqrt{t}. \tag{5.8}$$

The shape function is a polynomial of order N (degree $M = N-1$) obtained by a linear combination of the Bernstein polynomial basis with the A_i shape coefficients

$$S_{(t,A_i)} = \sum_{i=0}^{M} A_i s_{(t)}^{iM}. \tag{5.9}$$

The set of Bernstein polynomial functions of order N (degree $M = N-1$) forms of a complete basis for the space of polynomials of degree $M = N-1$. A linear homeomorphism exists between the Bernstein and canonical polynomial bases, but the Bernstein basis has more favourable numerical properties for higher-order settings with limited floating-point precision. The Bernstein basis functions of order N (degree $M = N-1$) are given in terms of the binomial coefficient

$$s_{(t)}^{iM} = \begin{pmatrix} M \\ i \end{pmatrix} t^i (1-t)^{M-i} \qquad \text{with} \qquad i = 0,1,2...M. \tag{5.10}$$

The binomial coefficient is often best visualised in Pascal's triangle, and the above expressions apply to parametrisation of arbitrary order. The basis of order N comprises all bases of a lower order, which is a favourable property in optimisation because a higher-order N includes all possible solutions of the lower orders. CST aerofoil parametrisation has proven itself as a solid approach to represent a complete set of aerofoil shapes that can be used for optimisation purposes.

5.3. MULTI-OBJECTIVE DESIGN OPTIMISATION

As depicted in the previous section, both optimisation objectives do not comply with each other. This common problem in multidisciplinary design optimisation can only be solved by compromising the two objectives. The Pareto front illustrates the boundary between feasible and infeasible solution space of two objectives and is obtained through the optimisation routine. The optimisation tool used to solve the underlying MDO is NS-GAII (Non-dominated Sorting Genetic Algorithm-II) which is a genetic, derivative-free method for numerical optimisation of non-convex continuous optimisation problems [135]. The power harvesting factor and the complementary energy expression vary non-linearly with small changes in the design vector due to the FSI analysis. NSGAII is capable of handling strong non-linearities, *NaN* value exceptions, and non-convexity and is therefore chosen as an optimiser. Also, NSGAII allows computing an entire Pareto front because the optimiser creates sets of solution generations that approach the infeasible boundary where the Pareto front resides. The objective function of the MDO consists of the power harvesting factor $\zeta_{\max}$ and the complementary energy W_{c}. The design variable vector consists of

$$\mathbf{x} = [\theta, \phi_i, \gamma_i, w_j^{\mathrm{top}}, w_j^{\mathrm{bot}}]^T \text{with} \quad i = 1,...,K \quad j = 1,...,N, \tag{5.11}$$

with the fibre angle, the absolute and relative reinforcements orientation angles, and the CST weights for the top and bottom side of the aerofoil, respectively. K is the number of reinforced LAPs, and N is the Bernstein polynomial function order. The optimisation problem is stated as

$$\underset{\mathbf{x}}{\text{minimize}} \ \mathbf{f}(\mathbf{x}) = [W_{\mathrm{c}}(\mathbf{x}), \ -\zeta_{max}(\mathbf{x})]^T$$
$$\text{subject to } \theta_i^{\min} \le \theta \le \theta_i^{\max}$$
$$\phi_i^{\min} \le \phi_i \le \phi_i^{\max}, \ i = 1,...,K$$
$$\gamma_i^{\min} \le \gamma_i \le \gamma_i^{\max}, \ i = 1,...,K$$
$$w_j^{\mathrm{top, \ min}} \le w_j^{\mathrm{top}} \le w_j^{\mathrm{top, \ max}}, \ j = 1,...,N$$
$$w_j^{\mathrm{bot, \ min}} \le w_j^{\mathrm{bot}} \le w_j^{\mathrm{bot, \ max}}, \ j = 1,...,N.$$

The PHF $\zeta_{\max}$ is defined as negative to comply with a minimisation statement. The box constraints on the angles can be found in Table 5.1 and the bounds on the Bernstein polynomial coefficients can be found in Table E.1. The order of the Bernstein polynomial function is chosen to be six, and their bounds are based on a collection of aerofoil data, including thick and high lift aerofoil designs. Finally, it should be emphasised that

(a) Pareto front for uncoupled optimisation.

(b) Highest PHF design.

(c) Compromised design ($W_c = 18$, $\zeta = 5.6$).
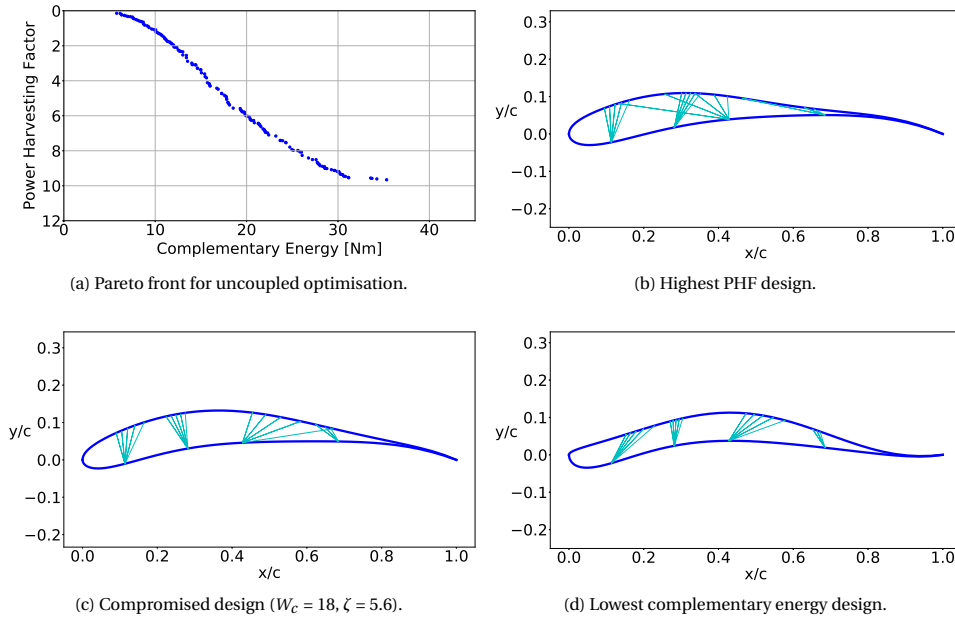

(d) Lowest complementary energy design.

Figure 5.3: MDO results without using FSI simulation.

strong nonlinearities are introduced in the objective function due to the fluid-structure coupling, and the obtained Pareto front is possibly not made of global optima solutions.

Table 5.1: Box constraints.

variable	θ [deg]	ϕ [deg]	γ [deg]
initial	45	90	15
min	0	45	5
max	90	135	20

5.3.1. OPTIMISATION WITHOUT FSI

The NSGAII is run with the full set of 21 design parameters for the uncoupled and FSI case. Figure 5.3a shows the resulting Pareto front between the two objectives ζ_{max} and W_c for an uncoupled optimisation. All solutions left of the frontier are infeasible because a higher ζ_{max} cannot be achieved without an increase in W_c. Similarly, all solutions right of the frontier are feasible but not optimal because a more dominant solution along the frontier exists. Hence, a Pareto front gives the user an idea of making optimal trade-offs between two objectives.

Figures 5.3b, 5.3c, and 5.3d depict three distinct aerofoil shapes and reinforcement layouts found on the Pareto front. Figure 5.3b is the profile with the highest obtained PHF of all individuals. The profile has a maximum thickness of approximately 10% and a thin trailing edge. The reinforcements are oriented towards the suction side, where

(a) Pareto front for FSI optimisation.

(b) Highest PHF design (FSI).

(c) Compromised design $W_c = 23$, $\zeta = 3$ (FSI).

(d) Lowest complementary energy design (FSI).
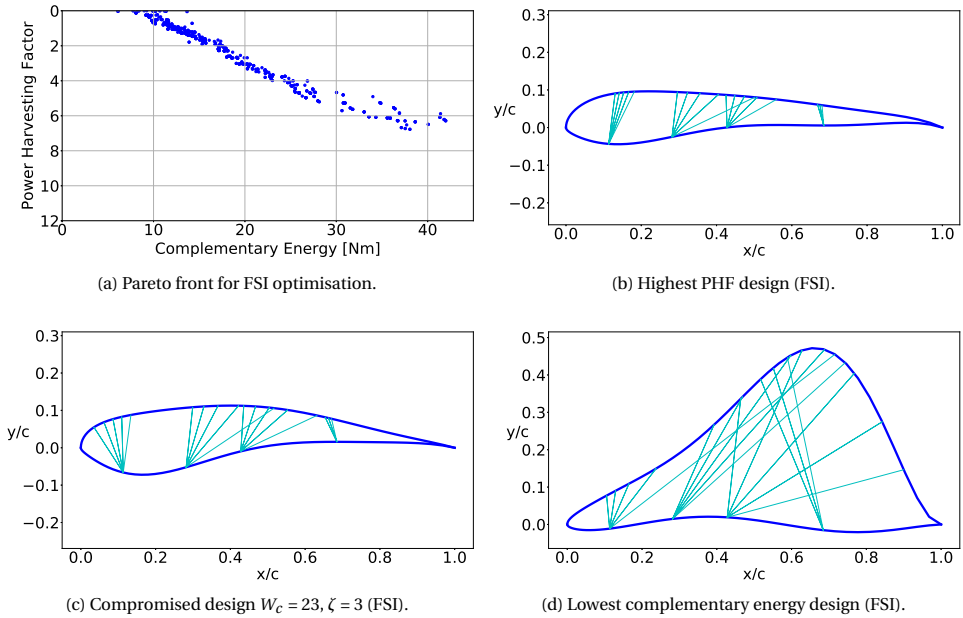
Figure 5.4: MDO results with FSI simulation.

the first two sets are more compressed in a direction, whereas the reinforcements from the third LAP spread out. Conversely, the resulting rib for the lowest complementary energy design in Figure 5.3d is shaped to minimise the resulting complementary energy. This is done by essentially forming the aerodynamically worst-performing profile such that the pressure forces acting on the rib are minimum. The reinforcements are oriented towards the mid-chord location, and the fibre orientation angle is 10 degrees. The rib with a compromised design in Figure 5.3c still exhibits a sharp profile with more camber than the high PHF design. The reinforcement orientation spreads towards the first third of the chord.

5.3.2. OPTIMISATION WITH FSI

The Pareto front, including the FSI in Figure 5.4a exhibits a larger non-feasible region than the uncoupled front. The maximum PHF of the uncoupled solution is almost twofold of the FSI case. Also, the complementary energy is higher for the same PHF in the case of the FSI frontier, which is caused by a more significant rib deformation.

For the optimal solution of the highest PHF design in Figure 5.4b the profile shows apparent differences to the uncoupled design. The optimiser favours a more prominent nose radius and overall thicker aerofoil when the maximisation of the PHF is considered only. The reinforcement orientation is characterised by spreading over the top surface in combination with a material orientation angle of 7 degrees. The optimal solution of the lowest W_c design in Figure 5.4d is a wedge-like profile with a maximum thickness at 70% chord. Again, an aerodynamically poor design is found, drastically reducing the
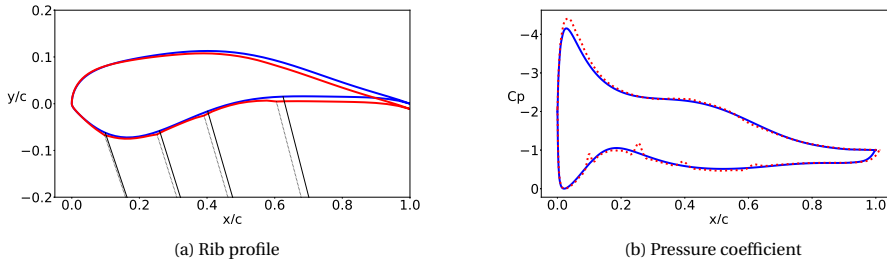
(a) Rib profile

(b) Pressure coefficient

Figure 5.5: Deformed (red) and undeformed (blue) compromised rib design.

overall pressure load and minimising the complementary energy. Also, the optimal compromised optimum in Figure 5.4c is a thicker aerofoil with a larger nose radius than the uncoupled optimum.

A qualitative inspection of the compromised designs leads to more insight into imperative design choices when the fluid-structure interaction is included in the design optimisation of ram-air kite ribs. Figure 5.5 outlines the undeformed and deformed rib and resulting pressure distribution in its final shape after FSI convergence. Critical aspects are the change in curvature on the top side, the minor kinks at the bottom side at each LAP, and the structural arching between the last two LAPs. Non-optimal designs typically show a deformed leading edge nose that is stretched towards the pressure peak, where its final shape differs from the initial nose shape. In the case of the optimum designs found on the Pareto front, the nose is slightly thicker and mainly resists traction due to the combined structural layout of profile shape and material and reinforcement orientation.

Elongation occurs mainly on the top side of the rib, where most aerodynamic forces act. The result is twofold - a non-smooth top side causes turbulent flow phenomena that generally reduce lift, whereas arching increases the local camber line and, as seen in the pressure coefficient, causes a decrease in pressure, i.e. increase in lift. It should be noted that Rfoil fails to present the physical phenomena of detached turbulent flow fully and, as a result, overestimates the produced lift force. Therefore, the pressure distribution should be interpreted with care, and the local pressure reduction due to increased camber may not be as prominent. Nevertheless, an imperative design choice is the correct placement of the reinforcements to locally reduce kinks and shape the bulging in an economical manner such that the flow stays attached. All these effects would not be considered when running the uncoupled case only. Another aspect that becomes apparent using FSI is the trim and optimal angle of attack, which changes between 10-30% compared to the uncoupled case, depending on the chosen design optimum on the Pareto front. In general, the deformed rib and extended bridles increase the relative angle of attack and, therefore, the trim position. Uncoupled approaches cannot represent this effect, and the reinforcement layout may not lay on the primary load path. Finally, the PHF with the FSI for the compromised profile is approximately 35% lower than the uncoupled solution. Utilising the FSI in the optimisation routine gives a more conservative result and the best design choice for the rib in a deformed flight state.
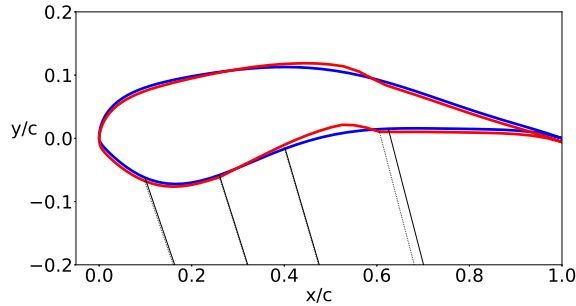
Figure 5.6: Undeformed (blue) and deformed (red) rib geometry with wrinkling model employed.

5.4. CONCLUSION

The MDO provides an insight into various aspects of profile and reinforcement shape optimisation for elastic rib profiles. A clear difference in design outcome is observed when the FSI analysis is part of the optimisation procedure. Noticeable features of the optimised profiles are a positive camber which maximises the lift coefficient, and an overall thicker profile for the coupled optimisation. The possible change in angle of attack due to deformation adds another nonlinear effect that the optimiser must tackle and might produce other local optima. It should be noted that optimisation results should always be interpreted with great care because the optimiser can only find optima for the underlying mathematical model, which is based on model assumptions. The results obtained from the optimisation in this work are atypical aerofoil designs found in parafoils. Possible reasons for that are the two-dimensional model reduction and the power harvesting factor as cost function. In a parafoil design, additional aspects like flight and structural stability and manufacturability play an essential role that is fully neglected in this study.

Regarding the absence of a wrinkling model, Figure 5.6 shows the compromised design layout and its deformation using a wrinkling model. A clear distinction in deformation between the third and fourth LAP can be seen. This deformation originates from the reduced stiffness due to compression and results in a more dominant bulging. The PHF for the deformed rib is 43% lower than computed without the wrinkling model. The complementary energy change is only 13% even though the deformations suggest otherwise. This tiny energy change is due to wrinkling, which slightly increases elastic strain energy. Based on this comparison, the wrinkling model is necessary to model the rib's deformation response correctly. Also, the convergence problems caused by the wrinkling model observed during the optimisation might originate from a non-realistic load determined by the simplified two-dimensional model, especially close to the trailing edge, which would result in a collapsed structure. Based on the results, an improvement in model accuracy and numerical stability could be obtained by a three-dimensional analysis of a single section, i.e. rib with two half panels on each side, to simulate the loads acting on the rib due to ballooning three-dimensional effects.

6

CONCLUSIONS AND RECOMMENDATIONS

This chapter concludes the results found in this work based on the developed method, and further recommendations for future work are given.

6.1. CONCLUSIONS

A numerical method has been developed to find the quasi-steady equilibrium shape and flight state of a tethered parafoil during flight. The theoretical background on computational structural dynamics was laid out in Chapter 3 where the kinetic dynamic relaxation method was derived and combined with a non-compression model. The method was numerically stable and accurately found the equilibrium state of a thin-walled membrane structure in a sufficiently short time. In Chapter 4 the structural solver was combined with a panel method and coupled using the software *preCICE*. The steady-state of the parafoil was found after 5-15 coupling iterations, and a mesh sensitivity study was performed. Compared to analytical and numerical solutions found in literature, the method showed promising results, even when large deformations occurred during the solution process. A validation using measurements from flight data was done, and the force coefficients from tether and steering belt showed a good resemblance with the simulation results for various flight speeds. The glide ratio was determined and compared with the simulation results from the flight data. It was found that the simulation overestimates the glide ratio by approximately 5-15%, depending on the flight speed. Also, the flight data showed widespread glide ratios, which originates in the model assumptions used to determine the glide ratio. A neutral flight scenario was simulated using tether and gravity influence, and the resulting elevation angles at the ground station and the steering pod showed a satisfying accuracy within 1-2 degrees. Finally, Chapter 5 introduced a multi-disciplinary design optimisation on a single parafoil rib where the optimiser was able to find various rib profile designs and reinforcement orientations that maximised the tether force and at the same time reduced the deformations in the rib.

Based on these results, the research questions stated in Chapter 2 can be answered:

How do different FSI methods for determining a ram-air kite's shape with bridle line system under load compare with respect to computational robustness and efficiency?
During the development of the fluid-structure interaction method it was found that both explicit and implicit coupling methods can find the deformed shape of the parafoil. The explicit coupling method found the equilibrium state after 5-10 iterations, whereas the implicit schemes took longer or diverged. This behaviour was only seen on one specific parafoil geometry used for verification purposes. The SkySails geometry, on the other hand did not converge using an explicit coupling, but the implicit method IQN-ILS did converge after 30-60 iterations. Therefore, it can be concluded that the effectiveness of each FSI coupling method is problem dependent, and both explicit and IQN-ILS coupling methods can determine the force equilibrium of the kite.

Is a panel code based on the potential flow assumption sufficiently accurate in estimating the aerodynamic characteristics of a ram-air kite? The developed method was validated against data measurements recorded during flight, and the simulation results matched well with the measured force acting on the tether and steering belt. This shows that the integrated pressure field from the panel code is sufficiently accurate for estimating the resultant force coefficient. Local flow effects have not been studied in detail except for a pressure coefficient distribution at the centre rib, and the comparison with CFD results show local discrepancies on the suction side. The glide ratio was determined experimentally but, due to model assumptions, had a significant variance, and it was shown that the FSI model overestimated the mean glide ratio by approximately 5-15%. It can be concluded that the developed method, in combination with a panel method, can determine both resultant force coefficient and glide ratio to sufficient accuracy for initial design and trim studies.

How can an engineering methodology be developed in order to design an efficient ram-air kite for AWE applications? It was shown that the integrated aero-structural model developed during this work could estimate various aerodynamic wing properties as well as mechanical stress and line forces. All these properties found by the model can test new design layouts and trim positions without field testing. Also, structural scaling effects are simple to implement, and their effects are crucial for AWE, which aims to operate large wing areas.

Is the current set of sensors in the operational airborne kite system sufficient for proper validation of integrated models? As shown in Chapter 4 the sensor data was used to validate the numerical model. Despite many data points recorded during flight, uncertainties due to the wind speed sensors and model assumptions introduced a significant variance when the glide ratio was determined. This shows that the sensor setup could be improved, e.g., introducing an angle of attack sensor that allows to determine lift and drag coefficients directly and thus glide ratio.

6.2. RECOMMENDATIONS

Based on the conclusions mentioned above, several recommendations about improvements of the method and model validations can be made.

AERODYNAMIC MODEL

The panel method determined the pressure distribution that is acting on the canopy. Despite its computational speed, the method cannot model flow separation that occurs at larger angles of attack. Without separation, the lift is generally overestimated as shown in Section 4.4.4 and a trim angle variation should also occur. Therefore, a thorough comparison between CFD and panel method is recommended to estimate the boundary of valid results from the panel method. Furthermore, the influence of the inlets on the flow field should be studied to justify the assumption made in this work by simply ignoring them. Finally, the frozen wake assumption used in *APAME* is another source of error in the pressure field and should be relaxed such that the wake develops over several iterations.

STRUCTURE MODEL

The recommendations for improving the structure model are using a more realistic material model and validation using experimental data. The material response of woven fabric is generally nonlinear and depends on factors like load ratio between warp and weft direction and load magnitude. The material model used in this work is only applicable to materials with linear stress-strain relation and small strains. A recommendation is to test the influence of the material model choice on stress and deformation. Validating the numerical model using an experimental setup, e.g. measuring the displacement field of an inflated airbag with photogrammetry, could be an excellent approach to test different material models. Another improvement could be done on the finite element mesh. In Chapter 3 it was mentioned that CST elements were used exclusively to model the membrane structure even though these types of elements potentially result in a stiffer structure compared to higher order elements. Therefore, other types of elements with at least quadratic shape functions should be tested with the KDR solver and the differences in stress and deformation field should be investigated. Finally, the panel shortening in the SkySails kite model should be added to find the differences between both models.

FLUID-STRUCTURE COUPLING

The coupling methods provided by *preCICE* were sufficient to obtain convergence, but the number of iterations, especially for the SkySails kite geometry, could still be improved. The IQN-ILS method requires several tuning parameters to be manually optimised to obtain reasonable convergence behaviour. Therefore, finding a suitable fixed-point iteration method with fewer or no tuning parameters would substantially simplify the coupling on new geometries. Also, it was shown in Chapter 5 that the coupling could also be done by estimating the angle of attack, which results in a zero moment coefficient. This approach could also be used to initialise the coupling and speed up the convergence in return.

VALIDATION USING FLIGHT DATA

The sensor setup used during this work did not measure the angle of attack during the flight. Therefore, the lift and drag coefficient could not be determined, and critical parameters like the glide ratio had to be estimated using the equation of motion. This approach introduced additional variables like the angle between the tether wind axis at the ground station, which massively increased the variance. On the other hand, a sensor measuring the angle of attack would allow a direct measurement of the glide ratio. Also, to validate local flow effects in a more controlled environment, the FSI should be validated in a wind tunnel.

OPTIMISATION

The developed optimisation procedure for profile shape and reinforcement orientation was only done on a two-dimensional rib. The same approach could be applied to an entire parafoil geometry to find a resilient reinforcement layout for the kite. Additional parameters such as LAP positioning could be introduced to optimise the load path through each rib.

6

ACKNOWLEDGEMENTS

First, I would like to thank the committee members for taking their time to read this dissertation and provide helpful feedback on improvements. I would also like to thank my promoter, Gerard van Bussel, for guiding me through the PhD and helping me with the structuring of the dissertation. I would also like to express my appreciation to my co-promoter, Roland Schmehl. His enthusiasm and optimism for airborne wind energy were always inspiring to me. I appreciated the weekly FSI meetings with you and the other PhD candidates when we discussed technical questions in great detail, and we could help each other on many occasions. Also, being part of the AWESCO network allowed us to travel several times within Europe and visit universities and companies affiliated with AWE research. It was a great pleasure to spend time with the group of PhD candidates from all over the world and build a network and collaborations with other researchers. I would also like to thank Moritz Diehl, who offered me to continue my research at his institute when SkySails had financial difficulties.

Nevertheless, I spent a long time of my PhD with SkySails Power in Hamburg. I want to thank all the employees accompanying me on my journey. Countless inspiring discussions about kite dynamics, numerical models and engineering methods helped me get where I am today. As of today, I still enjoy the innovative work with SkySails Power and hope to continue on this path.

And finally, I would like to thank my family and girlfriend, who gave me support and encouragement during some difficult times.

A

TENSOR ALGEBRA

The concept of tensors is introduced to understand the essential derivation of membrane kinematics. In general, a tensor can be described as a function that takes in multiple arguments, is linear in each of them, and maps into an underlying field. Tensors can be categorised in orders, where the tensor order is equivalent to the number of input arguments. A tensor of order zero is a scalar without components or basis. A tensor of order one is a vector and can map another vector into a scalar with the inner product. A second-order tensor (e.g. a matrix) is the tensor product of two vectors and maps a vector into another vector. Tensors describe physical quantities such as forces, velocities, or mechanical stress. Depending on which coordinate system is used to describe these quantities, the tensor components change under change of basis while the tensor as a whole is invariant, and for that particular reason, they are an elegant notation. This section introduces tensor notation with co-variant and contra-variant basis vectors, which is important when curvilinear coordinates are used. For a thorough introduction into tensor algebra, refer to Grinfeld [136] or Chapelle. [94]

A.0.1. VECTORS

A vector defined in $\mathbb{R}^3$ in an arbitrary coordinate system with linearly independent basis vectors $\mathbf{g}_i$ (with $i = 1, 2, 3$) is defined as

$$\mathbf{x} = \sum_{i=1}^{3} x^i \mathbf{g}_i = x^i \mathbf{g}_i, \tag{A.1}$$

where x^i are the coordinates for basis vectors $\mathbf{g}_i$ which do not have to be orthogonal nor have unit length. The summation sign can be omitted using the Einstein summation convention, which implies a summation of components with the same index. As will be explained next, the sub and superscript notation used for the coordinates and basis vectors distinguish between co-variant and contra-variant components. In order to determine the coordinates from vector $\mathbf{x}$ let us define a set of basis vectors $\mathbf{g}^i$ such that

A

$$\mathbf{g}_i \cdot \mathbf{g}^j = \delta_i^j, \tag{A.2}$$

where δ_i^j is the Kronecker delta which is simply a function that takes two indices as input and returns a scalar of either 0 or 1. It is written as

$$\delta_i^j = \begin{cases} 0 & \text{if} \quad j \neq i \\ 1 & \text{if} \quad j = i. \end{cases} \tag{A.3}$$

The basis vector $\mathbf{g}_i$ using subscript notation is referred to as the co-variant basis vector, whereas $\mathbf{g}^i$ using superscript indices is the contra-variant basis vector. By definition, the co-variant and contra-variant basis vectors are orthogonal such that A.2 always holds. Using this relation, the vector coordinates can be found with

$$\mathbf{x} \cdot \mathbf{g}^j = x^i \mathbf{g}_i \cdot \mathbf{g}^j = x^i \delta_i^j = x^j. \tag{A.4}$$

It can be seen that the basis vectors $\mathbf{g}^i$ map $\mathbf{x}$ into the contra-variant coordinate components. The vector $\mathbf{x}$ can also be expressed with its contra-variant basis as

$$\mathbf{x} = x_i \mathbf{g}^i, \tag{A.5}$$

where x_i are the co-variant vector coordinates for the contra-variant basis. In a Cartesian coordinate system, both co-variant and contra-variant basis vectors are equivalent, whereas using curvilinear coordinates, they generally differ. Next, the inner product between two arbitrary vectors using only co-variant, contra-variant, or mixed basis vectors respectively can be expressed as

$$\mathbf{x} \cdot \mathbf{y} = x^i y^j \mathbf{g}_i \cdot \mathbf{g}_j \tag{A.6a}$$
$$= x_i y_j \mathbf{g}^i \cdot \mathbf{g}^j \tag{A.6b}$$
$$= x^i y_j \mathbf{g}_i \cdot \mathbf{g}^j \tag{A.6c}$$
$$= x_i y^j \mathbf{g}^i \cdot \mathbf{g}_j. \tag{A.6d}$$

All four expressions are equivalent, but their coordinates and basis vectors differ. The product of two co-variant basis vectors are known as the metric tensor written as

$$\mathbf{g}_i \cdot \mathbf{g}_j = g_{ij}. \tag{A.7}$$

The metric tensor is a crucial function that inputs two vectors and produces a scalar, similar to the inner product. In Cartesian coordinates, the metric tensor is equivalent to the identity matrix, but for vector fields defined on curved surfaces, the metric tensor changes from location to location and defines a measure of the length of two vectors and the angle between them. The product of contra-variant basis vectors gives its inverse

$$[g_{ij}]^{-1} = \mathbf{g}^i \cdot \mathbf{g}^j = g^{ij}. \tag{A.8}$$

A.0.2. TENSORS

A second-order (or higher) tensor generalises a vector to higher dimensions. A second-order tensor $\mathbf{T}$ can be written as a tensor product of two vectors $\mathbf{a}$ and $\mathbf{b}$

$$\mathbf{T} = \mathbf{a} \otimes \mathbf{b}, \qquad \mathbf{a} \in V, \quad \mathbf{b} \in W, \tag{A.9}$$

where V and W are two vector spaces, and $\otimes$ is the tensor product operator. The tensor can map a vector $\mathbf{c} \in W$ into V using

$$\mathbf{Tc} = (\mathbf{a} \otimes \mathbf{b})\mathbf{c} \tag{A.10a}$$

$$= (\mathbf{b} \cdot \mathbf{c})\mathbf{a}, \tag{A.10b}$$

where $(\mathbf{b} \cdot \mathbf{c})$ is the inner product between $\mathbf{b}$ and $\mathbf{c}$. When specifying vectors $\mathbf{a}$ and $\mathbf{b}$ in a coordinate system the tensor $\mathbf{T}$ can be written as

$$\mathbf{T} = \sum_{i}^{N} \sum_{j}^{M} T^{ij} \mathbf{g}_i \otimes \mathbf{g}_j = T^{ij} \mathbf{g}_i \otimes \mathbf{g}_j, \tag{A.11}$$

where T^{ij} are the contra-variant components and $\mathbf{g}_i \otimes \mathbf{g}_j$ is the tensor product of the basis vectors. The components of a tensor can also be represented in matrix form, e.g. if $N = 3$ and $M = 3$

$$T^{ij} = \begin{bmatrix} T_{11} & T_{12} & T_{13} \\ T_{21} & T_{22} & T_{23} \\ T_{31} & T_{32} & T_{33,} \end{bmatrix} \tag{A.12}$$

and they are determined by

$$\begin{array}{lll} T_{11} = \mathbf{g}_1 \cdot (\mathbf{T} \cdot \mathbf{g}_1) & T_{12} = \mathbf{g}_1 \cdot (\mathbf{T} \cdot \mathbf{g}_2) & T_{13} = \mathbf{g}_1 \cdot (\mathbf{T} \cdot \mathbf{g}_3) \\ T_{21} = \mathbf{g}_2 \cdot (\mathbf{T} \cdot \mathbf{g}_1) & T_{22} = \mathbf{g}_2 \cdot (\mathbf{T} \cdot \mathbf{g}_2) & T_{23} = \mathbf{g}_2 \cdot (\mathbf{T} \cdot \mathbf{g}_3) \\ T_{31} = \mathbf{g}_3 \cdot (\mathbf{T} \cdot \mathbf{g}_1) & T_{32} = \mathbf{g}_3 \cdot (\mathbf{T} \cdot \mathbf{g}_2) & T_{33} = \mathbf{g}_3 \cdot (\mathbf{T} \cdot \mathbf{g}_3). \end{array} \tag{A.13}$$

Similar to vectors, second-order tensors can also be presented in co-variant, contra-variant, and mixed form

$$\mathbf{T} = T^{ij} \mathbf{g}_i \otimes \mathbf{g}_j \tag{A.14a}$$

$$= T_{ij} \mathbf{g}^i \otimes \mathbf{g}^j \tag{A.14b}$$

$$= T_i^{\ j} \mathbf{g}^i \otimes \mathbf{g}_j \tag{A.14c}$$

$$= T_j^{\ i} \mathbf{g}_i \otimes \mathbf{g}^j. \tag{A.14d}$$

Next, the product between two second-order tensors can be written as

$$(\mathbf{a} \otimes \mathbf{b})(\mathbf{c} \otimes \mathbf{d}) = (\mathbf{b} \cdot \mathbf{c})(\mathbf{a} \otimes \mathbf{d}), \tag{A.15}$$

and in index notation

A

$$\mathbf{TU} = (T^{ij}\mathbf{g}_i \otimes \mathbf{g}_j)(U^{kl}\mathbf{g}_k \otimes \mathbf{g}_l) \tag{A.16a}$$

$$= T^{ij}U^{kl}(\mathbf{g}_j \cdot \mathbf{g}_k)\mathbf{g}_i \otimes \mathbf{g}_l = T^{ij}U^{kl}g_{jk}\mathbf{g}_i \otimes \mathbf{g}_l \tag{A.16b}$$

$$= T_{ij}U_{kl}g^{jk}\mathbf{g}^i \otimes \mathbf{g}^l \tag{A.16c}$$

$$= T^{ij}U_{kl}\mathbf{g}_i \otimes \mathbf{g}^j. \tag{A.16d}$$

It can be seen that the product of two second-order tensors results in another second-order tensor. Finally, the double-dot product can be introduced, which reduces two second-order tensors to a scalar

$$\mathbf{T}{:}\mathbf{U} = T^{ij}U_{kl}(\mathbf{g}_i \otimes \mathbf{g}_j){:}(\mathbf{g}^k \otimes \mathbf{g}^l) \tag{A.17a}$$

$$= T^{ij}U_{kl}(\mathbf{g}_j \cdot \mathbf{g}^k)(\mathbf{g}_i \cdot \mathbf{g}^l) = T^{lk}U_{kl}. \tag{A.17b}$$

A.0.3. CHANGE OF BASIS

Changing the basis of a second-order tensor in an arbitrary coordinate system and determining its components can be done using the previously derived co-variant and contra-variant notation. Let **T** be a second-order tensor and **T**′ the same tensor with a different basis

$$\mathbf{T} = \mathbf{T}' \tag{A.18}$$

in components and respective basis vectors, it can be written as

$$T^{ij}\mathbf{g}_i \otimes \mathbf{g}_j = T'^{ij}\mathbf{e}_i \otimes \mathbf{e}_j \tag{A.19}$$

where both basis vectors are written in their co-variant basis. Extending both sides with contra-variant basis vectors $\mathbf{e}^k$ and $\mathbf{e}^l$ results in

$$\mathbf{e}^k \cdot T^{ij}(\mathbf{g}_i \otimes \mathbf{g}_j) \cdot \mathbf{e}^l = \mathbf{e}^k \cdot T'^{ij}(\mathbf{e}_i \otimes \mathbf{e}_j) \cdot \mathbf{e}^l \tag{A.20}$$

applying Equation A.10 the tensor product can be broken up into

$$(\mathbf{e}^k \cdot \mathbf{g}_i)T^{ij}(\mathbf{g}_j \cdot \mathbf{e}^l) = (\mathbf{e}^k \cdot \mathbf{e}_i)T'^{ij}(\mathbf{e}_j \cdot \mathbf{e}^l)$$
$$J_i^k T^{ij} J_j^l = \delta_i^k T'^{ij}\delta_j^l \tag{A.21}$$
$$= T'^{kl},$$

where **J** is the Jacobian with components

$$\mathbf{J} = \begin{bmatrix} \mathbf{e}^1 \cdot \mathbf{g}_1 & \mathbf{e}^1 \cdot \mathbf{g}_2 & \mathbf{e}^1 \cdot \mathbf{g}_3 \\ \mathbf{e}^2 \cdot \mathbf{g}_1 & \mathbf{e}^2 \cdot \mathbf{g}_2 & \mathbf{e}^2 \cdot \mathbf{g}_3 \\ \mathbf{e}^3 \cdot \mathbf{g}_1 & \mathbf{e}^3 \cdot \mathbf{g}_2 & \mathbf{e}^3 \cdot \mathbf{g}_3 \end{bmatrix}, \tag{A.22}$$

which transforms a tensor basis.

B

STRESS MEASURES

The Cauchy stress tensor σ relates the force to the area, both given in the current configuration. Cauchy's stress theorem defines the traction $\mathbf{t}$ as

$$\mathbf{t} = \mathbf{n}\sigma = \sigma^T\mathbf{n}. \tag{B.1}$$

The equivalent expression in the reference configuration is written as

$$\mathbf{t}_0 = \mathbf{P}\mathbf{n}_0. \tag{B.2}$$

where $\mathbf{P}$ is the first Piola-Kirchhoff stress tensor relating the force in the current configuration to the area in the reference configuration, and because of that, the tensor usually is non-symmetric. Both stress tensors can be related using

$$\mathbf{P} = J\sigma\mathbf{F}^{-T}, \tag{B.3}$$

with J being the determinant of the deformation gradient $\mathbf{F}$. Due to the non-symmetry of $\mathbf{P}$ the second Piola-Kirchhoff stress tensor $\mathbf{S}$ is introduced, which relates both force and area in the reference configuration

$$\mathbf{S} = \mathbf{P}\mathbf{F}^{-T}. \tag{B.4}$$

It should be noted that $\mathbf{S}$ is not a physical stress measure and should not be used for post-processing the FEM results. Instead, the Cauchy stress should be used, which can be determined using the relation

$$\sigma = J^{-1}\mathbf{F}\mathbf{S}\mathbf{F}^T. \tag{B.5}$$

In curvilinear coordinates, the second Piola-Kirchhoff stress tensor is expressed with co-variant basis vectors as

$$\mathbf{S} = S^{\alpha\beta}\mathbf{G}_\alpha \otimes \mathbf{G}_\beta. \tag{B.6}$$

C

Constitutive Model

The constitutive relation between stress and strain is described by the fourth order stiffness tensor $\mathbb{C}$ which maps the strain $\mathbf{E}$ into stress $\mathbf{S}$. It is a generalisation of Hooke's Law for elastic materials and contains 81 components. The stress-strain relation can be derived from the strain energy density function $\phi(\mathbf{E})$ which is defined as

$$\phi(\mathbf{E}) = \frac{1}{2}\mathbf{E} : \mathbb{C} : \mathbf{E}. \tag{C.1}$$

Taking the derivative with respect to the strain $\mathbf{E}$, the stress can be expressed as

$$\mathbf{S} = \frac{\partial \phi(\mathbf{E})}{\partial \mathbf{E}} = \mathbb{C} : \mathbf{E}. \tag{C.2}$$

The stiffness tensor can be simplified under plane stress assumptions, which applies to thin plates or membranes and results in little stress in the thickness direction. Using Voigt notation, the relation can be written in matrix form such that

$$\begin{bmatrix} S_{11} \\ S_{22} \\ S_{12} \end{bmatrix} = \begin{bmatrix} C_{11} & C_{12} & C_{13} \\ C_{21} & C_{22} & C_{23} \\ C_{31} & C_{32} & C_{33} \end{bmatrix} \begin{bmatrix} E_{11} \\ E_{22} \\ \gamma_{12} \end{bmatrix}. \tag{C.3}$$

In the case of isotropic material, the stiffness tensor properties can be described with two independent variables: Young's modulus E and Poisson's ratio ν. In matrix form $\mathbb{C}$ is written as

$$[\mathbb{C}^{\text{iso}}] = \frac{E}{1 - \nu^2} \begin{bmatrix} 1 & \nu & 0 \\ \nu & 1 & 0 \\ 0 & 0 & \frac{1-\nu}{2} \end{bmatrix}. \tag{C.4}$$

For orthotropic material which has two main stiffness directions, the stiffness tensor requires a total of five independent variables, two Young's moduli E_x and E_y, two Poisson's ratios ν_{xy} and ν_{yx}, and the shear modulus G_{xy}. The material properties of woven fabrics can be assumed to behave as orthotropic, and the stiffness directions then align with the
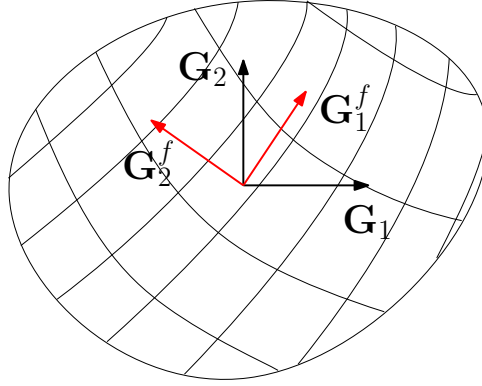
Figure C.1: Surface made of woven fabric with local basis (in red) aligned with weave indicating that a change in basis is required.

weave pattern, e.g. E_x being the stiffness in the warp direction and E_y in weft direction [137]. The stiffness tensor for orthotropic materials in matrix form is written as

$$[\mathbb{C}^{\text{ortho}}] = \frac{1}{1 - \nu_{xy}\nu_{yx}} \begin{bmatrix} E_x & \nu_{yx}E_x & 0 \\ \nu_{xy}E_y & E_y & 0 \\ 0 & 0 & \frac{1-\nu_{xy}\nu_{yx}}{G_{xy}} \end{bmatrix}. \tag{C.5}$$

The orthotropic constitutive matrix is only valid on the local fibre basis. Figure C.1 depicts a curved surface of woven fibres. The local fibre basis is described with two tangent vectors $\mathbf{G}_\alpha^{\text{f}}$ and does not necessarily align with the local basis vectors $\mathbf{G}_\alpha$. Since the strain tensor is defined for contra-variant basis vectors and the stress using co-variant basis vectors, both strain and stress require their own Jacobian to transform between fibre and local basis. The change of basis of the strain tensor is written as

$$\mathbf{E} = \mathbf{J}_E^T \mathbf{E}^{\text{fibre}} \mathbf{J}_E, \tag{C.6}$$

and similarly the change of basis of the stress tensor

$$\mathbf{S} = \mathbf{J}_S^T \mathbf{S}^{\text{fibre}} \mathbf{J}_S. \tag{C.7}$$

Applying the change of basis shown in Section A.0.3 the Jacobian for the strain tensor is written as

$$\mathbf{J}_E = \begin{bmatrix} \mathbf{G}^{\text{f1}} \cdot \mathbf{G}_1 & \mathbf{G}^{\text{f1}} \cdot \mathbf{G}_2 & \mathbf{G}^{\text{f1}} \cdot \mathbf{G}_3 \\ \mathbf{G}^{\text{f2}} \cdot \mathbf{G}_1 & \mathbf{G}^{\text{f2}} \cdot \mathbf{G}_2 & \mathbf{G}^{\text{f2}} \cdot \mathbf{G}_3 \\ \mathbf{G}^{\text{f3}} \cdot \mathbf{G}_1 & \mathbf{G}^{\text{f3}} \cdot \mathbf{G}_2 & \mathbf{G}^{\text{f3}} \cdot \mathbf{G}_3 \end{bmatrix}, \tag{C.8}$$

and the Jacobian for the stress tensor is

$$\mathbf{J}_S = \begin{bmatrix} \mathbf{G}_1^{\text{f}} \cdot \mathbf{G}^1 & \mathbf{G}_1^{\text{f}} \cdot \mathbf{G}^2 & \mathbf{G}_1^{\text{f}} \cdot \mathbf{G}^3 \\ \mathbf{G}_2^{\text{f}} \cdot \mathbf{G}^1 & \mathbf{G}_2^{\text{f}} \cdot \mathbf{G}^2 & \mathbf{G}_2^{\text{f}} \cdot \mathbf{G}^3 \\ \mathbf{G}_3^{\text{f}} \cdot \mathbf{G}^1 & \mathbf{G}_3^{\text{f}} \cdot \mathbf{G}^2 & \mathbf{G}_3^{\text{f}} \cdot \mathbf{G}^3 \end{bmatrix}. \tag{C.9}$$

D

CONSERVATION OF LINEAR MOMENTUM

The Cauchy momentum equation is the basis of structural mechanics as it describes the force balance inside a continuum derived from the conservation of linear momentum. It is derived from the stress balance found in a square continuum element using Cartesian coordinates as depicted in Figure D.1. The continuum element is an infinitesimally small square with mass m located in an arbitrary elastic continuum Ω with side lengths Δx and Δy and thickness h. Based on the plane stress assumption applicable to thin membranes, the stress acting in normal direction is negligibly small and can therefore be assumed to be zero. The Cauchy stress field is given by the tensor field $\sigma(x, y)$ consists of normal, and shear components in both x and y-direction acting on each side of the continuum element and they are expressed as a function of position. Additionally, body force **f** acts on the volume induced by gravity or other fields, and derived from the figure, a force balance in both x and y-direction based on Newton's second law of motion can be constructed

$$m\frac{\partial v_x}{\partial t} = \left[\sigma_{xx}(x + \Delta x, y) - \sigma_{xx}(x, y)\right]\Delta y h + \left[\tau_{yx}(x, y + \Delta y) - \tau_{yx}(x, y)\right]\Delta x h + f_x, \quad \text{(D.1a)}$$

$$m\frac{\partial v_y}{\partial t} = \left[\sigma_{yy}(x, y + \Delta y) - \sigma_{yy}(x, y)\right]\Delta y h + \left[\tau_{xy}(x + \Delta x, y) - \tau_{xy}(x, y)\right]\Delta x h + f_y, \quad \text{(D.1b)}$$

where v_x and v_y are the velocity components. The stress terms located at $x + \Delta x$ and $y + \Delta y$ can both be written in terms of the Taylor series expansion, here only for σ_{xx}

$$\sigma_{xx}(x + \Delta x, y) = \sigma_{xx}(x, y) + \frac{\partial \sigma_{xx}(x, y)}{\partial x}\Delta x + \mathcal{O}(\Delta x^2), \quad \text{(D.2)}$$

where quadratic and higher-order terms are discarded. Substituting Equation D.2 into the force balance for all stress components and cancelling the length terms results in
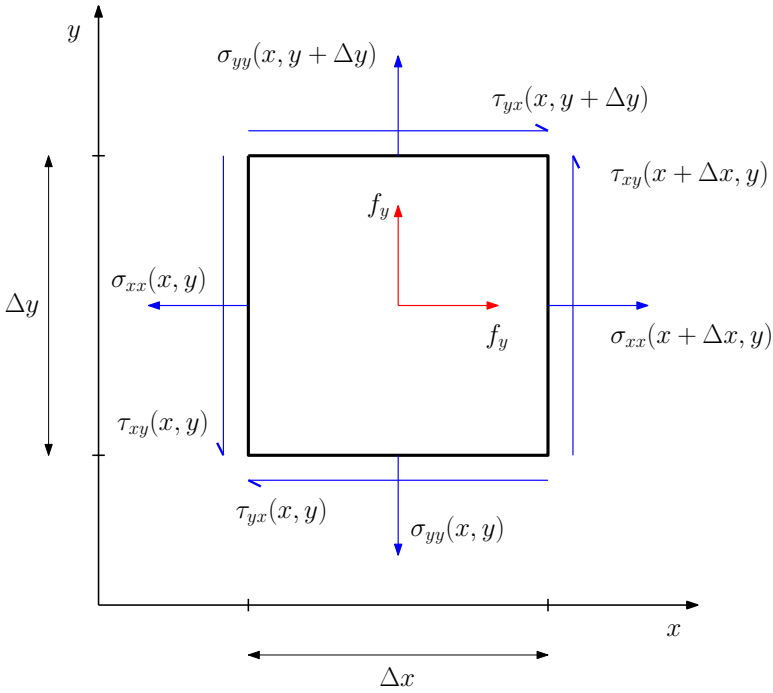
Figure D.1: Cauchy stress field in a continuum element.

$$\rho \frac{\partial v_x}{\partial t} = \frac{\partial \sigma_{xx}(x,y)}{\partial x} + \frac{\partial \tau_{yx}(x,y)}{\partial y} + \rho b_x$$

$$\rho \frac{\partial v_y}{\partial t} = \frac{\partial \sigma_{yy}(x,y)}{\partial y} + \frac{\partial \tau_{xy}(x,y)}{\partial x} + \rho b_y,$$
(D.3)

where the mass term was replaced with $\rho \Delta x \Delta y h$, and the body forces per unit volume with b_x and b_y. Finally, both equations can be written in a single equation using tensor notation

$$\rho \frac{\partial \mathbf{v}}{\partial t} = \nabla \cdot \sigma + \rho \mathbf{b},$$
(D.4)

where $\nabla \cdot$ is the divergence operator acting on the stress tensor. The conservation of linear momentum expressed in Equation D.4 states that the momentum change rate is equal to the sum of all forces acting on it. It is a governing equation that is valid everywhere in the continuum Ω, and in the case of small accelerations, the left-hand side can be assumed to be zero, and the problem is called static.

With a set of Dirichlet and Neumann boundary conditions, it forms an initial bound-

ary value problem

$$\rho \frac{\partial \mathbf{v}}{\partial t} = \nabla \cdot \sigma + \rho \mathbf{b} \qquad \text{in} \quad \Omega \qquad \text{(D.5a)}$$

$$\mathbf{n}\sigma = \mathbf{t} \qquad \text{on} \quad \Gamma_t \qquad \text{(D.5b)}$$

$$\mathbf{u} = \mathbf{u}^* \qquad \text{on} \quad \Gamma_u. \qquad \text{(D.5c)}$$

On the Neumann boundary, Γ_t the traction $\mathbf{t}$ acts on the body, and displacements $\mathbf{u}^*$ on Γ_u resemble the Dirichlet boundary condition such that the displacement field is fixed to a prescribed value. This formulation can be transformed to domain Ω_0 with boundary conditions acting on Γ_{t_0} and Γ_{u_0} in the reference configuration

D

$$\rho_0 \frac{\partial \mathbf{v}}{\partial t} = \nabla_0 \cdot \mathbf{P} + \rho_0 \mathbf{b} \qquad \text{in} \quad \Omega_0 \qquad \text{(D.6a)}$$

$$\mathbf{P}\mathbf{n}_0 = \mathbf{t}_0 \qquad \text{on} \quad \Gamma_{t_0} \qquad \text{(D.6b)}$$

$$\mathbf{u} = \mathbf{u}^* \qquad \text{on} \quad \Gamma_{u_0}. \qquad \text{(D.6c)}$$

Equation D.6a is called the Total Lagrangian formulation, and with its boundary conditions, it is referred to as the strong form. The word strong does not mean it is superior to its weak integral formulation but instead specifies the requirement of a twice differentiable field $\mathbf{u}$ which at the same time satisfies all boundary conditions.

E

INITIAL CONDITIONS FOR AEROFOIL SHAPE OPTIMISATION

Table E.1: Initial Bernstein polynomial coefficients.

variable	w_1^{top}	w_2^{top}	w_3^{top}	w_4^{top}	w_5^{top}	w_6^{top}
initial	0.3	0.3	0.3	0.3	0.3	0.3
min	0.0874	0.1028	0.0267	-0.0444	-0.0413	-0.1429
max	0.5254	0.5438	0.7101	0.6479	0.4681	0.5438
	w_1^{bot}	w_2^{bot}	w_3^{bot}	w_4^{bot}	w_5^{bot}	w_6^{bot}
initial	0.3	0.3	0.3	0.3	0.3	0.3
min	0.0553	-0.1324	-0.2729	-0.2852	-0.3228	-0.4128
max	0.6446	0.7203	0.9058	0.7813	0.3194	0.4164

REFERENCES

1. IEA: Electricity - Fuels & Technology. https://www.iea.org/fuels-and-technologies/electricity, IEA, Paris, 2020

2. IEA: World Energy Outlook 2020 - Achieving net-zero emissions by 2050. https://www.iea.org/reports/world-energy-outlook-2020/achieving-net-zero-emissions-by-2050, IEA, Paris, 2020

3. IEA: Renewables 2020. https://www.iea.org/reports/renewables-2020, IEA, Paris, 2020

4. Jung, C., Schindler, D., Laible, J.: National and global wind resource assessment under six wind turbine installation scenarios. Energy conversion and management **156**, 403–415 (2018). doi: 10.1016/j.enconman.2017.11.059

5. Edenhofer, O., Pichs-Madruga, R., Sokona, Y., Seyboth, K., Matschoss, P., Kadner, S., Zwickel, T., Eickemeier, P., Hansen, G., Schlömer, S., et al.: IPCC special report on renewable energy sources and climate change mitigation. Prepared By Working Group III of the Intergovernmental Panel on Climate Change, Cambridge University Press, Cambridge, UK (2011)

6. Fechner, U.: A methodology for the design of kite-power control systems. Ph.D. Thesis, Delft University of Technology, Delft, the Netherlands, 2016. doi: 10.4233/uuid:85efaf4c-9dce-4111-bc91-7171b9da4b77

7. Archer, C., Caldeira, K.: Global assessment of high-altitude wind power. Energies **2**(2), 307–319 (2009). doi: 10.3390/en20200307

8. Vermillion, C., Cobb, M., Fagiano, L., Leuthold, R., Diehl, M., Smith, R. S., Wood, T. A., Rapp, S., Schmehl, R., Olinger, D., et al.: Electricity in the air: Insights from two decades of advanced control research and experimental flight testing of airborne wind energy systems. Annual Reviews in Control (2021). doi: 10.1016/j.arcontrol.2021.03.002

9. Watson, S., Moro, A., Reis, V., Baniotopoulos, C., Barth, S., Bartoli, G., Bauer, F., Boelman, E., Bosse, D., Cherubini, A., Croce, A., Fagiano, L., Fontana, M., Gambier, A., Gkoumas, K., Golightly, C., Latour, M. I., Jamieson, P., Kaldellis, J., Macdonald, A., Murphy, J., Muskulus, M., Petrini, F., Pigolotti, L., Rasmussen, F., Schild, P., Schmehl, R., Stavridou, N., Tande, J., Taylor, N., Telsnig, T., Wiser, R.: Future emerging technologies in the wind power sector: A European perspective. Renewable and Sustainable Energy Reviews **113**, 109270 (2019). doi: 10.1016/j.rser.2019.109270

10. De Rose, A., Buna, M., Strazza, C., Olivieri, N., Stevens, T., Peeters, L., Tawil-Jamault, D.: Technology Readiness Level: Guidance Principles for Renewable Energy Technologies. European Commission: Petten, The Netherlands (2017)

11. Bechtle, P., Schelbergen, M., Schmehl, R., Zillmann, U., Watson, S.: Airborne wind energy resource analysis. Renewable Energy **141**, 1103–1116 (2019). doi: 10.1016/j.renene.2019.03.118

12. Schmehl, R., Tulloch, O.: 8th international Airborne Wind Energy Conference (AWEC 2019): Book of Abstracts. In: AWEC 2019: 8th international Airborne Wind Energy Conference, Delft University of Technology, (2019). doi: 10.4233/uuid:57fd203c-e069-11e9-9fcb-441ea15f7c9c

13. Oehler, J., Schmehl, R.: Aerodynamic characterization of a soft kite by in situ flow measurement. Wind Energy Science **4**(1), 1–21 (2019). doi: 10.5194/wes-4-1-2019

14. Dunker, S.: Ram-Air Wing Design Considerations for Airborne Wind Energy. In: Ahrens, U., Diehl, M., Schmehl, R. (eds.) Airborne Wind Energy, Green Energy and Technology, pp. 517–546. Springer, Berlin Heidelberg (2013). doi: 10.1007/978-3-642-39965-7_31

15. Argatov, I., Silvennoinen, R.: Efficiency of traction power conversion based on crosswind motion. In: Ahrens, U., Diehl, M., Schmehl, R. (eds.) Airborne Wind Energy, Green Energy and Technology, pp. 65–79. Springer, Berlin Heidelberg (2013). doi: 10.1007/978-3-642-39965-7_4

16. Martínez, E., Sanz, F., Pellegrini, S., Jiménez, E., Blanco, J.: Life-cycle assessment of a 2-MW rated power wind turbine: CML method. The International Journal of Life Cycle Assessment **14**(1), 52–63 (2009). doi: 10.1007/s11367-008-0033-9

17. Evans, A., Strezov, V., Evans, T. J.: Assessment of Sustainability Indicators for Renewable Energy Technologies. Renewable and Sustainable Energy Reviews **13**(5), 1082–1088 (2009). doi: 10.1016/j.rser.2008.03.008

18. Fraunhofer Institut: Wind monitor - Distance to Shore and Water Depth. http://windmonitor.iee.fraunhofer.de/windmonitor_en/4_Offshore/2_technik/2_Kuestenentfernung_und_Wassertiefe/. Accessed 6 August 2021

19. Salma, V., Friedl, F., Schmehl, R.: Improving reliability and safety of airborne wind energy systems. Wind Energy **23**(2), 340–356 (2020). doi: 10.1002/we.2433

20. Salma, V., Schmehl, R.: Flight Anomaly Detection for Airborne Wind Energy Systems. Journal of Physics: Conference Series **1618**(3), 032021 (2020). doi: 10.1088/1742-6596/1618/3/032021

21. Jalbert, D. C.: Multi-cell wing type aerial device. US Patent 3,285,546, Nov 1966

22. Folkersma, M., Schmehl, R., Viré, A.: Steady-state aeroelasticity of a ram-air wing for airborne wind energy applications. **1618**(3), 032018 (2020). doi: 10.1088/1742-6596/1618/3/032018

23. Wachter, A. de: Deformation and Aerodynamic Performance of a Ram-Air Wing. M.Sc.Thesis, Delft University of Technology, 2008. http://resolver.tudelft.nl/uuid:786e3395-4590-4755-829f-51283a8df3d2

24. Petry, G., Behr, R., Tscharntke, L.: The Parafoil Technology Demonstration (PTD) Project - Lessons learned and future visions. 15th CEAS/AIAA Aerodynamic Decelerator Systems Technology Conference (1997). doi: 10.2514/6.1999-1755

25. Strong, E.: Safe and rapid aerial delivery of cargo: the screamer concept. In: 17th AIAA Aerodynamic Decelerator Systems Technology Conference and Seminar, p. 2154, (2003). doi: 10.2514/6.2003-2154

26. Erhard, M., Strauch, H.: Control of Towing Kites for Seagoing Vessels. IEEE Transactions on Control Systems Technology **21**(5), 1629–1640 (2013). doi: 10.1109/TCST.2012.2221093

27. Paulig, X., Bungart, M., Specht, B.: Conceptual design of textile kites considering overall system performance. In: Schmehl, R. (ed.) Airborne wind energy, pp. 547–562. Springer Singapore, Singapore (2013)

28. Loyd, M.: Crosswind kite power. Journal of Energy **4**(3), 106–111 (1980). doi: 10.2514/3.48021

29. Erhard, M., Strauch, H.: Flight control of tethered kites in autonomous pumping cycles for airborne wind energy. Control Engineering Practice **40**, 13–26 (2015). doi: 10.1016/j.conengprac.2015.03.001

30. Fogell, N. A. T.: Fluid-structure interaction simulation of the inflated shape of ram-air parachutes. Ph.D. Thesis, Imperial College London, 2014. http://hdl.handle.net/10044/1/24855

31. Mittal, S., Saxena, P., Singh, A.: Computation of two-dimensional flows past ram-air parachutes. International Journal for Numerical Methods in Fluids **35**(6), 643–667 (2001). doi: 10.1002/1097-0363(20010330)35:6<643::aid-fld107>3.0.co;2-m

32. Delany, N. K., Sorensen, N. E.: Low-speed drag of cylinders of various shapes, NASA report NACA-TN-3038, 1953. https://ntrs.nasa.gov/citations/19930083675

33. Bergeron, K., Ecklebe, D., McClure, K., Johari, H., Curlett, T., Pitman, B.: Parachute suspension line drag analysis. In: 20th AIAA Aerodynamic Decelerator Systems Technology Conference and Seminar, p. 2982, (2009). doi: 10.2514/6.2009-2982

34. Jung, T.: Wind Tunnel Study of Drag of Various Rope Designs. In: June 2009. doi: 10.2514/6.2009-3608

35. Dunker, S., Meile, W., Brenn, G.: Experiments in line vibration and associated drag for kites. AIAA Paper 2015-2154. In: Proceedings of the 23$^{\mathrm{rd}}$ AIAA Aerodynamic Decelerator Systems Technology Conference, Daytona Beach, FL, USA, Mar 30–Apr 2, 2015. doi: 10.2514/6.2015-2154

36. Dunker, S.: Tether and bridle line drag in airborne wind energy applications. Airborne Wind Energy–Advances in Technology Development and Research, edited by: Schmehl, R., Green Energy and Technology, 29–56 (2018)

37. Siefers, T. M., Farrar, W. L., Jones, C. N., McLaughlin, T. E., Bergeron, K.: Influence of Angle of Attack on Profile Drag and Flow Induced Vibrations of Parachute Suspension Lines. In: 24th AIAA Aerodynamic Decelerator Systems Technology Conference, p. 4058, (2017). doi: 10.2514/6.2017-4058

38. Hoerner, S. F.: Fluid-dynamic drag. Hoerner fluid dynamics (1965)

39. Argatov, I., Rautakorpi, P., Silvennoinen, R.: Estimation of the mechanical energy output of the kite wind generator. Renewable Energy **34**(6), 1525–1532 (2009). doi: 10.1016/j.renene.2008.11.001

40. Uhlemann, J.: Elastic Constants of Architectural Fabrics for Design Purposes. Ph.D. Thesis, Universität Duisburg-Essen, 2016. doi: 10.2370/9783844044492

41. Jarasjarungkiat, A., Wüchner, R., Bletzinger, K.-U.: Efficient sub-grid scale modeling of membrane wrinkling by a projection method. Computer Methods in Applied Mechanics and Engineering **198**(9-12), 1097–1116 (2009). doi: 10.1016/j.cma.2008.11.014

42. Wagner, H.: Flat sheet metal girders with very thin metal web. Z. Flugtechn. Motorluftschiffahrt **20**, 200–314 (1929)

43. Schek, H.-J.: The force density method for form finding and computation of general networks. Computer Methods in Applied Mechanics and Engineering **3**(1), 115–134 (1974). doi: 10.1016/0045-7825(74)90045-0

44. Barnes, M. R.: Form-finding and analysis of prestressed nets and membranes. Computers & Structures **30**(3), 685–695 (1988). doi: 10.1016/0045-7949(88)90304-5

45. Barnes, M. R.: Form finding and analysis of tension structures by dynamic relaxation. International journal of space structures **14**(2), 89–104 (1999). doi: 10.1260/0266351991494722

46. Gosling, P., Bridgens, B., Albrecht, A., Alpermann, H., Angeleri, A., Barnes, M., Bartle, N., Canobbio, R., Dieringer, F., Gellin, S., Lewis, W., Mageau, N., Mahadevan, R., Marion, J.-M., Marsden, P., Milligan, E., Phang, Y., Sahlin, K., Stimpfle, B., Suire, O., Uhlemann, J.: Analysis and design of membrane structures: Results of a round robin exercise. Engineering Structures **48**, 313–328 (2013). doi: 10.1016/j.engstruct.2012.10.008

47. Roddeman, D. G., Drukker, J., Oomens, C. W. J., Janssen, J. D.: The Wrinkling of Thin Membranes: Part I—Theory. Journal of Applied Mechanics **54**(4), 884–887 (1987). doi: 10.1115/1.3173133

48. Roddeman, D. G., Drukker, J., Oomens, C. W. J., Janssen, J. D.: The Wrinkling of Thin Membranes: Part II—Numerical Analysis. Journal of Applied Mechanics **54**(4), 888–892 (1987). doi: 10.1115/1.3173134

49. Rossi, R., Lazzari, M., Vitaliani, R., Oñate, E.: Simulation of light-weight membrane structures by wrinkling model. International Journal for Numerical Methods in Engineering **62**(15), 2127–2153 (2005). doi: 10.1002/nme.1266

50. Jarasjarungkiat, A., Wüchner, R., Bletzinger, K.-U.: A wrinkling model based on material modification for isotropic and orthotropic membranes. Computer Methods in Applied Mechanics and Engineering **197**(6-8), 773–788 (2008). doi: 10.1016/j.cma.2007.09.005

51. Raible, T., Tegeler, K., Löhnert, S., Wriggers, P.: Development of a wrinkling algorithm for orthotropic membrane materials. Computer methods in applied mechanics and engineering **194**(21-24), 2550–2568 (2005). doi: 10.1016/j.cma.2004.07.045

52. Pipkin, A. C.: Relaxed energy densities for large deformations of membranes. IMA Journal of Applied Mathematics **52**(3), 297–308 (1994). doi: 10.1093/imamat/52.3.297

53. Steigmann, D. J., Pipkin, A. C.: Wrinkling of Pressurized Membranes. Journal of Applied Mechanics **56**(3), 624–628 (1989). doi: 10.1115/1.3176137

54. Rooij, R. de, Abdalla, M.: A finite element interior-point implementation of tension field theory. Computers & Structures **151**, 30–41 (2015). doi: 10.1016/j.compstruc.2015.01.007

55. Chatzikonstantinou, T.: Recent advances in the numerical analysis of ram air wings - The three dimensional simulation code PARA3D. In: Proceedings of the Aerospace Design Conference, Irvine,CA, USA, Feb 16–19, 1993. doi: 10.2514/6.1993-1203

56. Patel, V., Patel, V.: Utilizing a general purpose finite element code for aeroelastic analysis of a ram-air inflated fabric wing. In: 14th Aerodynamic Decelerator Systems Technology Conference, June 1997. doi: 10.2514/6.1997-1507

57. Altmann, H.: Numerical Simulation of Parafoil Aerodynamics and Dynamic Behavior. In: 20th AIAA Aerodynamic Decelerator Systems Technology Conference and Seminar, May 2009. doi: 10.2514/6.2009-2947

58. Ortega, E., Flores, R., Pons-Prats, J.: Ram-air parachute simulation with panel methods and staggered coupling. Journal of Aircraft **54**(2), 807–814 (2017). doi: 10.2514/1.C033677

59. Ortega, E., Flores, R., Cuartero, E., Oñate, E.: Efficient aeroelastic analysis of inflatable structures using enhanced potential flow aerodynamics. Journal of Fluids and Structures **90**, 230–245 (2019). doi: 10.1016/j.jfluidstructs.2019.06.013

60. Castro Fernández, I., Borobia-Moreno, R., Cavallaro, R., Sanchez-Arriaga, G.: Three-Dimensional Unsteady Aerodynamic Analysis of a Rigid-Framed Delta Kite Applied to Airborne Wind Energy. Energies **14**, 8080 (2021). doi: 10.3390/en14238080

61. Borobia-Moreno, R., Ramiro-Rebollo, D., Schmehl, R., Sánchez-Arriaga, G.: Identification of kite aerodynamic characteristics using the estimation before modeling technique. Wind Energy **24**(6), 596–608 (2021). doi: 10.1002/we.2591

62. Mittal, S., Saxena, P., Singh, A.: Computation of two-dimensional flows past ram-air parachutes. International Journal for Numerical Methods in Fluids **35**(6), 643–667 (2001). doi: 10.1002/1097-0363(20010330)35:6<643::aid-fld107>3.0.co;2-m

63. Balaji, R., Mittal, S., Rai, A. K.: Effect of leading edge cut on the aerodynamics of ram-air parachutes. International Journal for Numerical Methods in Fluids **47**(1), 1–17 (2004). doi: 10.1002/fld.779

64. Mohammadi, M. A., Johari, H.: Computation of Flow over a High-Performance Parafoil Canopy. Journal of Aircraft **47**(4), 1338–1345 (2010). doi: 10.2514/1.47363

65. Bosch, A., Schmehl, R., Tiso, P., Rixen, D.: Dynamic Nonlinear Aeroelastic Model of a Kite for Power Generation. Journal of Guidance, Control, and Dynamics **37**(5), 1426–1436 (2014). doi: 10.2514/1.g000545

66. Breukels, J.: An engineering methodology for kite design. Ph.D. Thesis, Delft University of Technology, 2011. http://resolver.tudelft.nl/uuid:cdece38a-1f13-47cc-b277-ed64fdda7cdf

67. Fogell, N. A., Sherwin, S., Cotter, C. J., Iannucci, L., Palacios, R., Pope, D. J.: Fluid-Structure Interaction Simulation of the Inflated Shape of Ram-Air Parachutes. In: AIAA Aerodynamic Decelerator Systems (ADS) Conference, Mar 2013. doi: 10.2514/6.2013-1326

68. Fogell, N. A., Iannucci, L., Bergeron, K.: Fluid-structure interaction simulation study of a semi-rigid ram-air parachute model. In: 24th AIAA Aerodynamic Decelerator Systems Technology Conference, p. 3547, (2017). doi: 10.2514/6.2017-3547

69. Perin, B., Belloc, H., Bordenave, P., Larrieu, C., Simond, C.: Fluid-Structure Interaction Simulation of Ram Air Parachutes - An Application for a Kite -. In: 23rd AIAA Aerodynamic Decelerator Systems Technology Conference, Mar 2015. doi: 10.2514/6.2015-2185

70. Lolies, T., Gourdain, N., Charlotte, M., Belloc, H., Goldsmith, B.: Numerical Methods for Efficient Fluid–Structure Interaction Simulations of Paragliders. Aerotecnica Missili & Spazio **98**(3), 221–229 (2019). doi: 10.1007/s42496-019-00017-2

71. Stein, K., Benney, R., Kalro, V., Tezduyar, T. E., Leonard, J., Accorsi, M.: Parachute fluid–structure interactions: 3-D computation. Computer Methods in Applied Mechanics and Engineering **190**(3-4), 373–386 (2000). doi: 10.1016/s0045-7825(00)00208-5

72. Stein, K. R., Benney, R. J., Tezduyar, T. E., Leonard, J. W., Accorsi, M. L.: Fluid-Structure Interactions of a Round Parachute: Modeling and Simulation Techniques. Journal of Aircraft **38**(5), 800–808 (2001). doi: 10.2514/2.2864

73. Stein, K., Tezduyar, T., Benney, R., Accorsi, M., Johari, H.: Computational Modeling of Parachute Fluid-Structure Interactions. Computational Fluid Dynamics Journal **12**, 516–526 (2003)

74. Stein, K., Tezduyar, T., Benney, R.: Mesh Moving Techniques for Fluid-Structure Interactions With Large Displacements. Journal of Applied Mechanics **70**(1), 58 (2003). doi: 10.1115/1.1530635

75. Stein, K., Tezduyar, T. E., Benney, R.: Automatic mesh update with the solid-extension mesh moving technique. Computer Methods in Applied Mechanics and Engineering **193**(21-22), 2019–2032 (2004). doi: 10.1016/j.cma.2003.12.046

76. Fan, Y., Xia, J.: Simulation of 3D parachute fluid–structure interaction based on nonlinear finite element method and preconditioning finite volume method. Chinese Journal of Aeronautics **27**(6), 1373–1383 (2014). doi: 10.1016/j.cja.2014.10.003

77. Fukasawa, T., Katori, M.: Numerical approach to aeroelastic responses of three-dimensional flexible sails. In: Proceedings of 11th Chesapeake Sailing Yacht Symposium, pp. 87–105, (1993). doi: 10.5957/CSYS-1993-012

78. Renzsch, H., Müller, O., Graf, K.: FLEXSAIL–a fluid structure interaction program for the investigation of spinnakers. In: Proc. International Conference on Innovations in High Performance Sailing Yachts, Lorient, France, (2008)

79. H. F. Renzsch, K. U. G.: Fluid Structure Interaction Simulation of Spinnakers Getting Closer to Reality. International Journal of Small Craft Technology **Vol 153**(Part B2) (2011). doi: 10.3940/rina.ijsct.2011.b2.115

80. Trimarchi, D.: Analysis of downwind sail structures using non-linear shell finite elements. Ph.D. Thesis, University of Southhampton, PhD Thesis, 2012. https://eprints.soton.ac.uk/348893/

81. Marklund, P.-O., Nilsson, L.: Simulation of airbag inflation processes using a coupled fluid structure approach. Computational Mechanics **29**(4-5), 289–297 (2002). doi: 10.1007/s00466-002-0341-z

82. Petit, P., Trosseille, X., Baudrit, P., Gopal, M.: Finite element simulation study of a frontal driver airbag deployment for out-of-position situations, SAE Technical Paper, 2003

83. Garcia, J. R.: Numerical study of dynamic relaxation methods and contribution to the modelling of inflatable lifejackets. Ph.D. Thesis, 2011. https://tel.archives-ouvertes.fr/tel-00659669

84. Burk, S. M., Ware, G. M.: Static Aerodynamic Characteristics of Three Ram-air-inflated Low-aspect-ratio Fabric Wings, Langley Research Center, 1967

85. Nicolaides, J. D.: Parafoil wind tunnel tests, DTIC Document, 1971. https://apps.dtic.mil/sti/citations/AD0731564

86. Ware, G. M., Hassell, J. L.: Wind-tunnel Investigation of Ram-air-inflated All-flexible Wings of Aspect Ratios 1.0 to 3.0, National Aeronautics and Space Administration, 1986

87. Geiger, R., Wailes, W.: Advanced recovery systems wind tunnel test report, Pioneer Aerospace Corporation, 1990

88. Askins, P., Zell, P., Ross, J., Askins, P., Zell, P., Ross, J.: Aerodynamic decelerator testing in the National Full-Scale Aerodynamics Complex. In: 14th Aerodynamic Decelerator Systems Technology Conference, June 1997. doi: 10.2514/6.1997-1528

89. Hummel, J.: Automatisierte Vermessung und Charakterisierung der dynamischen Eigenschaften seilgebundener, vollflexibler Tragflächen. Ph.D. Thesis, TU Berlin, 2017. doi: 10.14279/depositonce-5863

90. Oehler, J., Reijen Marc, van, Schmehl, R.: Experimental investigation of soft kite performance during turning maneuvers. Journal of Physics: Conference Series **1037**, 052004 (2018). doi: 10.1088/1742-6596/1037/5/052004

91. Schmidt, E., Oliveira, M. D. L. C. de, Silva, R. S. da, Fagiano, L., Neto, A. T.: In-flight estimation of the aerodynamics of tethered wings for airborne wind energy. IEEE Transactions on Control Systems Technology **28**(4), 1309–1322 (2019). doi: 10.1109/REDEC.2018.8598022

92. Borobia, R., Sanchez-Arriaga, G., Serino, A., Schmehl, R.: Flight-Path Reconstruction and Flight Test of Four-Line Power Kites. Journal of Guidance, Control, and Dynamics **41**(12), 2604–2614 (2018). doi: 10.2514/1.G003581

93. Wriggers, P.: Nonlinear finite element methods. Springer Verlag, Berlin Heidelberg (2008). doi: 10.1007/978-3-540-71001-1

94. Chapelle, D., Bathe, K.-J.: The finite element analysis of shells-fundamentals. Springer Science & Business Media (2010)

95. Day, A.: An introduction to dynamic relaxation. The Engineer **219**, 218–221 (1965)

96. Cook, R. D. e. a.: Concepts and applications of finite element analysis. John Wiley & Sons (2007)

97. Thedens, P.: mem4py repository. https://github.com/pthedens/mem4py.

98. Contri, P., Schrefler, B.: A geometrically nonlinear finite element analysis of wrinkled membrane surfaces by a no-compression material model. Communications in applied numerical methods **4**(1), 5–15 (1988)

99. Kang, S., Im, S.: Finite element analysis of dynamic response of wrinkling membranes. Computer Methods in Applied Mechanics and Engineering **173**(1-2), 227–240 (1999). doi: 10.1016/S0045-7825(98)00271-0

100. Ziegler, R., Wagner, W., Bletzinger, K.-U.: A finite element model for the analysis of wrinkled membrane structures. International Journal of Space Structures **18**(1), 1–14 (2003). doi: 10.1260/026635103769016591

101. Katz, J., Plotkin, A.: Low speed aerodynamics. 2nd ed. Cambridge University Press (2012). doi: 10.1017/CBO9780511810329

102. Filković, D.: Apame – Aircraft 3D Panel Method. https://www.3dpanelmethod.com. Accessed October 5 2020

103. Fasel, U., Keidel, D., Molinari, G., Ermanni, P.: Aerostructural optimization of a morphing wing for airborne wind energy applications. Smart Materials and Structures **26**(9), 095043 (2017)

104. Fasel, U., Tiso, P., Keidel, D., Molinari, G., Ermanni, P.: Reduced-order dynamic model of a morphing airborne wind energy aircraft. AIAA journal **57**(8), 3586–3598 (2019). doi: 10.1088/1361-665X/aa7c87

105. Gagnon, H., Zingg, D. W.: Aerodynamic optimization trade study of a box-wing aircraft configuration. Journal of Aircraft **53**(4), 971–981 (2016). doi: 10.2514/1.C033592

106. Bungartz, H.-J., Lindner, F., Gatzhammer, B., Mehl, M., Scheufele, K., Shukaev, A., Uekermann, B.: preCICE–a fully parallel library for multi-physics surface coupling. Computers & Fluids **141**, 250–258 (2016). doi: 10.1016/j.compfluid.2016.04.003

107. Degroote, J., Haelterman, R., Annerel, S., Swillens, A., Segers, P., Vierendeels, J.: An interface quasi-Newton algorithm for partitioned simulation of fluid-structure interaction. In: International Workshop on Fluid-Structure Interaction. Theory, Numerics and Applications, p. 55, Kassel University Press GmbH, (2009)

108. Wright, J. R., Cooper, J. E.: Introduction to aircraft aeroelasticity and loads, vol. 20. John Wiley & Sons (2008)

109. Leuthold, R.: Multiple-Wake Vortex Lattice Method for Membrane-Wing Kites. M.Sc.Thesis, Delft University of Technology, 2015. doi: 10.13140/RG.2.2.30811.41765

110. Folkersma, M., Schmehl, R., Viré, A.: Steady-state aeroelasticity of a ram-air wing for airborne wind energy applications. In: Journal of Physics: Conference Series, vol. 1618, 3, p. 032018, IOP Publishing, (2020). doi: 10.1088/1742-6596/1618/3/032018

111. Air Turquoise, S.: Nucleon 25 – Force Measurement on Each Riser. Test Report. http://www.para-test.com/images/Test_Report/PPG_measure/2009/2009-09-29_nucleon25_ppg.pdf, Villeneuve, Switzerland, Sept 29, 2009. Accessed Apr 24, 2021

112. Erhard, M., Strauch, H.: Automatic Control of Pumping Cycles for the SkySails Prototype in Airborne Wind Energy. In: Schmehl, R. (ed.) Airborne Wind Energy: Advances in Technology Development and Research, pp. 189–213. Springer Singapore, Singapore (2018). doi: 10.1007/978-981-10-1947-0_9

113. Thedens, P., Oliveira, G. de, Schmehl, R.: Ram-air kite airfoil and reinforcements optimization for airborne wind energy applications. Wind Energy **22**(5), 653–665 (2019). doi: 10.1002/we.2313

114. Taylor, R., Oñate, E., Ubach, P.-A.: Finite element analysis of membrane structures. In: Oñate, E., Kröplin, B. (eds.) Textile Composites and Inflatable Structures, Computational Methods in Applied Sciences, pp. 47–68. Springer Netherlands, Dordrecht (2005). doi: 10.1007/1-4020-3317-6_4

115. Carpenter, P., Morris, P.: The effect of anisotropic wall compliance on boundary-layer stability and transition. Journal of Fluid Mechanics **218**, 171–223 (1990). doi: 10.1017/S0022112090000970

116. Vinuesa, R., Hosseini, S., Hanifi, A., Henningson, D., Schlatter, S.: Pressure-gradient turbulent boundary layers developing around a wing section. Flow, Turbulence and Combustion **99**(3-4), 613–641 (2017). doi: 10.1007/s10494-017-9840-z

117. Slotnick, J., Khodadoust, A., Alonso, J., Darmofal, D., Gropp, W., Lurie, E., Mavriplis, D.: CFD Vision 2030: A path to revolutionary computational aerosciences. NASA/CR-2014-218178. http://hdl.handle.net/2060/20140003093, Langley Research Center, Hampton, VA, USA, 2014

118. Sørensen, N., Mendez, B., Munoz, A., Sieros, G., Jost, E., Lutz, T., Papadakis, G., Voutsinas, S., Barakos, G., Colonia, S., et al.: CFD code comparison for 2d airfoil flows. Journal of Physics: Conference Series **753**, 082019 (2016). doi: 10.1088/1742-6596/753/8/082019

119. Yilmaz, Ö. et al.: Summary of the blind test campaign to predict the high Reynolds number performance of DU00-W-210 airfoil. AIAA 2017-0915. In: Proceedings of the 35th AIAA/ASME Wind Energy Symposium, Grapevine, TX, USA (2017). doi: 10.2514/6.2017-0915

120. Timmer, W., Bak, C.: Aerodynamics characteristics of wind turbine blade airfoils. In: Brøndsted, P., Nissen, R. (eds.) Advances in Wind Turbine Blade Design and Materials, Woodhead Publishing Series in Energy, pp. 109–149. Woodhead Publishing (2013). doi: 10.1533/9780857097286.1.109

121. Veldman, A.: Boundary layers in fluids. Lecture Notes in Applied Mathematics. http://www.math.rug.nl/~veldman/Colleges/grenslaag/Oud/BoundaryLayers2008.pdf, University of Groningen, 2008

122. Drela, M.: XFOIL: an analysis and design system for low Reynolds Nnumber airfoils. In: Mueller, T. (ed.) Low Reynolds Number Aerodynamics, vol. 54, Lecture Notes in Engineering, pp. 1–12. Springer, Berlin-Heidelberg (1989). doi: 10.1007/978-3-642-84010-4_1

123. Lighthill, M.: On displacement thickness. Journal of Fluid Mechanics **4**(4), 383–392 (1958). doi: 10.1017/S0022112058000525

124. Van Rooij, R.: Modification of the boundary layer calculation in RFOIL for improved airfoil stall prediction. Report IW-96087R, Delft University of Technology, the Netherlands, 1996

125. Oliveira, G. de, Pereira, R., Timmer, W., Rooij, R. van: Improved airfoil polar predictions with data-driven boundary-layer closure relations. Journal of Physics: Conference Series **1037**, 022009 (2018). doi: 10.1088/1742-6596/1037/2/022009

126. Oliveira, G. de, Pereira, R., Ragni, D., Kotsonis, M.: Modeling DBD plasma actuators in integral boundary layer formulation for application in panel methods. In: Proceedings of the 46th AIAA Plasmadynamics and Lasers Conference, Dallas, TX (2015). doi: 10.2514/6.2015-3367

127. Bettermann, D.: Contribution a l'etude de la convection forcee turbulente le long de plaques rugueuses. International Journal of Heat and Mass Transfer **9**(3), 153–164 (1966). doi: 10.1016/0017-9310(66)90014-7

128. Tani, I.: Some equilibrium turbulent boundary layers. Fluid Dynamics Research **1**(1), 49–58 (1986). doi: 10.1016/0169-5983(86)90006-7

129. Buhl, T., Pedersen, C., Sigmund, O.: Stiffness design of geometrically nonlinear structures using topology optimization. Structural and Multidisciplinary Optimization **19**(2), 93–104 (2000). doi: 10.1007/s001580050089

130. Koiter, W.: On the principle of stationary complementary energy in the nonlinear theory of elasticity. SIAM Journal on Applied Mathematics **25**(3). https://www.jstor.org/stable/2100113, 424–434 (1973)

131. Kulfan, B.: The CST universal parametric geometry representation method, recent extensions and applications. Proceedings of the Royal Aeronautical Society Conference **114**(1135), 157–176 (2007). doi: 10.1017/S0001924000003614

132. Ciampa, P, Zill, T., Nagel, B., et al.: CST parametrization for unconventional aircraft design optimization. In: Proceedings of the 27th Congress of the International Council of the Aeronautical Sciences (ICAS), Nice, France (2010)

133. Straathof, M.: Shape parameterization in aircraft design: a novel method, based on B-splines. http://resolver.tudelft.nl/uuid:b4aee571-0489-42ff-ab55-d74e980f724a. Ph.D. Thesis, Delft University of Technology, 2012

134. Sripawadkul, V., Padulo, M., Guenov, M.: A comparison of airfoil shape parameterization techniques for early design optimization. In: Proceedings of the 13th AIAA/ISSMO multidisciplinary analysis optimization conference, Fort Worth, TX (2010). doi: 10.2514/6.2010-9050

135. Deb, K., Pratap, A., Agarwal, S., Meyarivan, T.: A fast and elitist multiobjective genetic algorithm: NSGA-II. IEEE transactions on evolutionary computation **6**(2), 182–197 (2002). doi: 10.1109/4235.996017

136. Grinfeld, P.: Introduction to tensor analysis and the calculus of moving surfaces. Springer (2013)

137. Uhlemann, J., Stranghöner, N., Saxe, K.: Stiffness parameters for architectural fabrics: an analysis of two determination procedures. Structural Engineering International **25**(1), 9–19 (2015). doi: 10.2749/101686614X14043795570291

CURRICULUM VITÆ

Paul THEDENS

Paul Thedens was born on February 15th in Henstedt-Ulzburg, Germany. He attended the Walddörfer Gynmasium in Hamburg to obtain his Abitur in 2008. After a year of travel and work in New Zealand he attended the Bachelor studies of aerospace engineering at Delft University of Technology, where he graduated in 2013. Before his graduation, he started an internship at Germanischer Lloyd SE in Hamburg in the wind turbine blade certification department for six months.

Following the Bachelor graduation, he started the dual programme European Wind Energy Master (EWEM) at DTU in Denmark and Delft University of Technology, and followed the track of wind turbine rotor design. During his master studies he focused on the development and implementation of numerical methods, such as finite element and finite volume methods. He graduated in 2015 with a thesis about topology optimisation of membrane structures with application to a parafoil rib.

In late 2015 he started his PhD within the interdisciplinary doctoral training network Airborne Wind Energy System Modelling, Control and Optimisation (AWESCO), which addressed key technical challenges of wind energy generation using tethered wings, of both fixed wing and flexible membrane type. The programme took place at University of Freiburg at the Department of Microsystems Engineering (IMTEK), and SkySails in Hamburg where he is employed since 2019.

LIST OF PUBLICATIONS

6. **P. Thedens, R. Schmehl**, *Aero-Structural Model for Ram-Air Kite Simulations.* Energies 2022 (under review)

5. **P. Thedens, M. A. M. Folkersma, A. Viré, R. Schmehl**, *Computational simulation of the aerodynamics of a ram-air kite for airborne wind energy applications.* Conference: Wind Energy Science Conference (WESC) 2021, Hannover, Germany, 2021.

4. **P. Thedens, G. de Oliveira, R. Schmehl**, *Ram-air kite airfoil and reinforcements optimization for airborne wind energy applications*, Wind Energy **22**, 5 , pp. 653–665 (2019).

3. **P. Thedens, M. Bungart, R. Schmehl**, *Steady-State Solver for a Ram-Air Kite Aero-elastic Model Based on Dynamic Relaxation.* Airborne Wind Energy Conference 2019, Glasgow, Scotland, 2019.

2. **M. A. M. Folkersma, P. Thedens, R. Schmehl**, *Fluid-structure interaction of inflatable wing section*, 13th OpenFOAM Workshop (OFW13), Shanghai, China, 24-29 June 2018.

1. **P. Thedens, R. Schmehl**, *Ram-Air Kite Reinforcement Optimisation for Airborne Wind Energy Applications.* Airborne Wind Energy Conference 2017, Freiburg, Germany, 2017.